

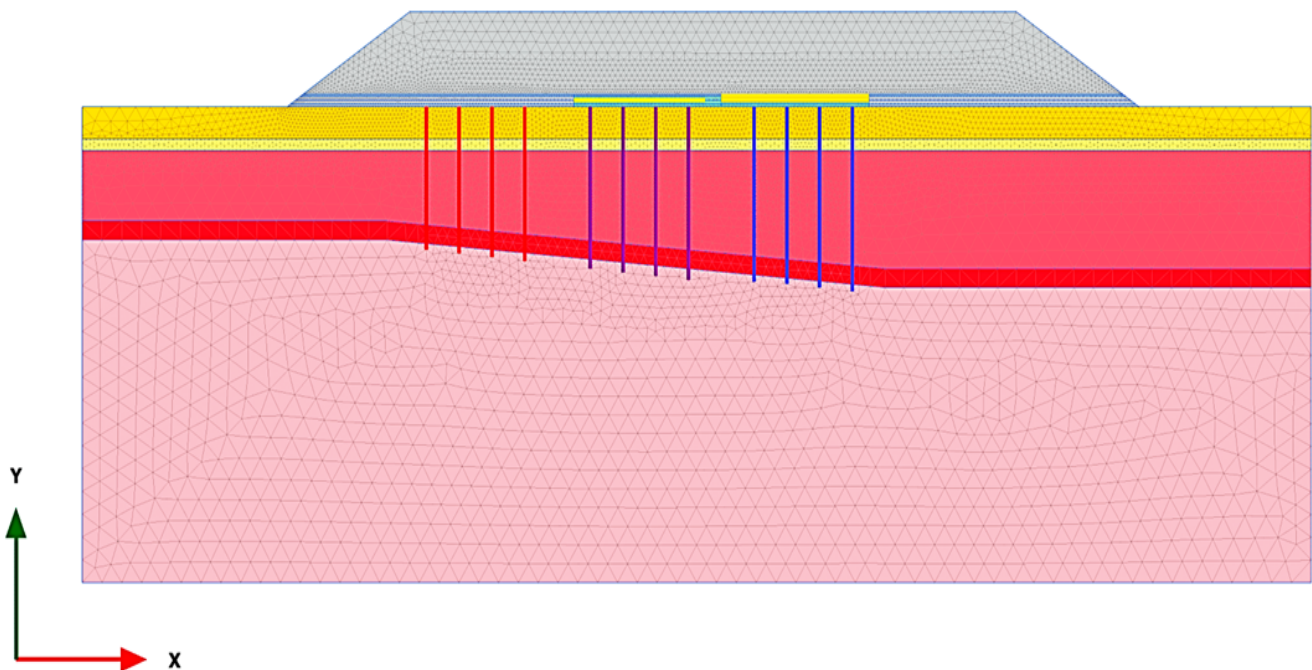


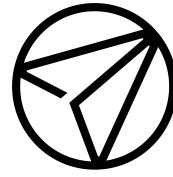
DEGREE PROJECT IN ,
SECOND CYCLE, 30 CREDITS
STOCKHOLM, SWEDEN 2020

2D Modelling of Geosynthetically Reinforced Piled Embankments

Calibration Methods in PLAXIS 2D & Review of
Analytical Guidelines

MAYA SLEIMAN





AFRY
ÅF PÖYRY

2D Modelling of Geosynthetically Reinforced Piled Embankments

Calibration Methods in PLAXIS 2D & Review of Analytical Guidelines

Maya Sleiman

KTH Supervisor:
Stefan Larsson

AFRY Supervisor:
Magnus Ruin

Abstract

This thesis focuses on the 2D modelling of Geosynthetically Reinforced Piled Embankments (GRPE) in PLAXIS 2D. In doing so, it explores two main aspects: 1) the calibration of Interface Stiffness Factors (ISFs) governing the soil-pile interaction of Embedded Beam Row (EBR) elements in PLAXIS 2D, and 2) the prospects and limitations of modelling geogrids (GR) in PLAXIS 2D when underlain by EBR elements; although several studies have validated the EBR element in modelling piles, none address the geogrid-EBR interaction and its implications on modelling GRPE systems. The thesis performs the calibration and validation processes using the full-scale GRPE structure ASIRI (*Amélioration des Sols par Inclusions Rigide*) as documented in Briançon and Simon, 2012 and Nunez et al., 2013. Calibration of the EBR's ISFs is done against 1) load-displacement curve of a test pile, 2) load-displacement of the structure's monitored piles, and 3) differential soil-pile settlement. Model results for soil settlement, pile settlement, and pile load are then compared to reported values from the ASIRI site.

Results show that the natural deviation between the structure and test pile's load - displacement results in a wide range of possible calibration values for the ISFs, making calibration based on a test pile's load-displacement curve an unpractical method. Even when such natural deviations were eliminated by calibrating the model against the structure's reported values for pile load-displacement, model predictions for subsoil displacement were compromised. It is thus advisable to calibrate the EBR element with respect to soil settlement, pile settlement, and pile load rather than solely on a load-displacement curve as to avoid high divergences in soil-pile differential settlement.

Modelling geogrids in GRPE systems, PLAXIS 2D underestimates GR strain due to its inability to simulate GR deflection: EBR elements are superimposed on top of a continuous soil mesh, thus allowing the embankment soil to settle through the EBR element. This unrealistically minimizes GR deflection, which underestimates GR strain when modelling GRPEs in PLAXIS 2D.

In addition to validating the 2D modelling of GRPE systems, the thesis conducts a comparative literature review of GRPE design guidelines, focusing on the British BS8006 (2010), the German EBGE0 (2011), and the Dutch CUR226 (2016). It then applies the latter two to the ASIRI full scale case study and compares results for predicted maximum GR strain and displacement to those from the PLAXIS 2D model and ASIRI measurements.

The literature review shows that the geogrid load distribution is highly dependent on the state of subsoil support, where a uniform distribution is more appropriate for high subsoil support, and an inverse-triangular one more appropriate for low subsoil support. However, the analytical analysis of the ASIRI case shows that the triangular distribution, previously dismissed as unrealistic by the literature review, gives satisfactory results due to a combination of soil sliding and high subsoil support at the ASIRI site.

Sammanfattning

Examensarbetet utvärderar 2D modellering av bankpålning med geosyntetisk armering (Geosynthetically Reinforced Piled Embankments – GRPE) i PLAXIS 2D. Examensarbetet utforskar två huvudaspekter: 1) kalibrering av Interface Stiffness Factors (ISFs) som styr jord-påle samspelet av Embedded Beam Row (EBR) element i PLAXIS 2D, och 2) möjligheter och begränsningar vid modellering av geonät i PLAXIS 2D när de ligger över EBR element. Även om flera studier har validerat användningen av EBR element för modelleringen av pålning, har inga behandlat samspelet geonät-EBR samt dess implikationer på modelleringen av GRPE.

I arbetet har kalibrerings- och valideringsprocesser genomförts genom att använda den fullskaliga GRPE strukturen ASIRI (*Amélioration des Sols par Inclusions Rigide*) som dokumenterats i Briançon och Simon(2012) samt Nunez et al.(2013). Kalibrering av EBR ISFs har utförts mot: 1) last/förskjutningssamband av testpålar, 2) last/förskjutningssamband av övervakade pålar i strukturen, och 3) jord-påle differenssättningen. Modellens resultat för sättningar i jorden, deformation i pålarna och lasten i pålarna jämförs med mätningar från ASIRI.

Resultaten visar att naturliga avvikelser mellan strukturens- och testpålens last/förskjutningssamband resulterar i ett brett spektrum av möjliga kalibreringsvärden för ISFs, som gör kalibrering mot testpålens last/förskjutningssamband opraktisk. Även vid justering för detta genom kalibrering mot strukturpålens last/förskjutningssamband minskade modellens noggrannhet för sättningar i jorden. Det är således lämpligt att kalibrera EBR element mot sättningar i jorden, deformation i pålarna och lasten i pålarna i stället för bara last/förskjutningssambanden för att undvika hög divergens i differenssättningen jord-påle.

Vid modellering av GRPE-geonät underskattar PLAXIS 2D töjningen i geonäten på grund av sin oförmåga att simulera geonätets utböjning. EBR element ligger över ett kontinuerligt beräkningsnät av jord (soil mesh) som tillåter bankfyllningen att sätta genom EBR element. Detta förhindrar utböjningen i geonätet som resulterar i en underskattning av töjningen i nätet vid modellering av GRPE i PLAXIS 2D. Förutom validering av 2D modelleringen av GRPE strukturer utför examensarbetet en jämförande litteraturstudie av GRPE dimensioneringsriktlinjer med fokus på Brittisk BS8006 (2010), Tysk EBGeo (2011), och Nederländsk CUR226 (2016). De två sista nämnda riktlinjerna tillämpas på ASIRI för att prognosticera maximum geonättöjning och utböjning. Beräkningsresultat jämförs med värden från PLAXIS 2D modellen och mätningar från ASIRI.

Litteraturstudien visar att geonätets belastningsfördelning är beroende främst på stödet från den underliggande jorden. Likformig belastningsfördelningen är lämpligare för en hög stödnivå och en invers-triangulär belastningsfördelningen för en låg stödnivå. Dock visar den analytiska analysen av ASIRI strukturen att en triangulär belastningsfördelning, som ansågs vara orealistisk i litteraturstudien, ger tillfredsställande resultat. Det är på grund av kombinationen av 'jordensglidning' och hög stödnivå från den underliggande jorden i ASIRI:s fall.

Acknowledgments

I would like to thank AFRY for hosting and funding my thesis. To my AFRY advisor Magnus Ruin, your openness, technical expertise, and thoughtful guidance have been crucial to the completion of this thesis.

Special thanks to my KTH advisor Stefan Larsson for his continuous availability and his insightful and thorough feedback.

Mom and Dad, thank you for being so patient and understanding of distance since I was seventeen, and my sisters for being the inspiration they are.

Yousef, thank you for your unwavering support throughout the past six years.

Contents

List of Figures	8
List of Tables	12
1 Introduction	5
1.1 Geosynthetically Reinforced Piled Embankments	5
1.2 Modelling GRPEs: Analytical and Numerical Approaches	5
1.3 Aim and Scope of Study	8
1.4 Thesis Structure and Content	8
2 Literature Review: Constituting Models and Design Guidelines	10
2.1 Arching Models	10
2.1.1 Rigid Arching Models	10
2.1.2 Limit Equilibrium Arching Models	12
2.1.3 Concentric Arches Model	15
2.2 European Codes	17
2.3 Conclusion	32
3 Modelling GRPE Systems in PLAXIS 2D	34
3.1 Model Geometries	34
3.2 Soil Models	35
3.3 Embedded Beam Row Element	39
3.4 Geogrids and Line Contractions	43
3.5 Summary	45
4 Methods: Case Study for PLAXIS 2D Model Validation	47
4.1 General Model Properties	50
4.2 Soil Profile Characterization	50
4.3 Structures	52
4.3.1 Embedded Beam Row as Piles	52
4.3.2 Geosynthetic Reinforcement using Geogrids	54

4.4	Staged Construction	55
4.5	Understanding the Effect of Interface Stiffness Factors	55
4.6	Model Variants: Calibration of Interface Stiffness Factors	56
4.6.1	Calibration to Load-Displacement Curve (LDC)	56
4.6.2	Calibration to Measured Load-Displacement (MLD)	57
4.6.3	Calibration to Measured Differential Settlement (MSD)	59
5	Results and Discussion	61
5.1	Effect of Interface Stiffness Factors	61
5.2	Calibration to Load-Displacement Curve (LDC)	64
5.2.1	Results	64
5.2.2	Discussion	65
5.3	Calibration to Measured Load-Displacement (MLD)	66
5.3.1	Results	67
5.3.2	Discussion: Calibration to LDC vs. MLD	68
5.4	Conclusions and Recommendations for ISF Calibration	68
6	Geogrid Strain: Numerical and Analytical Validation	71
6.1	Plaxis 2D Output	71
6.1.1	Methods	71
6.1.2	Results	72
6.1.3	Discussion	73
6.2	Analytical models: EBGEO and CUR 226	77
6.3	Results	78
6.4	Discussion	80
7	Summary and Future Work	81
7.1	Summary	81
7.2	Future work	82
A	Reported Data from Case Studies	85
A.1	ASIRI	85
B	Excel sheet for German Design Code EBGEO	87
B.1	Subgrade Support	93
C	Excel sheet for Dutch Design Code CUR-226	94

List of Figures

1.1	Common components of a GRPE structure. (van Eekelen & Brugman, 2016)	6
1.2	General flow of designing a GRPE system in BS8006, EBGEO, and CUR 226 guidelines	7
1.3	A comparison done by Edgars (2016) between 2D and 3D modelling of an extensive settlement case	8
2.1	The SINTEF Model. (Eiksund et al., 2000)	11
2.2	Collin’s Enhanced Arching Model. (Collin, 2013)	11
2.3	Collin’s Enhanced Arching Model for square and triangular pile grids (Collin, 2013)	12
2.4	Hewlett and Randolph Model based on two limit states: one at the crown and another at the cap (S van Eekelen 2012)	13
2.5	Zaeske’s model. (Zaeske and Kempfert, 2002)	14
2.6	Soil element under equilibrium according to Zaeske’s model (Zaeske and Kempfert, 2002)	14
2.7	Design chart based on Zaeske’s model at $\phi = 30^\circ$.(Zaeske and Kempfert, 2002)	15
2.8	Concentric Arches Model uses 2D arches and 3D hemispheres (van Eekelen & Brugman, 2016)	16
2.9	GR load resulting from the Concentric Arches model (van Eekelen & Brugman, 2016)	16
2.10	Tk Geo 13 recommendations for georeinforced piled embankments (Trafikverket, 2016)	17
2.11	GR line load is used to calculate the tensile force in a meter run of the GR. (BSI, 2010)	19
2.12	Distance to the GR in single and multi-layered systems according to EBGEO (GSC, 2011)	20
2.13	Design charts based on Zaeske’s equilibrium equations.(GSC, 2011)	21
2.14	Load distributions areas as defined by EBGEO. (van Eekelen, 2015)	22
2.15	EBGEO design chart to calculate GR strain (GSC, 2011)	23

2.16	Load distribution according to the Dutch CUR 226 guideline. (van Eekelen & Brugman, 2016)	24
2.17	Load distributing geometries defined by the Dutch CUR 226 guideline (van Eekelen & Brugman, 2016)	24
2.18	GR square geometry in the Dutch CUR 226 guideline (van Eekelen & Brugman, 2016)	25
2.19	GR strip geometry in the Dutch CUR 226 guideline (van Eekelen & Brugman, 2016)	26
2.20	Uniform and inverse triangular load distributions on the GR in the Dutch CUR 226 guideline	26
2.22	Tensioned membrane element used by all reviewed guidelines to derive strain as a function of GR load (van Eekelen, 2015)	27
2.21	Flow chart summarizing the Dutch Code	28
2.23	Comparisons of guidelines considered in Khansari and Vollmert, 2018 compared to measured values at a GRPE site in Hamburg.	32
3.1	Plane strain (left) vs axisymmetric (right) models (Plaxis2D, 2019a)	35
3.2	Oedometer stiffness at a reference stress p^{ref} (Plaxis2D, 2019b)	36
3.3	The Hyperbolic stress-strain relation in primary loading for a standard drained triaxial test (Plaxis2D, 2019b)	37
3.4	Compression and swelling indices can be found by plotting Void ratio vs log-stress under one dimensional compression (Plaxis2D, 2019b)	38
3.5	Surface settlement is most sensitive to E_{oed} (Satibi, 2014)	38
3.6	Modified compression and swelling indices found by plotting volumetric strain vs. natural log of stress at a reference pressure. (Plaxis2D, 2019b)	39
3.7	EBR element can be seen as superimposed on the 2D mesh (Plaxis2D, 2019a)	40
3.8	Elastic zone at the bottom of an EBR element in PLAXIS 2D (Plaxis2D, 2019a)	42
3.9	ISFs governing the interaction of the EBR element with the soil mesh (Plaxis2D, 2019a)	42
3.10	Interface elements governing the axial, lateral, and base interactions of the pile with the soil mesh (Plaxis2D, 2019a)	43
3.11	screenshot from PLAXIS 2D showing input table for the N- ϵ geogrid strength option	44
3.12	Displacement versus time in a creep test (Plaxis2D, 2019a)	45
4.1	Cross sectional view of the ASIRI test site showing its four test sections (Briançon & Simon, 2012)	47
4.2	Plane view of the ASIRI test site showing its four test sections, edited from (Briançon & Simon, 2012)	48
4.3	Measurement instrumentation on the ASIRI site, edited from (Briançon & Simon, 2012)	49

4.4	Longitudinal section modelled in PLAXIS 2D	51
4.5	Cumulative shear load reported in Nunez et al., 2013 can be approximated by a constant linear skin resistance	52
4.6	Transverse section of test section 2R used to understand the effect of ISFs on soil and pile settlement	56
4.7	Load-displacement curve reported by Nunez et al., 2013 and Briançon and Simon, 2012 following a static load test of an embedded pile at the ASIRI site	57
4.8	ISF_b of monitored piles is adjusted for each pile group to match pile-displacement curve	58
4.9	Load-displacement state of monitored piles in test sections 2R, 3R, and 4R plotted along the load-displacement curve of the test pile	59
5.1	Effect of varying ISF_a on soil and pile settlement	61
5.2	Effect of varying ISF_l on soil and pile settlement	62
5.3	Effect of varying ISF_b on soil and pile settlement	62
5.4	Percent change in differential settlement as a function of ISF value used . .	63
5.5	calibration of ISF_b of pile groups 2R, 3R, and 4R from their default values to match the load-displacement curve (LDC)	64
5.6	Settlement profile under default and calibrated ISF_b , compared to measured values	65
5.7	load-displacement state of monitored piles plotted over the reported load-displacement curve (Briançon & Simon, 2012)	66
5.8	Monitored piles in the ASIRI site pointed out on the PLAXIS 2D model . . .	66
5.9	Settlement profile under default, LDC-calibrated, and MLD-calibrated ISF values, compared to measured settlement	68
5.10	Settlement profile (using default ISF values) under various shaft capacity distributions	70
6.1	Locations of geogrid strain guages in test sections 3R and 4R, as reported in Briançon and Simon, 2012	72
6.2	PLAXIS 2D strain profile under various ISF-calibrated values, compared to measured strain for test section 3R	72
6.3	Higher errors of predicted to measured maximum strain is in models with less GR deflection, and vice versa	73
6.4	PLAXIS 2D strain profile under various ISF-calibrated values, compared to measured strain for the bottom geogrid in test section 4R	74
6.5	PLAXIS 2D strain profile under various ISF-calibrated values, compared to measured strain for the top geogrid in test section 4R	74
6.6	settlement soil mesh profile before (yellow, dashed) and after (purple, full) pile superimposition	75

6.7	EBR element fixed to the soil mesh at its bottom node (left) and top node (right)	76
6.8	EBR element fixed to a plate element at its top node	76
6.9	Anchor element with LTP rigidity separating EBR element and geogrid	77
6.10	The four analytical models used to predict maximum strain in test section 3R	78
6.11	GR deflection predicted by different models	79
6.12	Maximum GR strain predicted by different models	79
6.13	Higher soil settlement reported near the pile compared to midspan between piles, as reported by Briançon and Simon, 2012	80
A.1	Soil parameters reported by Nunez et al., 2013	85
A.2	Soil parameters reported by Briançon and Simon, 2012	85
A.3	LTP parameters reported by Briançon and Simon, 2012	86
A.4	Geogrid and Geotextile parameters as reported by Briançon and Simon, 2012	86

List of Tables

2.1	Comparative Summary of major European design guidelines for the design of GRPEs	29
4.1	Input parameters for the characterization of subsoil layers modelled using the Soft Soil PLAXIS model	52
4.2	Input parameters for the characterization of Embankment (E), Load transfer platform (LTP), and compact gravel substratum (CG)	53
4.3	Input parameters for the EBR element representing the piles	54
4.4	Input parameters to the geogrid element representing the geotextile in 3R and geogrids in 4R	55
4.5	Measured soil and pile settlement in sections 2R, 3R, and 4R as reported by Nunez et al., 2013 and Briançon and Simon, 2012	59
5.1	ISF values at their default and LDC-calibrated values	64
5.2	Measured load and displacement values at the monitored piles as reported by Briançon and Simon, 2012 and Nunez et al., 2013	67
5.3	ISF values under their default, LDC-, and MDC-calibrated models	67
6.1	Input parameters into the German EBGEO and Dutch CUR226 guidelines . .	77

Nomenclature

Abbreviations

EBR	Embedded Beam Row
FE	Finite Elements
GR	geosynthetic reinforcement
GRPE	geosynthetically reinforced piled embankment
LDC	load-displacement curve (from embankment-adjacent test piles)
LTP	load transfer platform
MDS	measured differential settlement (at monitored piles)
MLD	measured load-displacement (at monitored piles)

BS8006

γ	unit weight of the embankment fill	kN/m^3
ϕ'	Angle of internal friction of soil under effective stress conditions	deg
ε	reinforcement strain	—
a	pile cap side (and GR strip width)	m
E_{cap}	Arching efficacy assuming failure at pile cap	—
E_{crown}	Arching efficacy assuming failure at arch crown	—
f_{fs}	partial factor for soil unit weight load	—
f_q	partial factor for external load	—
H	embankment height	m

K_p	Coefficient of passive earth pressure	–
Q_p	pile design capacity	kN
s	pile center-to-center distance	m
T_{rp}	Tensile force generated in basal reinforcement in piled embankments due to transfer of vertical loading	kN/m
w_s	external load	kPa
$W_{T,min}$	minimum design value for W_T	kN/m
W_T	Distributed vertical load acting on basal reinforcement between adjacent pile caps	kN/m

Carlson and Rogbeck's Model

a	pile cap width	m
c	pile center-to-center distance	m
F_{2D}	Weight of the 30° 2D soil wedge in Carlson's 2D model	kN
F_{3D}	Weight of the 30° 3D soil cone in Rogbeck's 3D extension of Carlson's 2D model	kN

CUR-226

γ	embankment soil unit weight	m^2
A_i	pile influence area = $s_x s_y$	m^2
A_p	pile cap area	m^2
$A_{Lx/y}$	area belonging to a GR strip in the x or y direction	m^2
b_{eq}	equivalent width of a circular pile	m
d	pile diameter	m
$H_{g,2D}$	Height of the largest of the 2D arches	m
$H_{g,3D}$	Height of the largest of the 3D Hemispheres	m
$J_{x/y}$	tensile stiffness of the GR in the x or y direction	kN/m
k	modified subgrade reaction, accounts for full influence area	kN/m^3
k_s	subgrade reaction	kN/m^3

L_{2D}	Length of the GR strip, oriented along the x or y axis, on which the 2D arches exert a force	m
L_{3D}	width of GR square	m
$L_{wx/y}$	clear distance between two adjacent piles	m
q_{av}	average load on GR strip	kN/m^2
s_d	diagonal distance between opposite piles	m
s_x, s_y	pile center-to-center distance along the x or y direction	m
E	arching efficacy, portion of load transferred directly to piles	–
H	embankment height	m
T	Tensile force in the GR due to vertical load	m^2

EBGEO

$\sigma_{zo,k}$	normal stress between the piles	kPa
$\sigma_{zs,k}$	normal stress on the piles	kPa
ϕ'_k	drained friction angle	deg
A_E	pile influence area = $s_x \cdot s_y$	m^2
A_s	pile cap area	m^2
A_{Lx}	Load coverage area in the x-direction	m^2
A_{Ly}	Load coverage area in the y-direction	m^2
E_L	arching efficacy	m
$E_{s,k}$	constrained stratum modulus	–
F_{xk}	normal load acting on GR strip in the x-direction	m
F_{yk}	normal load acting on GR strip in the y-direction	m
J_k	characteristic value of geogrid tensile stiffness	kN/m
k_s	subgrade reaction modulus	–
L_x	length of GR strip between two adjacent piles in the x-direction	m

L_y	length of GR strip between two adjacent piles in the y-direction	<i>m</i>
p_k	external load	<i>kPa</i>
s_x	pile free distance in the x-direction	<i>m</i>
s_y	pile free distance in the y-direction	<i>m</i>
t_w	stratum thickness	<i>m</i>
z	distance from subsoil surface to geosynthetic reinforcement See Figure 2.12	<i>m</i>

Hewlett and Randolph Model

ϕ	embankment fill friction angle	<i>deg</i>
a	pile cap side	<i>m</i>
H	embankment height	<i>m</i>
s	pile center-to-center distance	<i>m</i>

Collin Model

γ	unit weight of the load transfer platform	<i>kN/m³</i>
A_n	Area of the geogrid under the wedge at level n	<i>m²</i>
A_{n+1}	Area of the geogrid under the wedge at level n+1	<i>m²</i>
d	pile diameter	<i>m</i>
h_n	distance between geogrid at level n and that at level n+1	<i>m</i>
s	pile free distance	<i>m</i>

PLAXIS 2D Modelling

ISF_a	axial interface stiffness factor
ISF_b	axial interface stiffness factor
ISF_c	axial interface stiffness factor
C	clay layer
CM	clayey made-ground layer
E	embankment fill

SC	sandy clay layer	
SS	substratum layer	

SINTEF Model

β	inverse the slope of the soil wedge in the SINTEF model	–
a	pile cap width	m
c	pile center-to-center distance	m
H	embankment height	m

TkGeo-13

a	pile cap width	m
c	pile center-to-center distance	m
H	embankment height	m
t	LTP thickness	m

Zaeske Model

γ	unit weight of the Zaeske soil element	kN/m^3
σ_z	vertical stress	kPa
σ_ϕ	lateral earth pressure	kPa
d	pile diameter	m
dA_u	Infinitesimal area of the bottom side of the Zaeske soil element	m^2
dV	Infinitesimal volume of the the Zaeske soil element	m^3
h	embankment height	m
s	pile center-to-center distance	m

Chapter 1

Introduction

1.1 Geosynthetically Reinforced Piled Embankments

A geosynthetically reinforced piled embankment (GRPE) consists of an embankment platform on a pile foundation (see Figure 1.1). The embankment is reinforced with one or more horizontal layers of geosynthetic reinforcement, conventionally installed at the embankment base.

The lower reinforced section of the embankment, referred to in literature as the *mattress* or *load transfer platform* (LTP), often consists of a frictional material like crushed aggregate with relatively high friction angle and stiffness, with the rest of the embankment often made of lower-quality fill.

GRPEs are often sought after for the construction of roads, railways, and industrial areas over highly compressible soft soils, particularly when alternative options are not feasible. These may include soil replacement, accelerated consolidation with the aid of vertical drains, and the transfer of load to a hard substratum. However, when the soft soil layer is too thick, soil replacement or reaching the hard-substratum become economically and executionally cumbersome, and accelerated consolidation might not be feasible due to time constraints or larger stability risks induced by excessive settlement.

Various full-scale case studies (e.g. Briançon and Simon, 2012; Nunez et al., 2013; and Oh and Shin, 2007) have pointed out to the added benefit of geosynthetically reinforcing piled embankments for reducing differential settlement.

1.2 Modelling GRPEs: Analytical and Numerical Approaches

Several analytical models describing the transfer of load from the embankment to the piles, and later to the geosynthetic reinforcement (GR), have been formulated, the earliest and most fundamental of which was Terzaghi's description of soil arching in 1943.

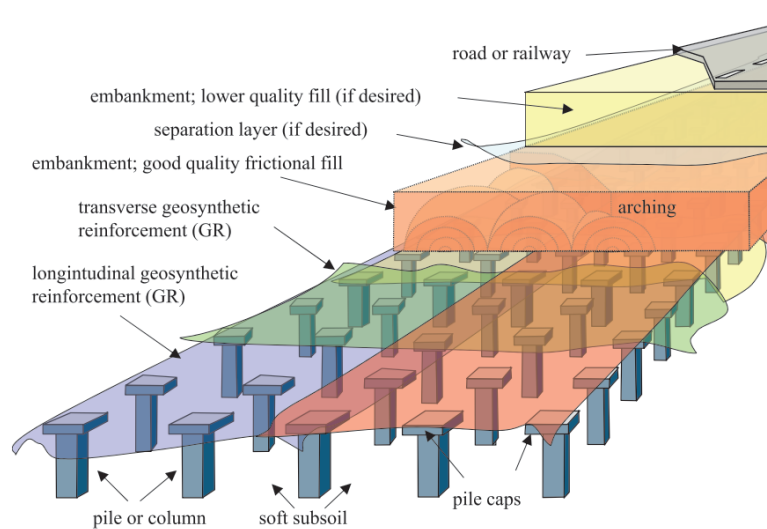


Figure 1.1 – Common components of a GRPE structure. (van Eekelen & Brugman, 2016)

Since then, multiple countries have developed GRPE design guidelines built around one or more of these analytical models. Most prominent of these are the British Design guideline BS8006, the German EBGEO, and the Dutch CUR226 (2016).

These guidelines have a common general flow structure shown in Figure 1.2 below, where the guidelines can be divided into two main steps:

1. *Step 1: Load distribution* - This step uses an arching model to find the arching efficacy of the GRPE system. This divides the total load into an arching load, received by the piles, and a residual load, received by the GR and subsoil.
2. *Step 2: Membrane Interactions* - This step uses the resultant residual load from part one to find the tensile force and resultant strain in the GR. Guidelines often use the same tensioned membrane formulas, but differ in their assumptions for the shape of GR load and the existence of subsoil support.

Shortcomings

The accuracy of these arching models and design guidelines is discussed in Chapter 2, but a common shortcoming among them is their focus on single-layered GRPEs, providing no guidance on the optimal arrangement of multi-layered systems.

The Swedish code, expanded upon in Section 2.2, provides rigid guidelines on the optimal number and spacing of GRs, but the guidelines are not linked to variables like embankment height, pile free distance, or GR properties.

This calls for the use of more robust and case-specific analysis methods, like Finite Elements (FE) modelling using existing software. This is of great use both to further develop existing

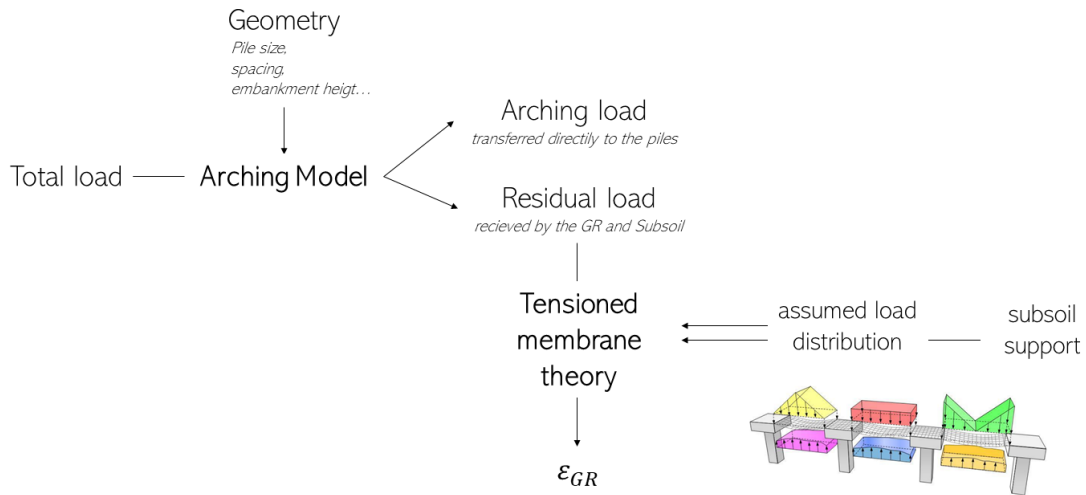


Figure 1.2 – General flow of designing a GRPE system in BS8006, EBGeo, and CUR 226 guidelines

analytical models *and* to represent cases that don't fulfill the limiting requirements of such guidelines.

Given the 3D nature of GRPEs, an FE analysis requires the use of a 3D FE package to accurately represent the system. However, this often comes at a great expense of computational time. In a comparison of 2D and 3D models of a settlement study, Edgers, 2016 concludes that the 3D model takes extensively more time both to set up and execute, with setup time in the order of a day compared to hours for the same system modelled in 2D.

Modelling GRPE systems in 2D underwent an improvement in 2012 when PLAXIS 2D introduced its Embedded Beam Row (EBR) element, which was later reviewed by Sluis (2012) (documented in Brinkgreve et al., 2017) concluding that the EBR element gives better results than modelling piles as plates yet significantly underestimates settlement. Additionally, the model was validated with piled embankment structures that were not geosynthetically reinforced. As will be shown in this thesis, the use of EBR elements along with geogrids - as is the case in GRPE systems - results in unrealistic geogrid-pile interactions which require circumvention if a 2D model is to be used for GRPE modelling.

Table 4. Program Setup, Execution and Verification Time

Software Program	Setup Time	Execution Time	Verification/Mesh Fineness Time
Plaxis 2D	Hours	Minutes	Days
Plaxis 3D	Day	Hours	Weeks

Figure 1.3 – A comparison done by Edgars (2016) between 2D and 3D modelling of an extensive settlement case

1.3 Aim and Scope of Study

The aim of this Master thesis is thus multi-fold:

1. Provide a comparative literature review of the most prominent design codes for (GR)PEs and gives a brief overview of the analytical arching models they are based on. Arching models have undergone tremendous refinement since Terzaghi first introduced his model for soil arching in 1943. It is thus crucial that this thesis acknowledges and builds upon this massive mass of literature. In particular, the thesis focuses on the British BS8006 (2010), the German EBGE0 (2011), and the Dutch CUR226 (2016) guidelines, and compares their performance by reviewing available validation case studies done on them.
2. Provide practical recommendations for the use of PLAXIS 2D for the modelling of GRPE systems. The thesis uses a full-scale case study with 4 test sections to assess the performance of the suggested 2D modelling approach. This is done by:
 - Exploring multiple methods of calibrating the Embedded Beam Row (EBR) elements in PLAXIS 2D used to simulate piles.
 - Validating the ability of PLAXIS 2D to simulate GR behavior in GRPE systems. This has not been explored before.
3. Apply analytical guidelines to the case study and compare results of geogrid strain and displacement to measurements and PLAXIS 2D output.

1.4 Thesis Structure and Content

Following this introduction, the thesis is divided into six main chapters.

Chapter 2 presents the comparative literature review of arching models and design guidelines, including several validation studies.

Chapter 3 presents the PLAXIS 2D soil models and structural elements relevant to the modelling of the GRPE case study.

Chapter 4 presents the full scale case study and the methods of modelling it in PLAXIS 2D, including the various calibration methods used for the EBR elements.

Chapter 5 presents results of the validation process in regards to EBR calibration, and presents recommendations for this calibration process.

Chapter 6 examines PLAXIS 2D's ability to model GR strain and displacement in GRPE systems, and applies the analytical guidelines (German EBGeo and Dutch CUR226) to the case study to compare analytical predictions to PLAXIS 2D outputs and measurements reported.

Chapter 8 summarizes major conclusions from the thesis, and suggests possible areas of future work.

Chapter 2

Literature Review: Constituting Models and Design Guidelines

Piled embankments transfer the load to the piles through the phenomenon of soil arching. Terzaghi (1943) defined arching as the transfer of pressure from a yielding mass of soil onto adjoining stationary parts. In simpler words, it is the mechanism by which the relative movement of soil due to differential settlement causes shear stresses to develop within the granular material of the embankment base. These shear stresses result in the transfer of loads to the pile caps. (King et al., 2019)

2.1 Arching Models

Arching models allow us to divide the load of the embankment and external loads into an arching load: the portion that is transferred directly to piles, and residual load: the portion that is received by the GR and subsoil. This load division is thus a prerequisite for any subsequent GR dimensioning.

Arching models can be grouped into two families: rigid and limit equilibrium.

2.1.1 Rigid Arching Models

Rigid arch models assume a certain arch shape above which all load, including fill and external loads, is transferred to pile caps and below of which the soil load is carried by the GR and subsoil.

Most prominent among these are Carlson's 1987 model (as reported in Eiksund et al., 2000) in which the arch takes the shape of a 30° angled triangle between piles. The 2D nature of Carlson's model does not account for loads diagonally between piles and thus underestimates the load carried by the GR and subsoil.

Rogbeck et al. (1998) later proposed a 3D extension of Carlson's model, still retaining the fixed triangle angle, but increasing the 2D load as seen in Equation 2.1 below.

$$F_{3D} = \frac{1 + c/a}{2} F_{2D} \quad (2.1)$$

with a being the pile cap width and c the pile center-to-center distance.

The SINTEF method proposed by Svanø et al. (2000) also assumed a 3D soil wedge carried by the GR and subsoil yet assumes a wedge slope $1 : \beta$ with β ranging between 2.5 and 3.5 and needs to be calibrated as a function of the a/c ratio and embankment height H (see Figure 2.1). At lower a/c ratios and lower H , β increases to account for weaker arching effects and vice versa.

The Enhanced Arching Model, commonly known as the Collin (2004) model, assumes a 3D 45° soil wedge: a tetrahedron for triangular pile geometries, and a quadrhedron for square ones. (see Figure 2.2)

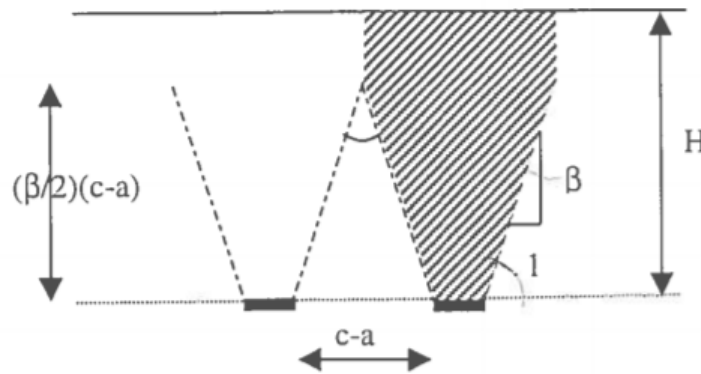


Figure 2.1 – The SINTEF Model. (Eiksund et al., 2000)

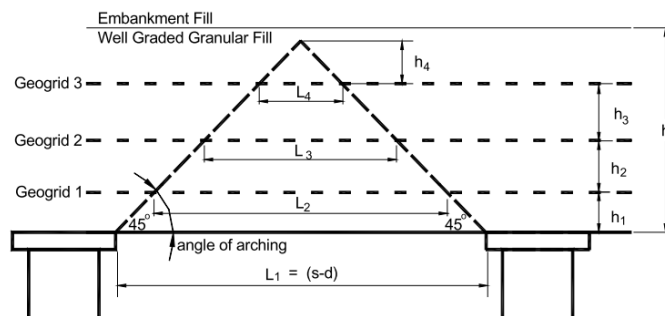


Figure 2.2 – Collin's Enhanced Arching Model. (Collin, 2013)

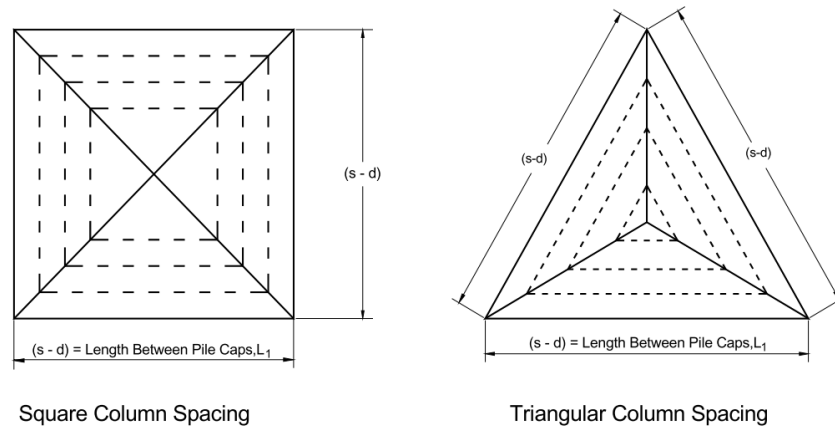


Figure 2.3 – Collin’s Enhanced Arching Model for square and triangular pile grids (Collin, 2013)

It assumes that each layer carries the load of the soil between the considered layer and the one above, thus resulting in the following load, $W_{T,n}$, on a GR layer n :

$$W_{T,n} = \left(\frac{A_n + A_{n+1}}{2} h_n \right) \gamma \cdot A_n \quad (2.2)$$

where A_n is the area of the considered GR under the wedge, A_{n+1} is the area of the following GR under the wedge, h_n is the vertical distance between the considered wedge and the following one, and γ is the unit weight of the load LTP. It is worth noting that the Collin Model can only be applied to GRPEs with 3 or more layers, and is the sole model among the rigid arch models considered that tackles for multi-layered systems.

2.1.2 Limit Equilibrium Arching Models

The following arching models constitute the base of the most prominent European design codes. They are all based on limit equilibrium equations where a certain failure mode is assumed, and arching efficacy equations are derived accordingly.

Hewlett and Randolph

Hewlett and Randolph’s (1988) model is based on semi-circular (2D) and semi-spherical (3D) arches. The model is based on experiments that were conducted without a GR. Two methods of failure, or two limiting conditions, are considered each resulting in a different arching load, the first taking place at the arch crown and the second at the cap (see Figure 2.4). The model then derives equations to calculate efficacy for each of the two limit states. The minimum of the two is chosen for a conservative value of subsoil load.

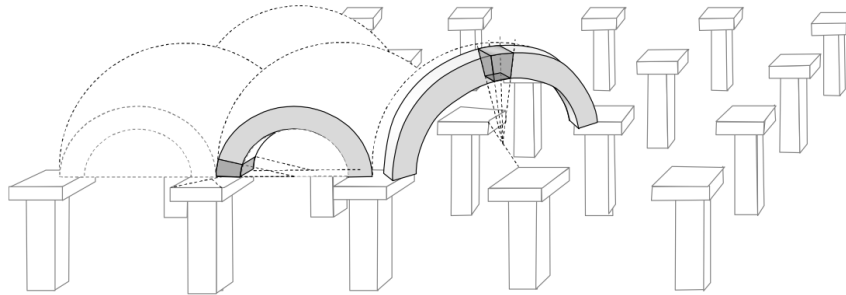


Figure 2.4 – Hewlett and Randolph Model based on two limit states: one at the crown and another at the cap (S van Eekelen 2012)

The arching efficacies are expressed in terms of the pile cap size a , pile center-to-center distance s , embankment height H , and embankment fill friction angle ϕ (detailed out in Section 2.2 below).

The Hewlett and Randolph model was adopted by the British BS8006 guideline (2010) and the French ASIRI guideline (2012) and as one of two possible arch models in the German EBGEO (2011) guideline (expanded upon in Section 2.2 below).

Hewlett and Randolph's model presents two major shortcomings: First, it was derived without a GR, and thus does not account for the increased pile loading transferred from GR to pile caps. Second, it does not account for partial arching in shallow embankments, and might thus overestimate the arching effect and underestimate subsoil loading in such cases.

Zaeske

Zaeske's model is based on a series of 3D scaled model tests that were carried out by Zaeske and Kempert (2002) to investigate both the arching model proposed and the subgrade reaction behaviour, an element of GRPE that was not accounted for in earlier models. The tests tracked the stress field within the embankment with pressure cells at various heights of the embankment and at the pile cap.

Another advantage of the Zaeske model is its ability to account for partial arching in embankments where the arch height is higher than the embankment height, a shortcoming of the Hewlett and Randolph model.

As with other limit equilibrium models, Zaeske and Kempert's equations were developed based on the lower bound theorem of plasticity, where a soil element at the arch crown was considered, and a differential equation for its equilibrium is derived (Equation 2.3). The equation is then solved to find the radial force σ_z acting on the soil element. The stress on subsoil is then found by carrying out this equation to the limit of $z = 0$, i.e. until subsoil is reached (see Figure 2.5).

To circumvent the complication of differential equations, Zaeske and Kempfert developed a dimensionless design graph (Figure 2.7) to find the portion of residual load at a given friction angle (ϕ).

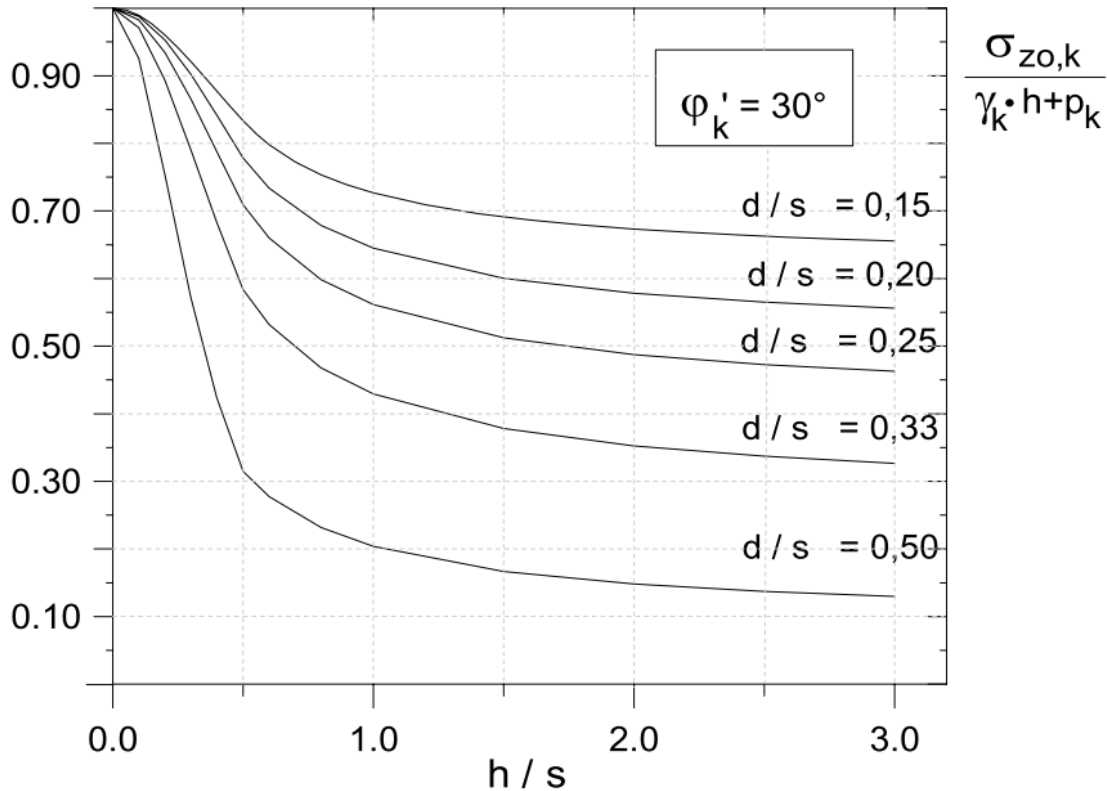


Figure 2.7 – Design chart based on Zaeske’s model at $\phi = 30^\circ$. (Zaeske and Kempfert, 2002)

The Zaeske model was adopted by the German design guidelines EBGE0 (2011) and the Dutch CUR226 (2016) before its 2016 amendment where the concentric arches model was adopted instead.

2.1.3 Concentric Arches Model

The concentric hemispheres model was introduced by Van Eekelen (2013) and detailed out in her PhD thesis (2015).

The model uses a system of both 3D hemispheres and 2D arches. (Figure 2.8) The hemispheres form above the GR square, the area between four pile corners, while the arches form over GR strips, the area lying between two neighboring piles. The hemispheres exert some load on the GR square and transfer the remainder to the pile caps. Likewise the arches exert some load on the GR strips and transfer the remainder to the piles caps.

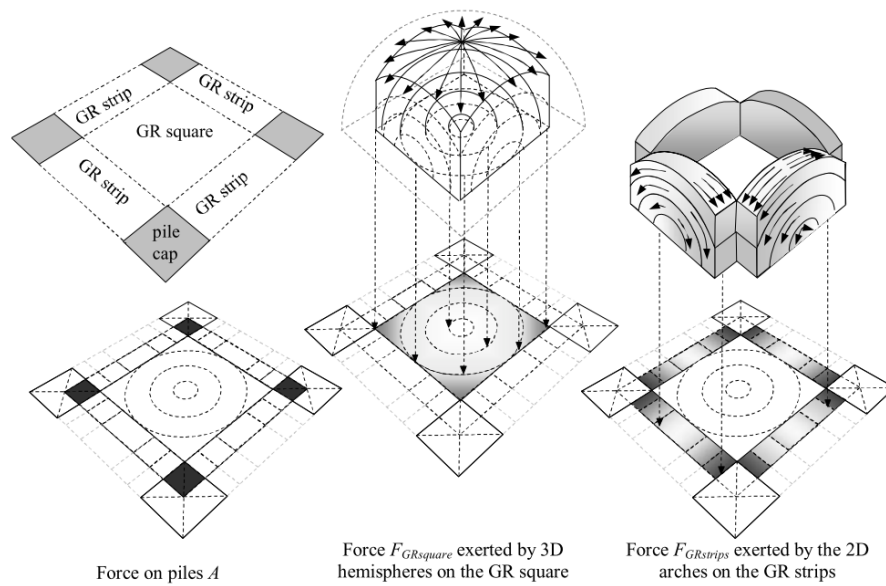


Figure 2.8 – Concentric Arches Model uses 2D arches and 3D hemispheres (van Eekelen & Brugman, 2016)

This arching model results in load concentrations on the GR strips (between adjacent piles), specifically near the pile cap in a way resembling an inverse triangular load distribution (Figure 2.9).

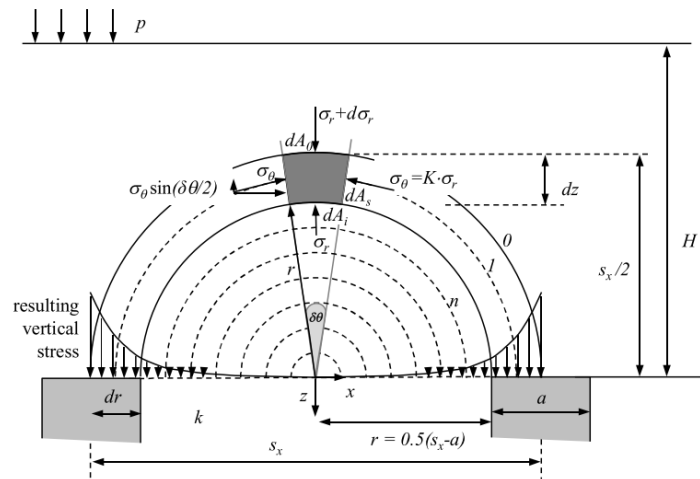


Figure 2.9 – GR load resulting from the Concentric Arches model (van Eekelen & Brugman, 2016)

2.2 European Codes

This section gives a brief overview of the most comprehensive and developed European guidelines for the design of GRPE systems. The Swedish Design code was also considered for relevance to future work. For each of these guidelines, the following will be presented in order:

1. Prerequisite boundary conditions such as limits for embankment height, pile free distance, and free distance to pile cap size ratio;
2. The arching model used and resulting equations for load distribution to arching and residual loads;
3. The method of transforming the residual load into a GR strain value.

Swedish Design Practices - Tk Geo 13 (2016)

Guideline Conditions

- The embankment height must be greater than 1.5 m ($H \geq 1.5m$).
- Thickness of the LTP must be greater than 1.5 times the pile cap free distance ($t \geq 1.5(c - a)$)
- The LTP cover of the top GR should be at least 50cm thick.

The Swedish code also has requirements to ensure lateral displacement and slope stability meet the requirements, but those are beyond the scope of focus of this thesis.

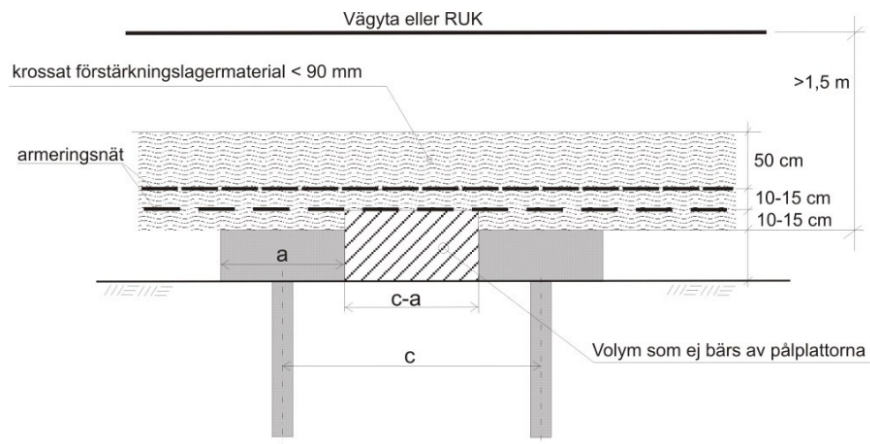


Figure 2.10 – Tk Geo 13 recommendations for georeinforced piled embankments (Trafikverket, 2016)

The Swedish code thus presents the following limitations in regards to GR layering:

- The maximum **free distance** allowed is a fixed function of the embankment height, with no dependence on other design variables like embankment friction angle, sub-soil support, etc.
- The **cover thickness** is limited to 0.5 m with no dependence on other design variables as those listed above.
- The **distance between the geosynthetic layers** is specified at 10 - 15 cm with no dependence on other design variables as those listed above.

British Code – BS8006 (2010)

Guideline Conditions

- The maximum pile free spacing is a function of the pile design capacity Q_p , the embankment load $\gamma.H$, and the surcharge load w_s : $s \leq \sqrt{\frac{Q_p}{\gamma.H+w_s}}$. This is a conservative approach that assumes that all the load will be carried by piles.
- The embankment height must not fall below seventh the pile free spacing: $\frac{H}{s-a} \geq 0.7$
- The GR must be designed with a minimum GR load $W_{T,min} = 0.15.s.(f_{fs}\gamma.H + f_q w_s)$, where f_{fs} and f_q are load factors for soil unit weight load and external loads accordingly. In simpler terms, the GR has to be designed for a minimum load of 15% of the total load.
- The code has specifications for grid spread outside the embankment area (edge limit) through a function of the embankment height H and geometry. Its details are beyond the scope of this paper (see Figure 77 in BS8006 for more details).

Load Distribution

Efficacy is calculated using the Hewlett and Randolph Model for a limit equilibrium state at the crown E_{crown} and the cap E_{cap} . The minimum of the two is used, thus maximizing GR load.

$$E_{crown} = [1 - (\frac{a}{s})^2](A - AB + C) \quad (2.4)$$

$$E_{cap} = \frac{\beta}{\beta + 1} \quad (2.5)$$

with A, B, C , and β are coefficients calculated as a function of pile cap size a , pile center-to-center distance s , embankment height H , and embankment fill friction angle ϕ' as follows:

$$A = [1 - (\frac{a}{s})]^{2(K_p-1)}; B = \frac{s}{\sqrt{2}H} \frac{2K_p - 2}{2K_p - 3}; C = \frac{s - a}{\sqrt{2}.H} \frac{2K_p - 2}{2K_p - 3} \quad (2.6)$$

$$\beta = \frac{2K_p}{(K_p + 1)(1 + \frac{a}{s})} \left[\left(1 - \frac{a}{s}\right)^{-K_p} - (1 + K_p) \left(\frac{a}{s}\right) \right] \quad (2.7)$$

$$K_p = \frac{(1 + \sin \phi')}{(1 - \sin \phi')} \quad (2.8)$$

The GR load W_T is then calculated using the minimum of the two efficacies E_{crown} and E_{cap} as follows:

$$W_T = \frac{s(f_{fs}H + f_q w_s)}{s^2 - a^2} (1 - E_{min}) s^2 \quad (2.9)$$

GR Strain

Once the line load W_T is found, the tensile load T_{rp} (Figure 2.11) of a GR strip with width a is calculated using the following equation. The equation derived with the assumptions of 1) an absence of subsoil support, 2) a parabolic GR deformation shape, 3) a constant GR load W_T along the GR length, and 4) a fixed GR at the pile caps.

$$T_{rp} = \frac{W_T(s-a)}{2a} \sqrt{1 + \frac{1}{6\varepsilon}} \quad (2.10)$$

The equation is set up for strain at the pile cap, and will thus give the maximum strain value. To solve the equation, the strain ε is replaced with T/J , J being the apparent stiffness of the GR at the assumed maximum strain.

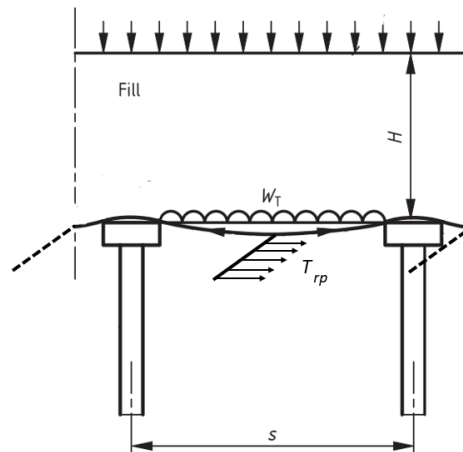


Figure 2.11 – GR line load is used to calculate the tensile force in a meter run of the GR. (BSI, 2010)

German Code – EBGEO (2011)

Guideline Conditions

- The maximum pile free spacing should not exceed 3.0 m for predominantly static loads and 2.5 m for predominantly dynamic ones.
- The embankment height must be greater than 80% the pile free spacing such that $\frac{h}{s-a} \geq 0.8$
- The pile size must be greater than 15% the pile free distance: $\frac{d}{s} \geq 0.15$.
- Distance to the GR should not exceed 0.15 m for single GR, and 0.30 m for multi-layered GR (see Figure 2.12).

Load Distribution

Zaeske's dimensionless design graphs, derived from the model's equilibrium differential equation, are used to find the portion of residual load at a given ϕ .

The stress applied to the pile $\sigma_{zs,k}$ is then found using Equation 2.11:

$$\sigma_{zs,k} = [\gamma_k \cdot H - \sigma_{zs,o}] \cdot \frac{A_E}{A_S} + \sigma_{zs,o} \quad (2.11)$$

where $A_E = s_x s_y$ is the influence area of a pile and $A_S = \pi d^2 / 4$ is the pile contact area. The efficacy E_L , the portion of the total load that is transferred to the piles directly without being first transferred to the GR, is thus calculated as follows.

$$E_L = \frac{\sigma_{zs,k} A_S}{(\gamma_k \cdot H + w_s) A_E} \quad (2.12)$$

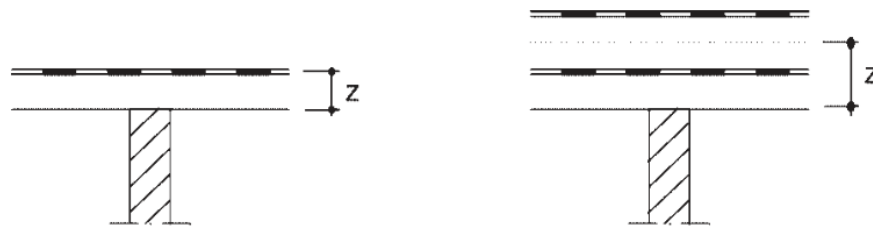


Figure 2.12 – Distance to the GR in single and multi-layered systems according to EBGEO (GSC, 2011)

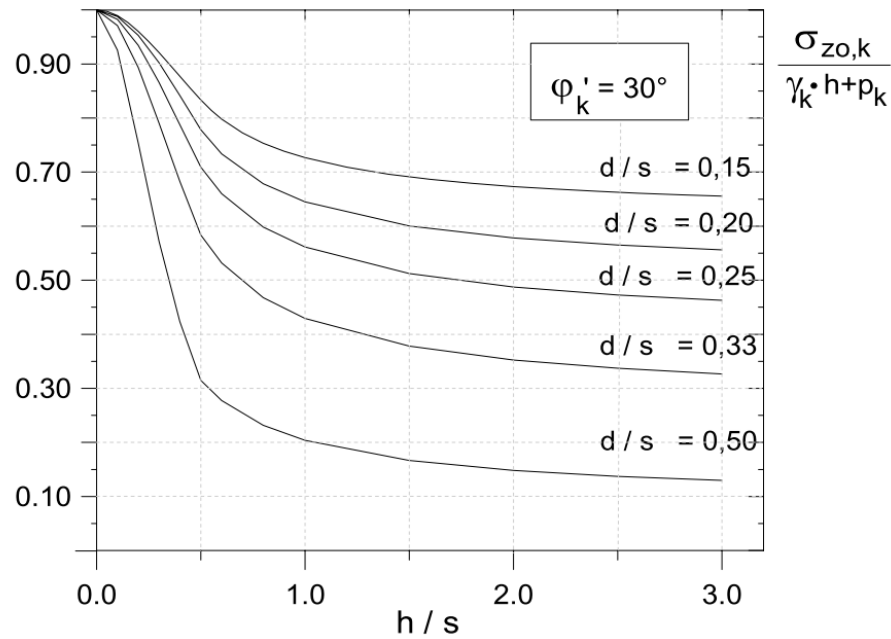


Figure 2.13 – Design charts based on Zaeske's equilibrium equations.(GSC, 2011)

The GR load $\sigma_{z0,k}$ acts the load coverage areas in each direction A_{Lx} and A_{Ly} (see Figure 2.15), where the load acting on A_{Lx} is reduced to a line load between two adjacent piles along the x-direction, and that acting on A_{Ly} , where:

$$A_{Lx} = \frac{1}{2}s_x s_y - \frac{d^2}{2} \operatorname{atan}\left(\frac{s_y}{s_x}\right) \frac{\pi}{180} \quad (2.13)$$

$$A_{Ly} = \frac{1}{2}s_x s_y - \frac{d^2}{2} \operatorname{atan}\left(\frac{s_x}{s_y}\right) \frac{\pi}{180} \quad (2.14)$$

With the load coverage areas and the load calculated, the resultant normal load acting on the GR strip between two adjacent piles is calculated as follows:

$$F_{x,k} = A_{Ly} \sigma_{z0,k} \quad (2.15)$$

$$F_{y,k} = A_{Lx} \sigma_{z0,k} \quad (2.16)$$

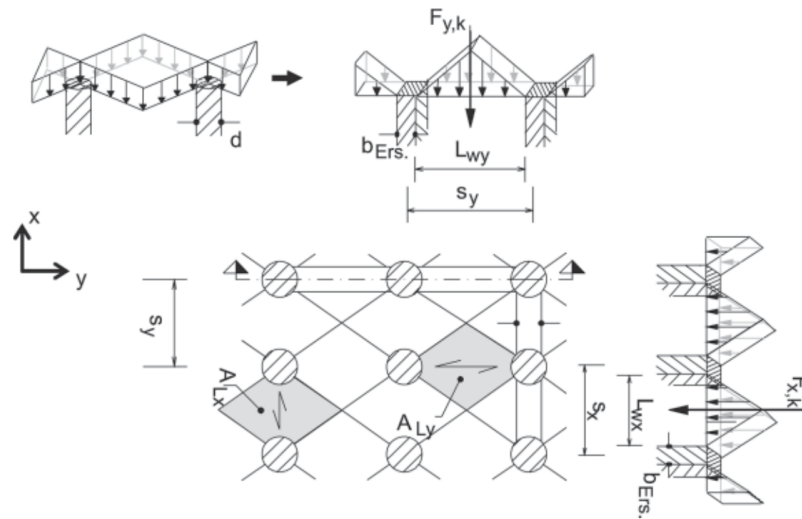


Figure 2.14 – Load distributions areas as defined by EBGEO. (van Eekelen, 2015)

GR Strain

The following design chart in Figure 2.15 is derived given the triangular distribution suggested by Zaeske's model, and allows the user to find the maximum strain in the GR strip as a function the system's geometry, GR characteristics, and subsoil support. Inputs into the chart not previously defined include:

- Subgrade support k_s through the subgrade reaction modulus defined as follows

$$k_s = \frac{E_{s,k}}{t_w} \quad (2.17)$$

where $E_{s,k}$ is the constrained stratum modulus, and t_w is the stratum thickness.

- The characteristic value of axial stiffness J_k in kN/m of the geogrid.

Even though EBGEO states that the strain calculated from the design chart is the maximum strain, van Eekelen, 2015 has pointed out that the strain should in fact be the average strain.

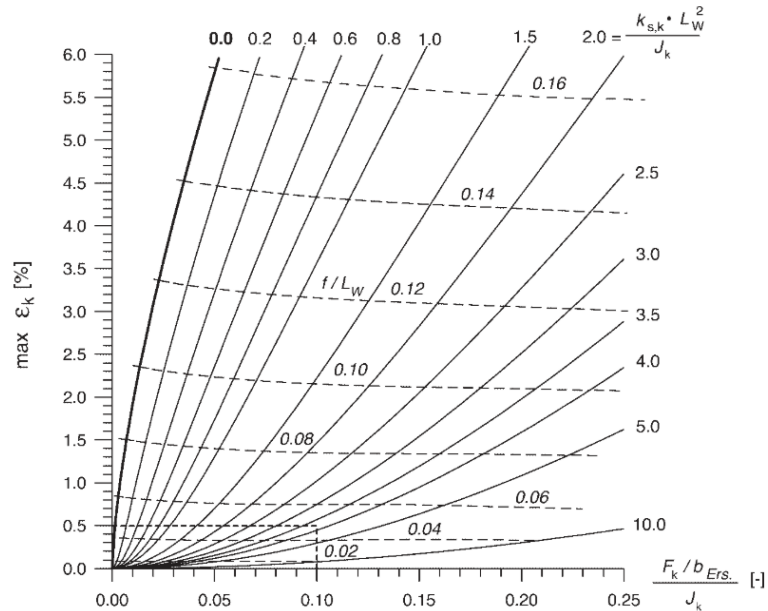


Figure 2.15 – EBGEO design chart to calculate GR strain (GSC, 2011)

Dutch Code - CUR 226 (2016)

Guideline Conditions

- The maximum pile free distance should not exceed 2.5 m;
- The embankment height should range between 0.5 to 4 times the cap free distance with $0.5 \leq \frac{H}{s_d - d_{eq}} \leq 4.0$
- Vertical stress acting on pile can be up to 1450 kPa, but embankments of this type with pile cap vertical stress of up to 2000 kPa have been realized.

Load Distribution

The Dutch code redistributes the applied vertical load into three parts (see Figure 2.16):

- Load part A: load portion transferred directly to piles through arching;
- Load part B: load portion transferred indirectly to the piles through the GR;
- Load part C: load portion carried by the subsoil between the piles.

Arching efficacy is accordingly defined as:

$$E = \frac{A}{A+B+C} = 1 - \frac{B+C}{A+B+C} \quad (2.18)$$

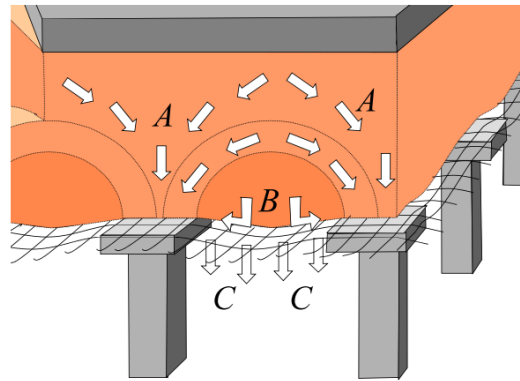


Figure 2.16 – Load distribution according to the Dutch CUR 226 guideline. (van Eekelen & Brugman, 2016)

The load distribution requires defining the following geometric entities (see Figure 2.17):

- $H_{g,3D}$: Width of the GR square on which the 3D hemispheres exert load
- $H_{g,3D}$: Height of the largest 3D hemisphere
- L_{2D} (L_{x2D} , L_{y2D}): Length of the GR strip, oriented along the x or y axis, on which the 2D arches exert load
- $H_{g,2D}$: Height of the largest 2D arch
- L_w (L_{wx} , L_{wy}): clear distance between two adjacent piles

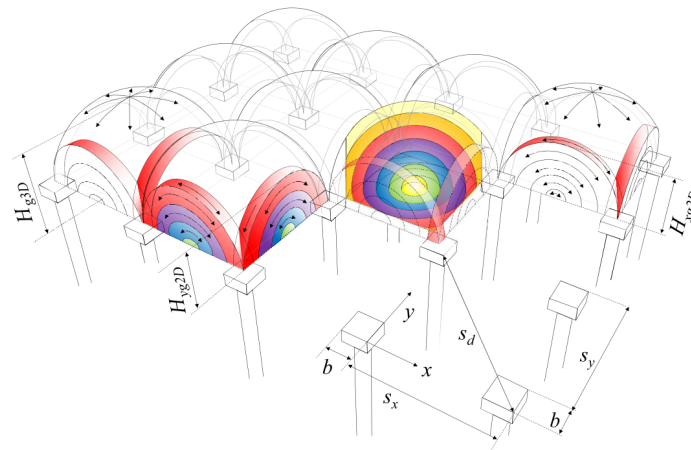


Figure 2.17 – Load distributing geometries defined by the Dutch CUR 226 guideline (van Eekelen & Brugman, 2016)

The code defines 3 load entities:

- $F_{GR\ square}$: Load exerted by a 3D hemisphere on the GR square between 4 piles (in kN/pile, see Figure 2.18). It is calculated using two calculation parameters P_{3D} and Q_{3D} , in addition to the geometry of the GR square (via b_{eq} and L_{3D})
 - P_{3D} : Calculation parameter, a function of the 3D arch height $H_{g,3D}$ and passive earth pressure coefficient K_p , and the vertical soil weight load γH .
 - Q_{3D} : Calculation parameter, a function of passive earth pressure coefficient K_p
- $F_{transferred}$: Load transferred along the 3D hemispheres to the 2D arches, and applied to the 2D arches as a surcharge load. It is used in the calculation of $F_{GR\ strip}$.

$$F_{transferred} = \gamma H \cdot L_{wx} \cdot L_{wy} - F_{GR\ square} \quad (2.19)$$

- $F_{GR\ strip}$: Load exerted by the 2D arches on the GR strip between two adjacent piles (in kN/pile, see Figure 2.19). It is calculated using two calculation parameters P_{2D} and Q_{2D} , in addition to the geometry of the GR strip (via b_{eq} and L_{2D})
 - P_{2D} : Calculation parameter, a function of the 2D arch height $H_{g,2D}$, passive earth pressure coefficient K_p , and the total vertical load including the transferred load
 - Q_{2D} : Calculation parameter, a function of passive earth pressure coefficient K_p

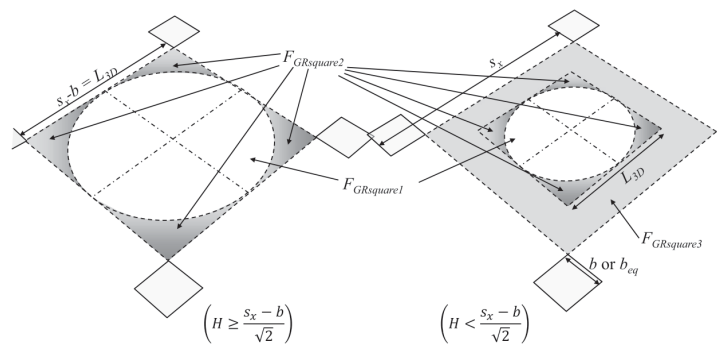


Figure 2.18 – GR square geometry in the Dutch CUR 226 guideline (van Eekelen & Brugman, 2016)

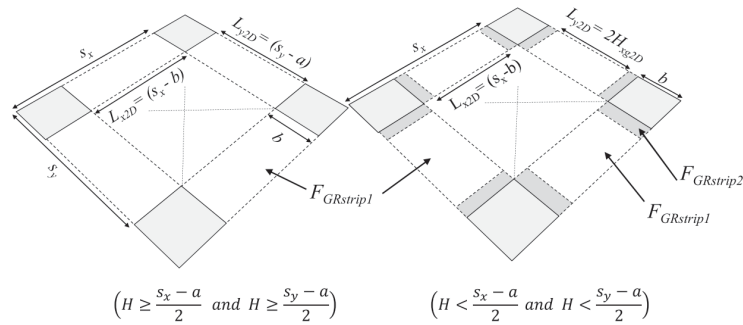


Figure 2.19 – GR strip geometry in the Dutch CUR 226 guideline (van Eekelen & Brugman, 2016)

Once the above loads are calculated:

- The residual load is calculated by adding the square and strip portions of the GR load, $B + C = F_{GR,square} + F_{GR,strip}$.
- The remainder of the force is applied to the pile caps: $A = \gamma H A_p - (B + C)$

GR Strain

With the Residual Load (B+C) calculated, the average load acting on the GR strips in both the transverse and longitudinal direction is found by dividing the force onto area of the GR strips using $q_{av} = \frac{B+C}{b_{eq}(L_{wx}+L_{wy})}$.

The Dutch guideline presents two GR load distributions, a uniform (uni) and inverse-triangular (inv) as seen in Figure (2.20)

Under the chosen load, the GR displaces by a distance $z(x)$ described by equations below. As can be seen, the equations account for subsoil support through the modified subgrade reaction value K :

$$\alpha = \sqrt{K/T_H} \tag{2.20}$$



Figure 2.20 – Uniform and inverse triangular load distributions on the GR in the Dutch CUR 226 guideline

The slope of GR displacement $z'(x)$ is then used to find the tensile force in through the GR along the GR length.

$$T = T_H \sqrt{1 + z'(x)^2} \quad (2.21)$$

The guideline then calculates the average strain $\epsilon_{average}$ using a constitutive equation – that is based on the physical definition of strain as the product of stiffness J by the tensile force T - and a geometric one – as the change in length of the GR divided by its original length. The two strain expressions are a function of the horizontal component of the tensile force T_H : They are thus equated to find the value of T_H .

$$\epsilon_{const,average} = \frac{\frac{1}{J} \cdot \int_{x=0}^{x=0.5L} T(x) dx}{\frac{1}{2}L} \quad (2.22)$$

$$\epsilon_{geometric,average} = \frac{\int_{x=0}^{x=0.5L} dx \sqrt{1 + z'(x)^2} - \frac{1}{2}L}{\frac{1}{2}L} \quad (2.23)$$

The following flow chart (Figure 2.21) summarizes the Dutch code’s calculation steps. It shows the steps followed and intermediate geometries and calculation constants used to go from the input variables ($s_{x/y}$, b , K_p , H , γ) to the output (Arching load A and Residual load B+C).

Comparative Review

Major differences between the British BS8006 (2010) following Hewlett and Randolph’s model, the German EBGeo (2011) following Zaeske’s model, and the Dutch Code CUR 226 (2016) following van Eekelen’s (concentric arches) model following an extension of the two are summarized in Table 2.1) below.

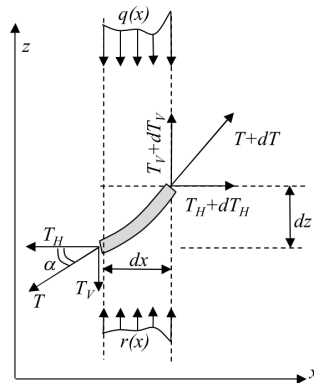


Figure 2.22 – Tensioned membrane element used by all reviewed guidelines to derive strain as a function of GR load (van Eekelen, 2015)

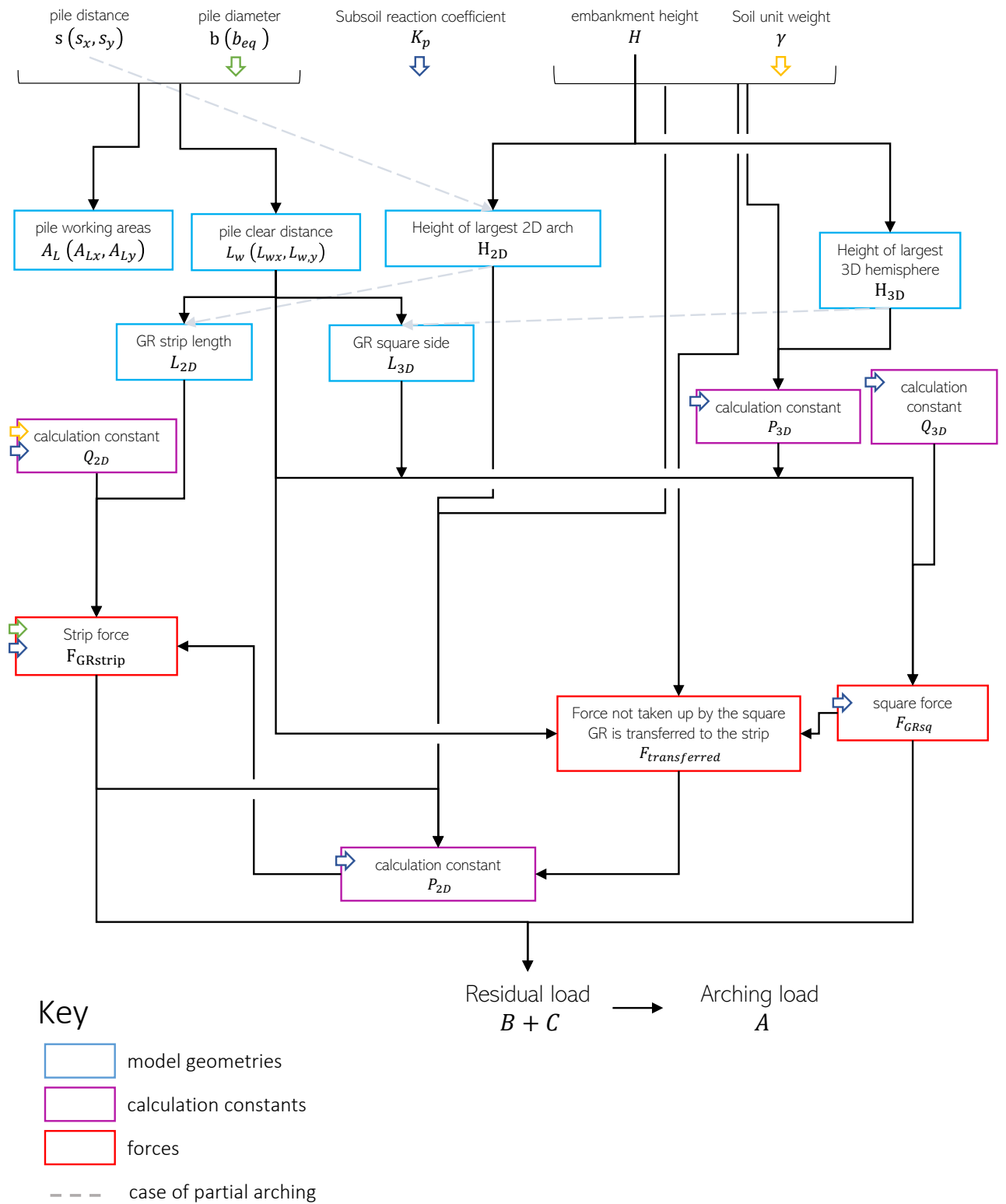


Figure 2.21 – Flow chart summarizing the Dutch Code

Table 2.1 – Comparative Summary of major European design guidelines for the design of GRPEs

	BS8006 (2010) <i>Hewlett Randolph</i>	EBGEO (2011) <i>Zaeske</i>	CUR (2016) <i>Concentric Arches</i>
Arching Model	Semi circular arches/spheres based on the equilibrium of a crown or pile element. Minimum of the two is used	Multi-scale arches based on the equilibrium of a crown element	Concentric 2D arches and 3D hemispheres
Partial arching	Not accommodated	Accommodated by removing arches above the embankment height	Accommodated through different load distribution based on whether arching height is reached
Subsoil support	Disregarded as a conservative approach	Considered through subgrade reaction modulus k_s , only considers soil under GR strip	Considered through a modified subgrade reaction modulus K , considers soil under the whole subsoil
Load distribution over GR	Uniform	Triangular	Offers inverse triangular and uniform, Inverse triangular – more suitable for poor subgrade Uniform – more suitable for stiffer subgrades
GR Load to strain	$T_{rp} = \frac{w_T(s-a)}{2a} \sqrt{1 + \frac{1}{6\varepsilon}}$ derived using an elastic tensioned membrane (Figure 2.22) with disregard to subsoil support. The equation can be solved by replacing ε with T/J and solving for T	Dimensionless design graphs (derived using the same elastic tensioned membrane setup and assumptions of the BS8006 equation but including subsoil support) as a function of: <ul style="list-style-type: none"> · k_s-subgrade support · L_w-length of GR strip · J-stiffness of GR, incl. creep effect · F-resultant vertical load on GR · b-width of GR strip 	Derived using the same elastic tensioned membrane setup. Expressions for $z(x)$ and $z'(x)$ were derived for both a uniform and inverse triangular. Geometric and constitutive expressions of strain are equated to find tensile force through the GR and max strain

Available literature comparing the accuracy of prediction of these guidelines is reviewed below.

van Eekelen et al., 2008 carried out measurements over the span of two years on a full-scale model of basal reinforced piled embankment, the Kyoto Road case study built in Giessenburg in the Netherlands. The test measured the load received directly by the piles and that received by the piles through the GR. The study concludes that EBGEO over-predicts the direct loads on piles, yet results in the best prediction of residual load. The paper deems this overestimation of the arching load is practically inconsequential for the end purpose of dimensioning the GR. The BS8006 vastly overestimated the residual load (i.e. the GR load in the case of BS8006).

van Eekelen et al., 2012 carried out a series of 3D laboratory model tests on piled embankments. The tests measured and analysed load distribution, system deformations, and GR strains then compared them with predictions of EBGEO (2011). In regards to arching, the model seemed to under-predict the arching load and thus overestimate the residual load, thus resulting in a conservative analysis. The paper hypothesizes that this is due to EBGEO's inability to capture the phenomena of improved arching due to subsoil consolidation which was shown in measurements. In regards to GR strain, the model overestimates GR strains by more than a double at lower strain levels. The overestimation of GR strains is linked to two main factors: the triangular GR load distribution assumed by EBGEO and the mobilization of only the subsoil directly under the GR strip instead of the whole GR area. In that regard, the paper shows that changing EBGEO's GR load distribution shape from a triangle to an inverse triangle shape, and mobilizing a bigger portion of the subsoil, give results that better match measurements. These suggestions reflect some of the major differences between the EBGEO and the newer Dutch code.

Bhasi and Rajagopal, 2015 used a 3D model of a GRPE calibrated according to Liu et al. (2007) using 1 to 3 layers of GR and with varying heights of embankment. They compared the single layer case to the analytical predictions for tensile stress of Hewlett and Randolph's model (1988), EBGEO (2011), and BS8006 (2010, following Van Eekelen's modifications). They also compared the multi-layered case results to predictions of Collin's model (2005). Results showed that the EBGEO method, using Zaeske's arching model, gave the most accurate predictions of pile loads by arching, while BS8006 model underestimated this value by close to 35%. In regards to GR load, both EBGEO and BS8006 overpredict it, but BS8006 gives much higher values likely due to its neglect of subsoil support. Under low subgrade support values, tensile forces predicted by EBGEO and BS8006 tend to converge, as predicted. For multi-layered systems, Collin (2005) seems to underestimate the tensile load developed in the GRs, with the error being highest for the bottom layer and for more stiff GRs.

van Eekelen et al., 2015 analysed measurements from seven full-scale tests and four series of scaled model experiments. The paper compared measurements to analytical results using different combinations of a) Arching models: Hewlett and Randolph's, Zaeske's,

and the Concentric Arches model; b) Load distributions: uniform, triangular, and inverse triangular; and c) Subsoil mobilization: under the full GR and only under the GR strip. The Zaeske model with triangular load and limited subsoil support (Zs-tri-str) and the Hewlett and Randolph model with triangular load and limited subsoil support (HW-tri-str) resulted in the most overestimation of GR strain (average overestimations of 146% and 189% respectively). On the arching model choice, both the Concentric Arches and Zaeske's models result in conservative results for GR strain, but the concentric arches model gives more accurate predictions with an average overestimation of 16-34% compared to 24-42% for Zaeske's. The paper also concludes that Zaeske's arching is overly sensitive to the fill friction angle, resulting in underestimations of arching action at lower angles and overestimations at higher ones. In regards to the effect of subsoil support on model appropriateness, the CA-inv-all model gives the most accurate results in cases of low to no subsoil support, while the CA-uni-all gives better results in cases of high subsoil support.

Khansari and Vollmert, 2018 used field data collected at a GRPE structure in Hamburg to compare the predictions of BS8006 (2010), EBGEO (2011), and CUR-226 (2016) for GR load, deflection, and strain and pile load. All three models resulted in an overestimation of GR load (189%, 15% and 32% by EBGEO, BS8006 and CUR-226, respectively) and a large overestimation of forces on the pile head (43%, 75% and 89% by the models in EBGEO, BS8006 and CUR-226, respectively). The paper also concludes that EBGEO's triangular distribution of GR load is the farthest away from measured values while the uniform distribution is the closest, likely due to the firm subsoil at the site. BS8006's shortcoming lies in its dramatic overestimation of GR deflection due to its neglect of subsoil support. The paper concludes that despite its overestimation of both GR deflection and pile load, CUR-226 gave the most accurate predictions of GR load and associated strains and settlements when a uniform GR load distribution and a stiff subsoil is used.

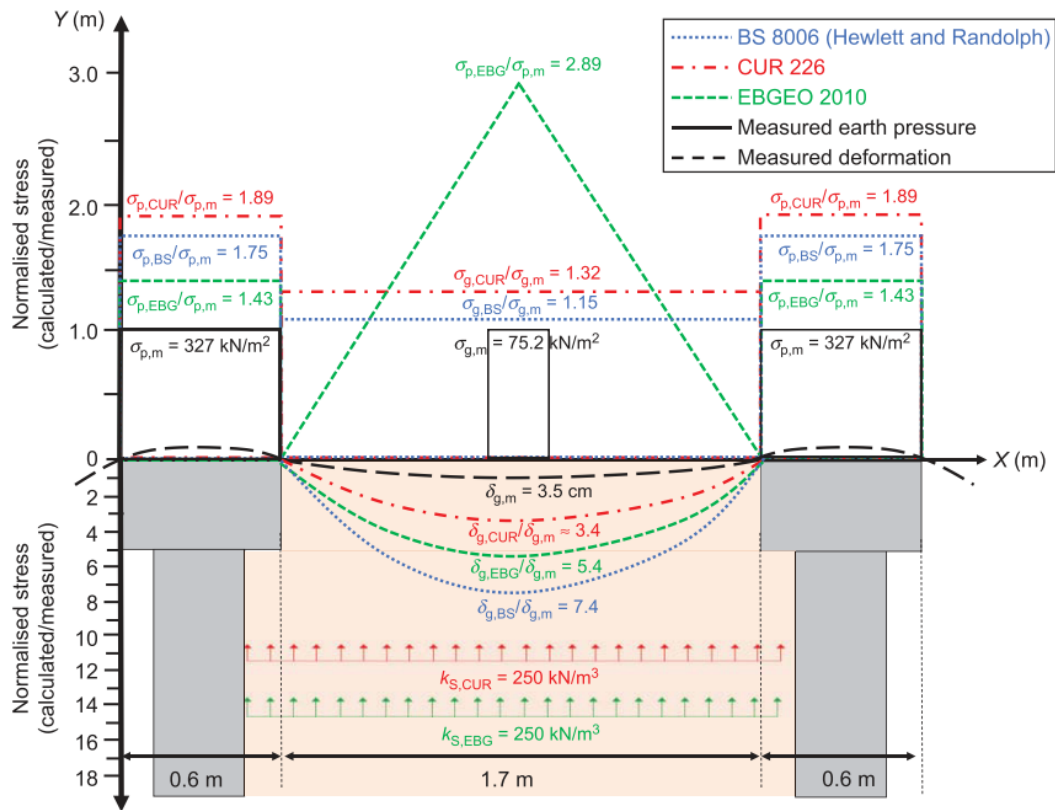


Figure 2.23 – Comparisons of guidelines considered in Khansari and Vollmert, 2018 compared to measured values at a GRPE site in Hamburg.

2.3 Conclusion

This chapter presents the most prominent arching models, including rigid and limit equilibrium arching models. Rigid models discussed include the 2D Carlson model (1987), its 3D extension by Rogbeck et al. (1998), the SINTEF model (2000), and the Collin (2004) model. Limit equilibrium models discussed are the Hewlett and Randolph model (1988), the Zaeske model (2002), and the Concentric Arches model (2013).

The chapter also gives an overview of the most developed European guidelines for the design of GRPEs, including the German EBGEO 2011, the British BS8006 2010, and the Dutch CUR-226 2016.

Based on a review of the literature assessing the accuracy of BS8006 (2010), EBGEO (2011), and CUR-226 (2016) in predicting GRPE system loads and displacements, the following points can be deduced:

- Whether the arching load is underestimated or overestimated is highly dependent on the GRPE system parameters. For Zaeske's arching model adopted by EBGeo (2011), the arching load estimation is very sensitive to the embankment fill friction angle ϕ , overestimating the arching load at lower ϕ values (e.g. van Eekelen et al., 2008; Khansari and Vollmert, 2018) yet giving better results for sand material at higher ϕ values (e.g. van Eekelen et al., 2012; Woerden case in van Eekelen et al., 2015).

This sensitivity to ϕ is also noted in the Hewlett and Randolph model adopted by BS8006 (2010), resulting in underestimations at higher ϕ values (e.g. the Woerden and Houten cases in van Eekelen et al., 2015) and giving better predictions (moving towards overestimations) at lower values (e.g. Khansari and Vollmert, 2018, PFA embankment in Bhasi and Rajagopal, 2015).

- In regards to the GR load distribution, the literature review shows this choice is highly dependent on subsoil support: a uniform load distribution has proved to be more suitable for higher subsoil support, while an inverse triangle distribution is more suitable for low subsoil support. The Zaeske triangular distribution, however, seems the farthest away from measurements, giving the highest overestimations of GR deflection and strain among the three shapes. This will be checked for in Chapters 5, the results and discussion of the PLAXIS 2D modelling.
- All considered guidelines are prone to underestimating arching with time: as consolidation increases with time, the arching effect grows stronger, which might not have been accounted for in the initial phase of calculation when the subsoil has not undergone consolidation yet. This might thus result in an overestimation of GR load in time.

Chapter 3

Modelling GRPE Systems in PLAXIS 2D

PLAXIS 2D is a finite element package for two-dimensional analysis of deformation and stability in geotechnical engineering and rock mechanics. It is used to track stresses and displacements in embankments, excavations, foundations, and tunnels.

In 2012, PLAXIS introduced the Embedded Beam Row element which allows for a simplified method of representing rows of identical piles or beams that extend perpendicularly out-of-plane (Plaxis2D, 2019a). The accuracy of this representation has been assessed by J. Sluis (2012) as documented in Brinkgreve et al., 2017. However, no assessment has been done on this feature in the presence of GRs, particularly given the theory behind the element, and its problematic practical implications when implemented in the presence of a GR. This is discussed in Section 3.3 below.

This chapter documents the most relevant features of PLAXIS 2D that were used in constructing the GRPE model. It was intentionally written in a detailed manner, presenting the theory behind these features, to justify their use in the following chapter.

3.1 Model Geometries

PLAXIS 2D offers two types of model geometries: plane strain and axisymmetric (see Figure 3.1):

- A plane strain model is used for geometries with a generally uniform cross section, from both a geometric and loading perspective, in the direction perpendicular to the cross section (z-direction). Examples of such structures include plates under in-plane loading, pipes under internal pressure, uniform embankment extending along roads, etc.

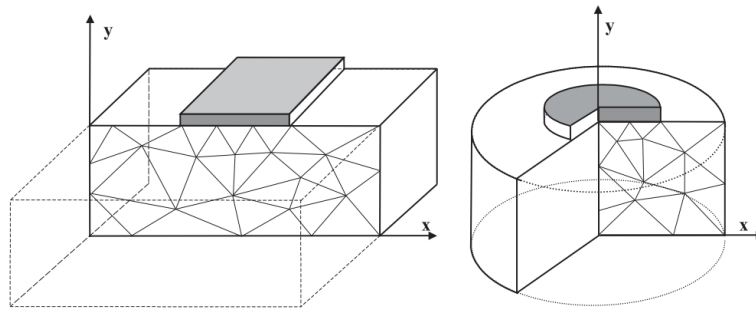


Figure 3.1 – Plane strain (left) vs axisymmetric (right) models (Plaxis2D, 2019a)

- An axisymmetric model is used for circular structures with a generally uniform cross section in the radial direction in regards to geometry and loading scheme. Examples of such structures include single foundation piles and singular sources of ground vibration.

From the start, an axisymmetric model was deemed inappropriate for modelling a GRPE model for obvious reasons: although a single pile is in itself an axisymmetric structure, the arching effect taking place between a minimum of two piles cannot be axisymmetrically modelled.

A plane strain model can accurately represent an embankment's geometry and loading scheme, both extending uniformly in the z-direction. The piles, although also uniformly extending under the embankment in the z-direction, are not continuous in that direction due to their grid-geometry: their modelling in a plane strain model will result in a wall-like structure that extends in the out-of-plane direction. This is where EBR elements serve an alternative, as is explained below.

3.2 Soil Models

The soil layering of the subsoil is defined by creating a borehole and defining its constituting layers. Each layer in the borehole has a defined width and each soil's parameters are input according to a predefined material model.

The embankment on the other hand is constructed as a soil polygon that can be later activated or deactivated through the staged construction explained later. Material models define how PLAXIS 2D analyses the stress-strain behaviour of the soil being modelled, with the software supporting different models to simulate the behaviour of a soil. Expectedly, when a sophisticated model is chosen, the number of input parameters characterizing the soil increases.

This paper will only describe the material models used in the creation of the GRPE model, but descriptions of other material models used in PLAXIS can be found in the software manual.

Mohr-Coulomb (MC) model - This is a familiar linear elastic perfectly-plastic model. Input parameters are fairly basic and include unit weight γ , a constant young's modulus E , Poisson's ratio ν , cohesion c , friction angle ϕ , and dilatancy ψ . The MC model is often used for modelling frictional embankment fills, (Van den Boogert) and is often used as a preliminary model before more sophisticated models are needed.

Hardening Soil (HS) model - This is a more advanced elastoplastic model that accounts for stiffness changes as a function of stress states. In contrast to the elastic perfectly plastic MC model, the yield surface of the HS model is not fixed with respect to the principal stress state, but can expand due to plastic straining.

Accordingly, instead of a single constant parameter for stiffness, as is the case for the MC model, the HS model requires 3 stiffness values E_{oed}^{ref} , E_{50}^{ref} , E_{ur}^{ref} and a power m :

- The oedometer stiffness E_{oed}^{ref} , also termed the elastic soil stiffness, captures the effect of primary compression σ_1 on plastic straining. This value is derived at a reference pressure p^{ref} - conventionally $100kPa$ - from an oedometer test as shown in Figure 3.2 below. In the absence of an oedometer test, PLAXIS suggests the use of an approximation $E_{oed}^{ref} \approx E_{50}^{ref}$.
- The triaxial loading stiffness E_{50}^{ref} , also termed the plastic soil stiffness, captures the effect of primary deviatory loading ($\sigma_1 - \sigma_3$) on plastic straining. This value is also derived at a reference pressure p^{ref} - conventionally $100kPa$ - from a triaxial test as shown in Figure 3.3 below. In the absence of a triaxial test, PLAXIS suggests the use of an approximation $E_{oed}^{ref} \approx E_{50}^{ref}$.

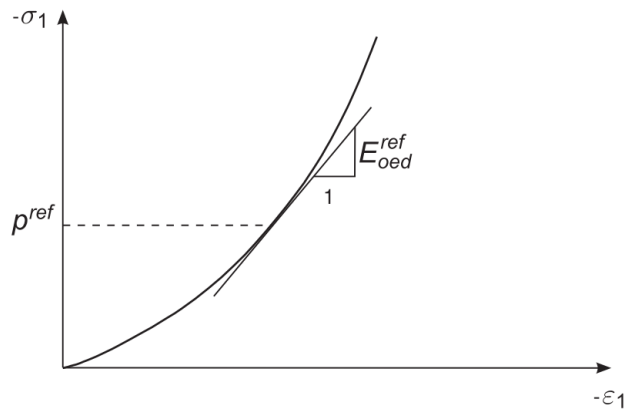


Figure 3.2 – Oedometer stiffness at a reference stress p^{ref} (Plaxis2D, 2019b)

- In addition to the plastic strains in primary loading (tracked through E_{50}^{ref} , the model captures for elastic strains developing both in primary loading and unloading/reloading through E_{ur}^{ref} . This stiffness modulus is also derived from a triaxial test at a reference pressure p^{ref} . In the absence of a triaxial test, PLAXIS uses an $E_{ur}^{ref} = 3E_{50}^{ref}$.
- The power (m) dictates the stress dependency of stiffness, implying weaker dependencies lower m values. Janbu (1963) reports values of m around 0.5 for Norwegian sands and silts, and von Soos (1990) reports various different values in the range $0.5 < m < 1.0$. Satibi (2014) reports an m value of 0.5 for sands and 1.0 for clays.

$$E_{oed} = E_{oed}^{ref} \left(\frac{c \cos \varphi - \sigma'_1 \sin \varphi}{c \cos \varphi + p^{ref} \sin \varphi} \right)^m \quad (3.1)$$

$$E_{50} = E_{50}^{ref} \left(\frac{c \cos \varphi - \sigma'_3 \sin \varphi}{c \cos \varphi + p^{ref} \sin \varphi} \right)^m \quad (3.2)$$

$$E_{ur} = E_{ur}^{ref} \left(\frac{c \cos \varphi - \sigma'_3 \sin \varphi}{c \cos \varphi + p^{ref} \sin \varphi} \right)^m \quad (3.3)$$

In the absence of the above described stiffness moduli, PLAXIS 2D allows for using the following alternative input parameters, which can be derived from a primary compression test like a odometer or a CRS test (see Figure 3.4):

- Compression index C_c , the slope of the void ratio e to \log . of primary compression effective stress $\log \sigma'_1$ beyond preconsolidation stress, $C_c = \frac{\Delta e}{\log(\sigma'_1)}$.

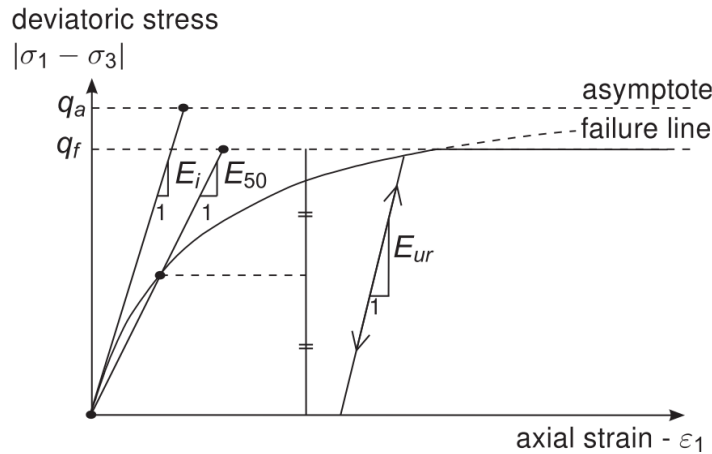


Figure 3.3 – The Hyperbolic stress-strain relation in primary loading for a standard drained triaxial test (Plaxis2D, 2019b)

- Swelling index C_s , the slope of the rebound curve of ratio e versus \log . of effective stress $C_s = \frac{\Delta e}{\log(\sigma'_f)}$
- Initial void ratio e_o , or the in-situ void ratio of soil under study.

Satibi (2014) points out that out of the three stiffness moduli, E_{oed}^{ref} has the highest influence on the settlement of the embankment and thus of subsoil settlement compared (see Figure 3.5). However, such a value seems to have very little influence on arching action. He also pointed out little influence of the power (m) on either settlement or arching action.

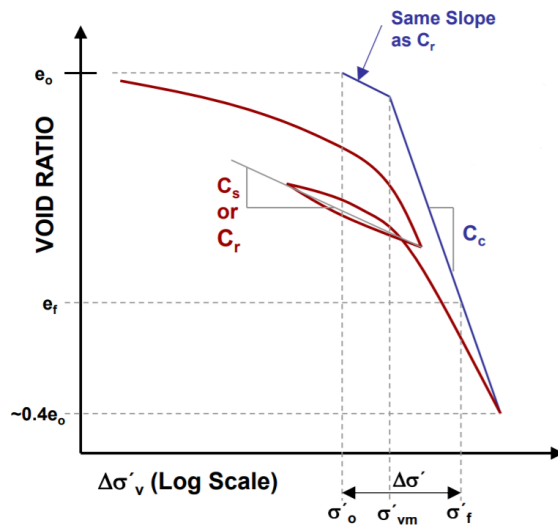


Figure 3.4 – Compression and swelling indices can be found by plotting Void ratio vs log-stress under one dimensional compression (Plaxis2D, 2019b)

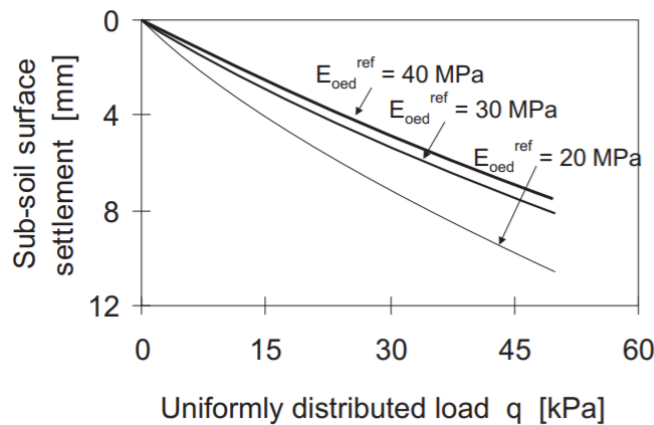


Figure 3.5 – Surface settlement is most sensitive to E_{oed} (Satibi, 2014)

Soft Soil (SS) – These include near-normally consolidated clays, clayey silts and peat as defined by PLAXIS’s Material Manual. Such soils share a high degree of compressibility characterized by much lower odometer moduli in the range of 1 to 4 MPa. Similar to the HS model, the SS model has a stress-dependent stiffness, but one that is more linear due to the near-1 value of the power m and the low cohesion c . Input parameters to this model are from the Clam-Clay model:

- The modified compression index λ^* which captures the compressibility of the material during primary loading. It is the slope of isotropic strain versus the log. of primary effective stress.
- The modified swelling index κ^* which captures the expansion of the material during primary unloading. It is the slope of isotropic unloading strain versus the log. of primary effective stress at a reference primary pressure.

In case an isotropic compression test is not available, results of a primary compression analysis, i.e. compressibility and swelling indices C_c and C_s in addition to the initial void ratio e_o , can be used.

3.3 Embedded Beam Row Element

The Embedded Beam Row element was introduced by PLAXIS 2D in 2012 to attempt at more accurately modelling piles in 2D. Previously, pile rows were modelled either as plates or anchor-to-anchor connections.

Modelling piles as plates results in wall structures extending in the z-direction. This required that a modeller separately convert the per pile properties to per unit length as to more accurately portray a pile row. As for the soil-pile interaction, interface elements could be used yet are limited in interfaces lying in the 2D plane. Plate representations were thus most appropriate to pile rows with low out-of-plane spacing ($\frac{L_{space}}{D} \leq 2 - 3$ as recommended by PLAXIS 2D).

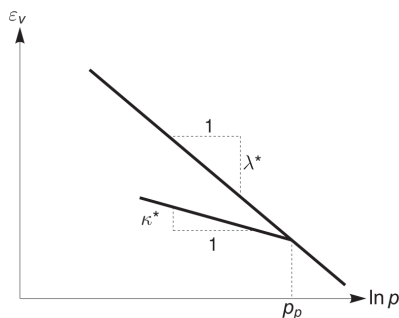


Figure 3.6 – Modified compression and swelling indices found by plotting volumetric strain vs. natural log of stress at a reference pressure. (Plaxis2D, 2019b)

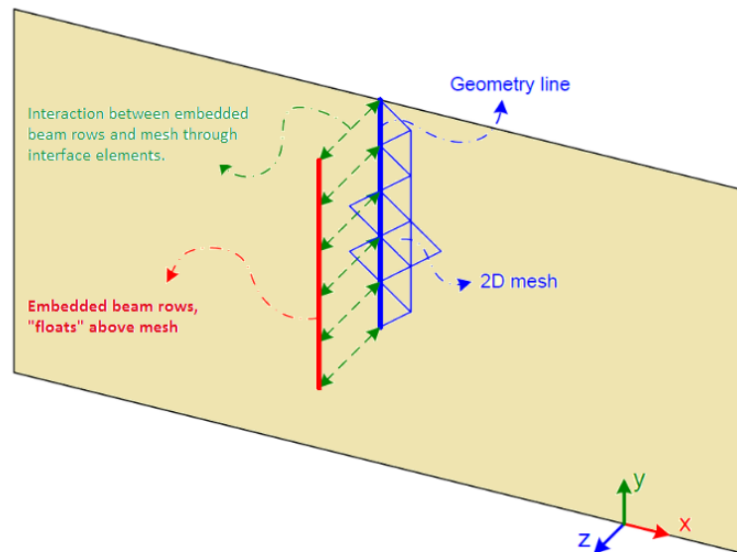


Figure 3.7 – EBR element can be seen as superimposed on the 2D mesh (Plaxis2D, 2019a)

Modelling them as node-to-node anchors simulates them as a two-node spring with a specified stiffness, which can accommodate axial interactions - through compression and tension - but not lateral ones.

The Embedded Beam Row element is a line element that can model a row of long slender members, like piles and rock bolts, used to transmit loads to the surrounding soil or rock. This line element has 3 degrees of freedom at each of its nodes: two translational u_x, u_y and an in-plane rotational θ_z (see Figure 3.7). The element can transfer this load through a special out-of-plane interface that connects it to surrounding soil in the out-of-plane direction. In this sense, the element can be thought of as not simply existing ‘in’ the 2D model plane but rather as being ‘superimposed on’ its mesh, as Sluis (2012) describes it. Displacements of the soil mesh connected to the Embedded Beam Row thus represents the average displacement of this element in the out-of-plane direction.

It is thus unnecessary to specify a separate interface element between the EBR element and the soil, as it is already built into the EBR material properties.

The EBR element can be chosen to behave as a pile, rock bolt, or grout body. The following will focus on the material properties of a pile. To characterize a pile EBR, the following is required as input parameters:

- *Connection point* – can be set to either the top or bottom node of the EBR element. This connection point is either set to be rigid, hinged, or free. A rigid connection implies that both the displacement and rotation of the EBR node is couple with those of the element it is connected to. This applies to cases where the pile is connected to rigid plated at the top for example. A hinged connection implies coupling in only

the rotational degree of freedom, while a free connection point implies a decoupled node.

- *Material type* – can be set to Elastic, Elastoplastic, or Elastoplastic $M - \kappa$. In the case of a concrete pile, an Elastoplastic material type is chosen.
- *Material Properties* – includes the pile’s Young’s modulus E and unit weight γ .
- *Beam type* – can either be chosen from a predefined list (massive circular beam, circular tube, massive square beam) or user defined. A diameter should be input for circular beams, a width for a square beam, and a thickness for tube beams. This cross-sectional size factors into determining the element’s stiffness factors, as will be explained later.
- *Spacing $L_{spacing}$* - the distance separating adjacent piles of the row in the out-of-plane direction. This spacing also factors into determining the element’s stiffness factors, as will be explained later.

The interaction of the element with the surrounding soil is determined by PLAXIS 2D by means of a special interface elements along the beam length. This interface follows an elastoplastic model, where the plastic behaviour is governed by user-input values for skin resistance and base resistance:

- **Skin Resistance F_{skin}** - is entered in units of force per unit member length, and can take one of three forms: linear, multi-linear, or layer dependent. In the case of a linear skin resistance, the skin resistance at the top and bottom of the member is input by the user as $T_{skin,start,max}$ and $T_{skin,end,max}$. In the case of multi-linear skin resistance, the user inputs into a table varying skin resistance values at varying member lengths. In the case of layer-dependent resistance, the program uses the surrounding soil’s values parameters cohesion c , friction angle ϕ , and interface strength reduction factor R_{inter} to calculate a depth dependent skin resistance. As such, one of the following values for skin resistance apply:

$$\text{Linear : } F_{skin} = \frac{1}{2}(T_{skin,start,max} + T_{skin,end,max}) \cdot L$$

$$\text{Multi-linear : } F_{skin} = \sum_1^{n-1} (L_{i+1} - L_i) \cdot \frac{T_{i+1} + T_i}{2}$$

$$\text{Layer-dependent: } F_{skin} = \int_0^L 2\pi R_{eq} \tau_i$$

$$\text{where } \tau_i = R_{inter}(c + \sigma'_n \tan \phi)$$

In all the above cases, an (EBR-soil) interface element behaves elastically if it is under a shear force less than the corresponding skin resistance at that point, and deforms plastically if the shear force exceeds that resistance.

- **Base Resistance F_{max}** - in the unit of force per pile. To simulate a realistic load transfer at the bottom of the pile, the program forces an elastic semi-spherical soil zone of a radius dependent on the base size (see Figure 3.8).

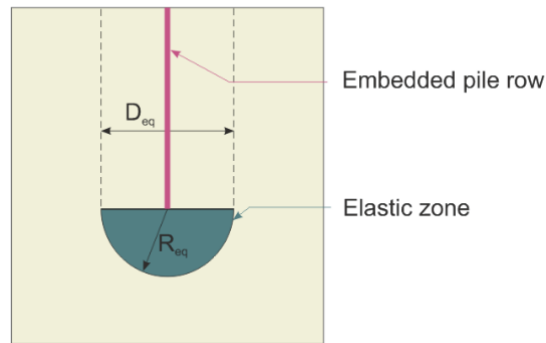


Figure 3.8 – Elastic zone at the bottom of an EBR element in PLAXIS 2D (Plaxis2D, 2019a)

The interaction between the pile and the surrounding soil is governed by the interface elements connecting the pile beam element with the underlying soil mesh (see Figures 3.9 and 3.10). These can be represented by spring elements of varying stiffness. These stiffnesses are calculated as follows:

$$R_s = ISF_{RS} \frac{G_{soil}}{L_{spacing}} \quad (3.4)$$

$$R_N = ISF_{RN} \frac{G_{soil}}{L_{spacing}} \quad (3.5)$$

$$K_f = ISF_{KF} \frac{G_{soil}}{R_{eq} L_{spacing}} \quad (3.6)$$

The interface stiffnesses ISF_{xx} are automatically calculated by PLAXIS 2D as a function of the ratio of the spacing to the diameter $\frac{L_{spacing}}{D}$. These expressions of interface stiffnesses ISF_{xx} can be overwritten by the user to match the load-displacement curve of the pile, as recommended by PLAXIS 2D.

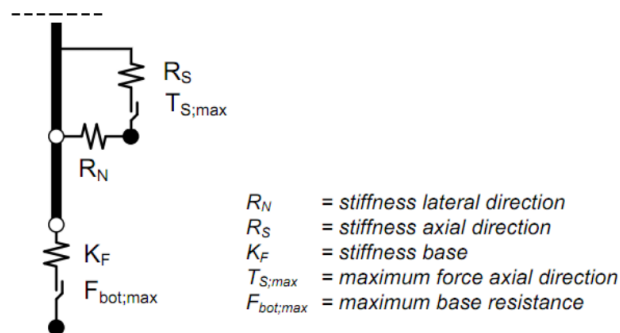


Figure 3.9 – ISFs governing the interaction of the EBR element with the soil mesh (Plaxis2D, 2019a)

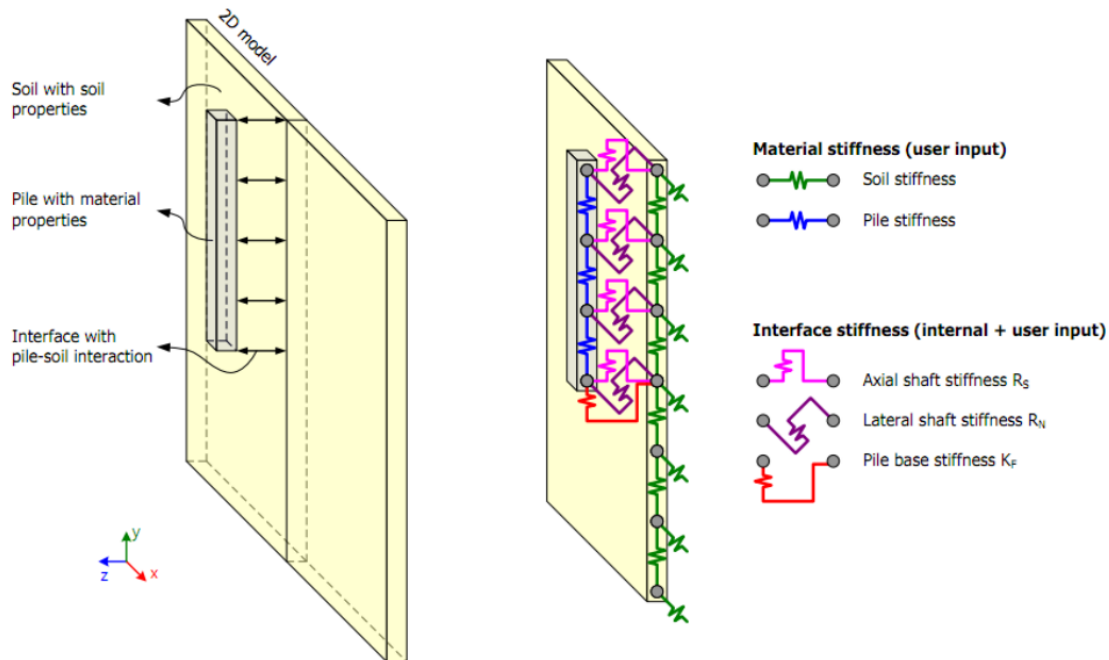


Figure 3.10 – Interface elements governing the axial, lateral, and base interactions of the pile with the soil mesh (Plaxis2D, 2019a)

3.4 Geogrids and Line Contractions

Geogrid elements are line structures that extend in the out-of-plane direction and possess axial stiffness but no flexural stiffness. A geogrid element has two translational degrees of freedom per node (u_x, u_y) and can only undergo tension, not compression. Despite their specific name, geogrid elements are used to represent other forms of geosynthetic reinforcements along with geogrids like geotextiles.

To characterize a geogrid structure in PLAXIS 2D, the user has to mainly specify its normal elastic stiffness i.e. the axial stiffness. If the isotropic option is ticked, as is the case for biaxial geogrids, only one stiffness is required. In the case of an anisotropic geogrid, as is the case with uniaxial geogrids, two stiffness values are entered:

- EA_1 [force per out-of-plane unit width]: The normal elastic stiffness in the in-plane direction
- EA_2 [force per out-of-plane unit width]: The normal elastic stiffness in the out-of-plane direction

The above values are typically found in product manuals under the name ‘axial stiffness J ’ or can be derived from a diagram showing tensile force vs tensile strain. In the case of

uniaxially single-layered reinforced embankments modelled in plane strain, the in-plane stiffness is typically the CMD stiffness and accordingly the highest among the two.

If the geogrid material is set to the elastoplastic option, the following strength parameters would also be required:

- $N_{p,1}$ [force per out-of-plane unit width]: The maximum force in the in-plane direction
- $N_{p,2}$ [force per out-of-plane unit width]: The maximum force in the out-of-plane direction

If the geogrid material is set to the elastoplastic ($N - \epsilon$) option, a strain-dependent strength is specified through a table, as follows with:

- $N_1 - \epsilon_1$: The strain-dependent strength diagram in the in-plane direction
- $N_2 - \epsilon_2$: The strain-dependent strength diagram in the out-of-plane direction

If time dependent geogrid interactions are to be taken into account, i.e. the strength-reduction effect of time (creep), then the visco-elastic (time dependent) model should be chosen. Here, the following stiffness values should be specified:

- $EA_{1,short}$ [force per out-of-plane unit width]: The normal elastic stiffness in the in-plane direction during an instantaneous (initial) strain increment
- $EA_{2,short}$ [force per out-of-plane unit width]: The normal elastic stiffness in the out-of-plane direction during an instantaneous (initial) strain increment
- $EA_{1,long}$ [force per out-of-plane unit width]: The normal elastic stiffness in the in-plane direction during a long term (infinite) strain increment
- $EA_{2,long}$ [force per out-of-plane unit width]: The normal elastic stiffness in the out-of-plane direction during a long term (infinite) strain increment

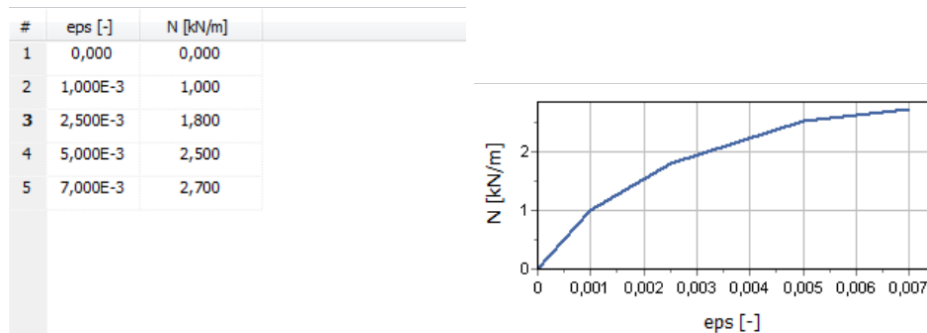


Figure 3.11 – screenshot from PLAXIS 2D showing input table for the $N - \epsilon$ geogrid strength option

- $N_{p,1}$ [force per out-of-plane unit width]: The maximum force in the in-plane direction
- $N_{p,2}$ [force per out-of-plane unit width]: The maximum force in the out-of-plane direction
- Retardation time: the time needed for a linear extrapolation of initial creep to reach the long-term creep level (Figure 3.12). It is derived from a creep test.

In order to track the strain in the geogrid element, the latter has to coincide with a line contraction, a way for PLAXIS 2D to either apply a predetermined contraction to a an element (to simulate heat effects for example), or track the strains in a line element after each construction phase (to track strains developing in a geogrid for example).

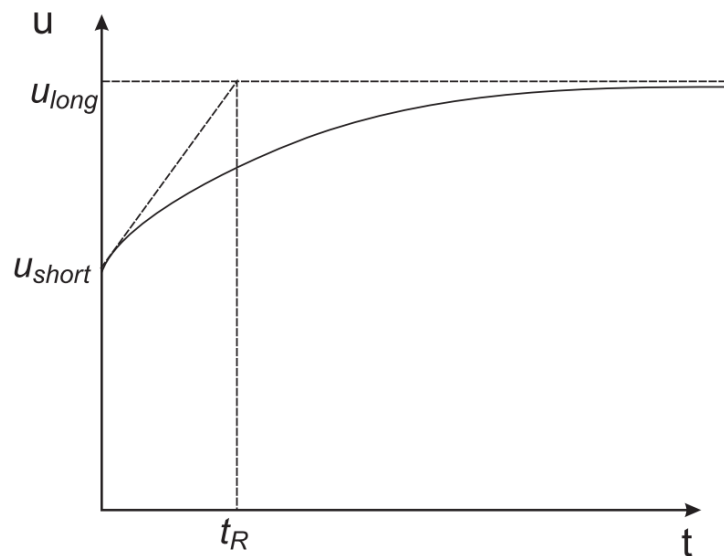


Figure 3.12 – Displacement versus time in a creep test (Plaxis2D, 2019a)

3.5 Summary

This chapter laid out the major features that would be used in modelling a GRPE system in PLAXIS 2D. These included:

- *Model Geometry*: A plane strain model is the most appropriate, as an asymmetric model cannot capture the arching between piles. Eventhough piles don't extend as walls in the out-of-plane direction, they can still be modelled in 2D through the use of Embedded Beam Row elements.
- *Embedded Beam Row elements*: These are line elements superimposed on the existing soil mesh of the 2D model plane with a user-defined out-of-plane spacing. They

interact with the surrounding soil through a set of 'Interface Stiffness Factors' which are automatically calculated by PLAXIS but can be calibrated by the user. Worth noting is that pile capacity (both shaft and toe) is a user input rather than an output for an EBR element.

- *Geogrids and line contractions*: These can be used to model any tensile membrane like geotextiles and geogrids. Their most important properties include the axial stiffness and strain-dependent strength.
- *Soil Model*: This choice determines the stress-strain influence of modelled soils. The Soft Soil model is most likely to be appropriate for modelling soft substratum soils, while both the Hardening Soil and Mohr Columb models could be appropriate for the frictional GRPE embankment. This will be validated in the next chapter.

The next chapters attempts at validating the use of PLAXIS 2D in modelling GRPE systems through a full scale case study. In particular, it focuses on the EBR-soil interaction (through the EBR Interface Stiffness Factors) and the EBR-Geogrid interaction.

Chapter 4

Methods: Case Study for PLAXIS 2D Model Validation

A case study with four test sections was used to validate PLAXIS 2D's ability to model a GRPE system. Validation of PLAXIS 2D has been carried out with pile structures previously (Sluis et al., 2014; Pedersen and Bjorn, 2014; Gunnvard, 2016; Torggler, 2016) but none of these studies tackle a geosynthetically-reinforce system, specifically one that is validated with measurements.

The French national research project, Amélioration des Sols par Inclusions Rigides (ASIRI) was chosen for validation. It is a full-scale experiment of piled embankments on soft soil with test sections that are geosynthetically reinforced. It is documented in detail in Briçon and Simon, 2012 and Nunez et al., 2013.

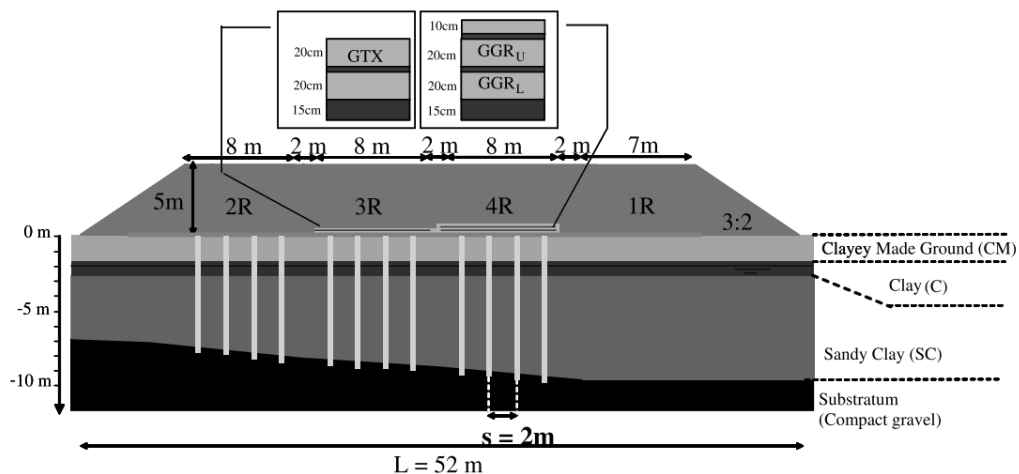


Figure 4.1 – Cross sectional view of the ASIRI test site showing its four test sections (Briçon & Simon, 2012)

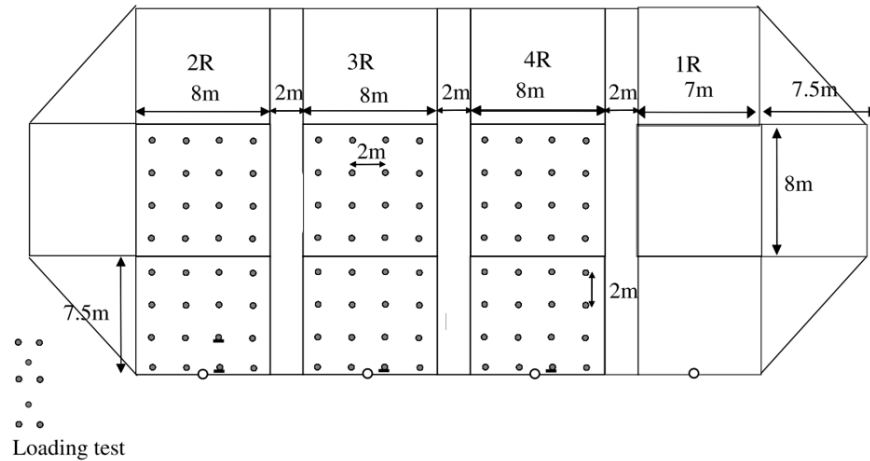


Figure 4.2 – Plane view of the ASIRI test site showing its four test sections, edited from (Briançon & Simon, 2012)

The embankment extends over a 52 m span (out-of-plane), a 23 m width (in-plane), a 5 m height, and a 2:1 side slope (see Figure 4.1). It was divided into 4 instrumented sections (1R, 2R, 3R, and 4R), as seen in Figure 4.2. Sections 2R, 3R, and 4R were supported by a pile grid, while 1R was not piled for reference. Only sections 3R and 4R were basally reinforced, with 3R reinforced with a single geotextile sheet and 4R reinforced with two geogrid layers. Additionally, a set of adjacent test piles were installed for load-displacement, toe capacity, and shaft capacity characterization.

The following instruments were used to measure various stresses, displacements, and strains at the site, and are tracked in PLAXIS 2D for calibration and validation (see Figure 4.3 for a visualization):

- Earth pressure cells (E) to measure the load transfer on pile #3;
- Magnetic probe extensometer in the soft soil (M) to measure the settlement of the soft soil at depths 0 m, -2 m, -5 m, and -8 m;
- Settlement transducers (T) to measure settlement at pile #2 head and subsoil surface at midspan between pile #2 and pile #3;
- Optical fibers (Geodect) to measure strain at and between pile #2 and pile #3

As can be seen in Figure 4.1 above, the subsoil profile is layered from top bottom with a clayey made ground i.e. dry crust layer (CM), a clay layer (C), two sandy clay layers (SC1 and SC2), and a hard substratum of compact gravel (CG).

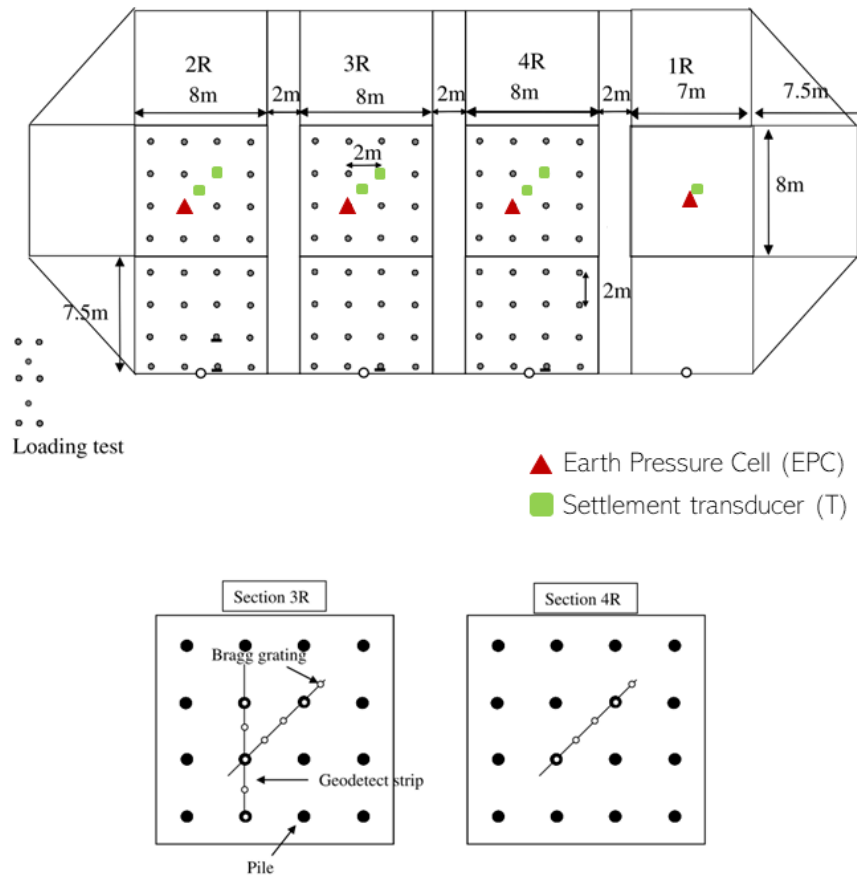


Figure 4.3 – Measurement instrumentation on the ASIRI site, edited from (Briançon & Simon, 2012)

The embankment fill (E) is made of chalky and marley natural soils, and the load transfer platform (LTP) in sections 3R and 4R is made of compact gravel.

Subsoil and embankment fill parameters reported by Briançon and Simon, 2012 and Nunez et al., 2013 can be found in Appendix A.1.

The ASIRI site was chosen for the following reasons:

- The site is characterized in two papers Briançon and Simon, 2012 and Nunez et al., 2013
- Measurements for pile settlement, subsoil settlement, and geogrid strain are documented

- The site includes four test sections (Figure 4.1):
 - Section 1R: non-improved
 - Section 2R: piled
 - Section 3R: piled with 1 geotextile
 - Section 4R: piled with 2 geogrids
- Load-displacement tests were carried out on the used piles to characterize the base and shear resistance of the piles.

4.1 General Model Properties

The site was modelled in the longitudinal direction due to the uniformity of the test sections along the transverse section.

The model size was 75 meters in the horizontal direction to allow for extending the natural subsoil beyond the embankment width, and 30 meters in the vertical direction to allow for extending the substratum downwards.(Figure 4.4)

A 15-node very fine mesh was used. The water table was set at -2 m as reported by Briançon and Simon, 2012.

4.2 Soil Profile Characterization

The Soft Soil (SS) model was chosen for all subsoil layers excluding the substratum, as all these layers had a low stiffness of less than 4 MPa, calculated using their reported initial void ratio e_{init} and compression ratios C_c (2.2 MPa, 1.2 MPa, 3.9 MPa, and 2.8 MPa for the clayey made ground (CM), clay (C), sandy clay (SC1 and SC2) layers respectively). See Appendix A.1 for the list of deduced parameters from reported data.

Input properties are listed in Table 4.1.

The Hardening soil (HS) model was used for the fill, LTP, and substratum due to their relatively high stiffness values (50 MPa, 70 MPa, and 76 MPa respectively). The Mohr-Coulumb model was tested for these soils, but seemed to underestimate displacements in the reference (unimproved) test section 1R most likely due to its insensitivity to increased elasticity with stress.

Input properties for the embankment fill (E), load transfer platform (LTP), and substratum (SS) are listed in Table 4.2 below, all of which are directly taken or derived from reported values in Nunez et al., 2013 and Briançon and Simon, 2012.

All soil types were modelled as *drained* due to the rapid dissipation of water pore water pressure reported by Nunez et al., 2013.

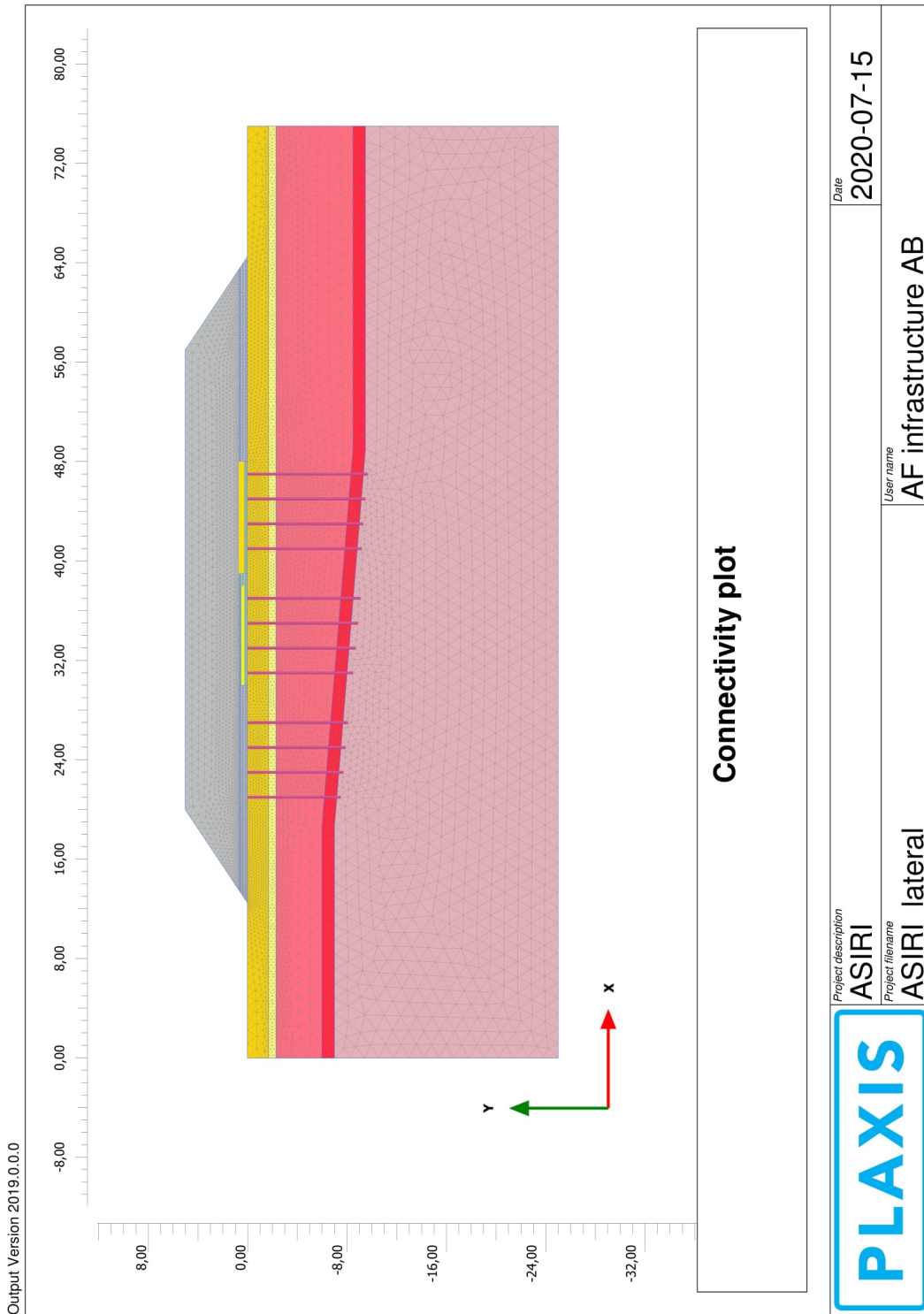


Figure 4.4 – Longitudinal section modelled in PLAXIS 2D

Table 4.1 – Input parameters for the characterization of subsoil layers modelled using the Soft Soil PLAXIS model

	CM	C	SC1	SC2
$\Delta z[m]$	1.7	0.6	3.7	1
$\gamma[kN/m^3]$	20	15	20	20
$e_0[-]$	1	1.7	0.7	0.6
$C_c[-]$	0.2	0.54	0.12	0.14
$C_s[-]$	0,03	0,05	0,01	0,01

4.3 Structures

4.3.1 Embedded Beam Row as Piles

Piles in test sections 2R, 3R, and 4R were drawn as to extend 0,3m into the substratum as reported in Briançon and Simon, 2012, and were given the material properties listed in Table 4.3.

Briançon and Simon, 2012 report that tested piles had a total bearing capacity equal to 600 kN, 61% of which was end bearing and 39% shaft friction. A base resistance F_{max} of 366 kN was thus used. For skin friction, a linear near-constant skin friction was used $T_{skin,start}; T_{skin,end}[kN/m] = [26;30]$, deduced from the reported near-triangular cumulative skin friction values reported. (Figure 4.5)

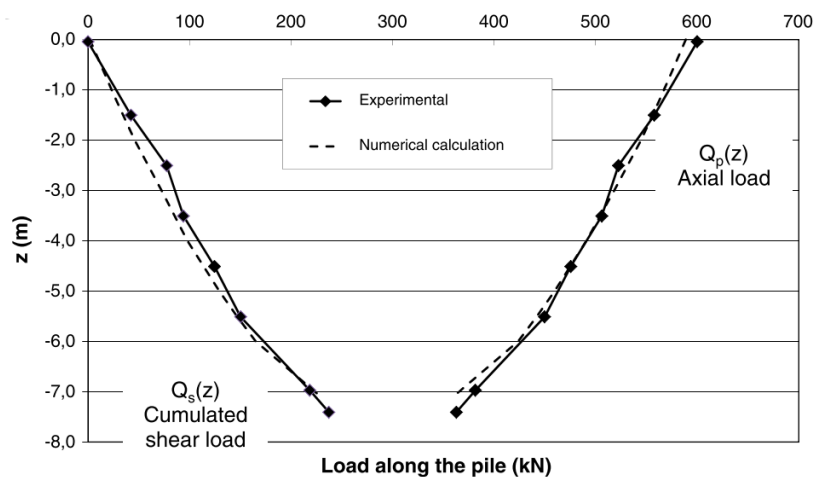


Figure 4.5 – Cumulative shear load reported in Nunez et al., 2013 can be approximated by a constant linear skin resistance

Table 4.2 – Input parameters for the characterization of Embankment (E), Load transfer platform (LTP), and compact gravel substratum (CG)

		E	LTP	CG
	$\gamma[kN/m^3]$	19.1	21	20
	$c'[kPa]$	17.3	61	0
	$\theta'[^{\circ}]$	36.6	36	26
	$\psi[^{\circ}]$	6.6	3	3
	$e_0[-]$	0.3	0.35	0.7
Mohr-Columb	$E'[MPa]$	50	70	76.6
	ν	0,3	0,3	0,3
Hardening Soil	$E_{oed}[MPa]$	67.3	94	103.1
	$E_{50}[MPa]$	67.3	94	103.1
	$E_{ur}[MPa]$	201.9	282.7	309.3
	$m[-]$	0.5	0.5	0.5

The EBR connection type is set to the pile bottom to avoid an unrealistic *adhesion* between the pile top and surrounding soil at the pile head, and thus allow soil sliding at the pile top. The bottom connection was set to *fixed* given the embedded nature of the piles, having been driven 30 cm into hard substratum.

Interface Stiffness Factors (ISFs) of the EBR element (axial, lateral, and base) can be set to *default*, allowing PLAXIS 2D to automatically calculate them as a function of the user-defined pile free distance $L_{spacing}$ and diameter as stated previously in Equations 3.5, 3.4, and 3.6. They can also be overruled by the user to match load-displacement measurements.

The main goal of this section is to thus validate the accuracy of these default values, and the practicality of using load-displacement curves to overrule their default values.

First, to understand the general effect of the three ISFs on pile-soil settlement, test section 2R (piles, no GR) is considered and its piles' ISFs (ISF_{axial} , $ISF_{lateral}$, ISF_{base}) are varied individually to understand their individual effect on the soil/pile settlement. The method is detailed out in section 4.5 below.

Then, the full case study model is used, calibrating each of the test section piles to the load-displacement curve (LDC) of test piles adjacent to the embankment, the measured load-displacement (MLD) at monitored piles in test sections 2R, 3R, and 4R, and the measured soil-pile differential settlement (MDS) of monitored piles in test sections 2R, 3R, and 4R. This is expanded upon in Section 4.6 below.

Table 4.3 – Input parameters for the EBR element representing the piles

	Material type	Elastic
	E [GPa]	20
	γ [kN/m ³]	23
	Beam type	predefined
	Predefined beam type	Massive circular beam
	Diameter [m]	0.38
	$L_{spacing}$ [m]	2
	Base resistance F_{max} [kN]	366
Linear skin resistance	$T_{skin,start,max}$ [kN/m]	26
	$T_{skin,end,max}$ [kN/m]	30
Interface Stiffness Factors (ISF)	ISF_{R_s}	default=0.7; calibrated to LDC*, MLD [†] , MDS [‡]
	ISF_{R_n}	default=0.7; calibrated to LDC, MLD, MDS
	ISF_{K_f}	range = default=7; calibrated to LDC, MLD, MDS

* LDC: Load displacement curve of test piles reported by Briançon and Simon, 2012, found in Figure 4.7 below

[†] MLD: Measured load displacement of monitored piles following embankment construction as reported by Briançon and Simon, 2012 and Nunez et al., 2013.

[‡] MDS: Measured soil-pile differential settlement at monitored piles as reported by Briançon and Simon, 2012

4.3.2 Geosynthetic Reinforcement using Geogrids

The geotextile in test section 3R and geogrids in test section 4R are both modelled using a geogrid element, with parameters listed in Table 4.4. Original manufacturer values were reported by Briançon and Simon, 2012 and Nunez et al., 2013 at various strain levels. The isotropic option is chosen given the geotextile is biaxial.

Table 4.4 – Input parameters to the geogrid element representing the geotextile in 3R and geogrids in 4R

	Geotextile (3R)	Geogrid (4R)
Material type	Elastoplastic N- ϵ	Elastoplastic N- ϵ
Isotropic	Yes	Yes
EA_1 [kN/m]	750	520
$N(2\%)$ [kN/m]	16	10
$N(3\%)$ [kN/m]	22	13
$N(5\%)$ [kN/m]	37	17

4.4 Staged Construction

The model is run with the following stages:

1. **Initial phase** determining the initial in-situ stresses based on the reported pre-overburden pressure (POP) of 30 MPa.
2. **Pile Activation** where the embedded beam row elements are activated.
3. **LTP Construction** where LTP fill and associated geogrid elements are activated in test sections 3R and 4R, and embankment fill of the same height is activated in sections 1R and 2R.
4. **Embankment Construction** where the remainder of the embankment is activated.

4.5 Understanding the Effect of Interface Stiffness Factors

To better understand the effect of stiffness factors on the pile and soil settlement, the axial, lateral, and base stiffness factors are varied from their default values of $ISF_a = 0.7$, $ISF_l = 0.7$, and $ISF_b = 7$, and the resulting pile and soil settlement compared. This is done to a transverse cross section of test section 2R (Figure 4.6).

Accordingly, ISFs were varied from 1/10 to 10 times their default value, and the resulting pile and soil settlement tracked:

- $ISF_a = [0.07; 0.35; 0.7(\text{default}); 2.1; 7; 70]$
- $ISF_l: [0.07; 0.35; 0.7(\text{default}); 2.1; 7; 70]$
- $ISF_b: [0.7; 3.5; 7(\text{default}); 21; 70; 210]$

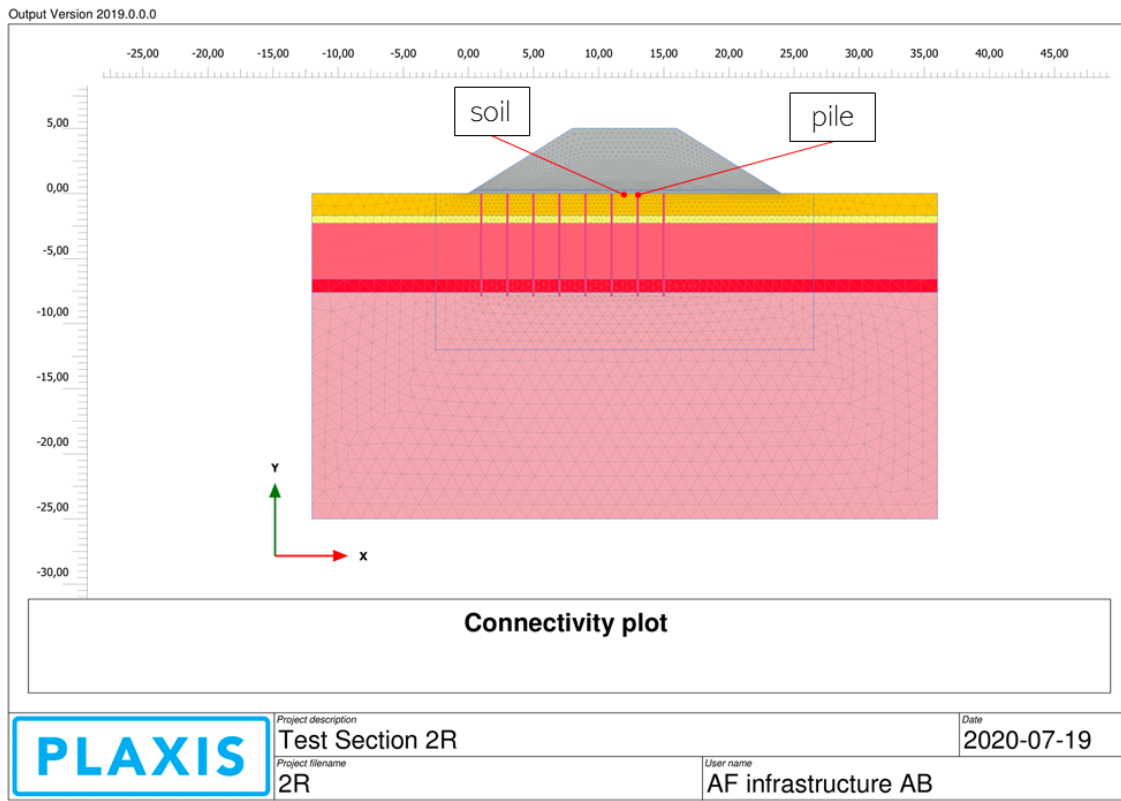


Figure 4.6 – Transverse section of test section 2R used to understand the effect of ISFs on soil and pile settlement

4.6 Model Variants: Calibration of Interface Stiffness Factors

PLAXIS 2D has built-in functions to calculate the interface stiffness factors of the embedded beam row elements (Equations 3.5, 3.4, and 3.6), but allows the user to calibrate ISFs by fitting the model to various measurements.

4.6.1 Calibration to Load-Displacement Curve (LDC)

Static load testing was performed adjacent to the ASIRI embankment for a test pile with $L=7.44$ m, and force-displacement results of the pile toe are reported. (Figure 4.7).

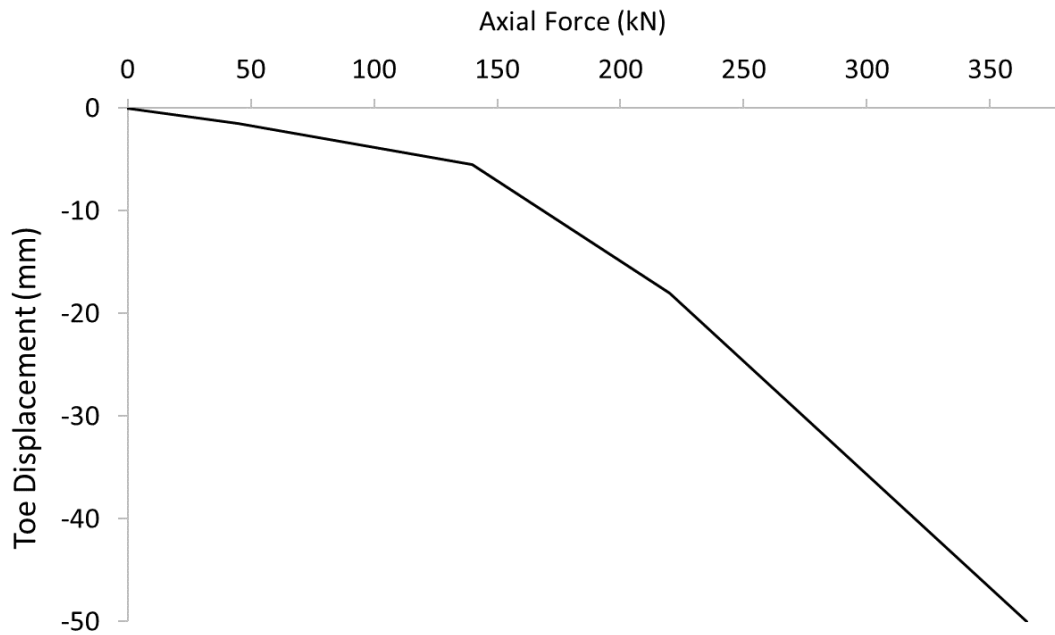


Figure 4.7 – Load-displacement curve reported by Nunez et al., 2013 and Briançon and Simon, 2012 following a static load test of an embedded pile at the ASIRI site

Base stiffness factor ISF_b was calibrated for each test section pile group (2R, 3R, and 4R) until the output load-displacement of the second pile of each pile group (see Figure 5.8 below) matches the reported load-displacement curve.

After ISF_b of each of pile group has been calibrated to fit the LDC, the resulting pile and soil settlement are compared with measurements.

4.6.2 Calibration to Measured Load-Displacement (MLD)

To test whether the discrepancies between measurements and the LDC-calibrated model are due to the natural deviation of pile behavior from test pile behavior, the model's ISF_a ISF_b values are recalibrated to match the reported load-displacement measurements of monitored piles in each of sections 2R, 3R, and 4R. (Figure 5.8).

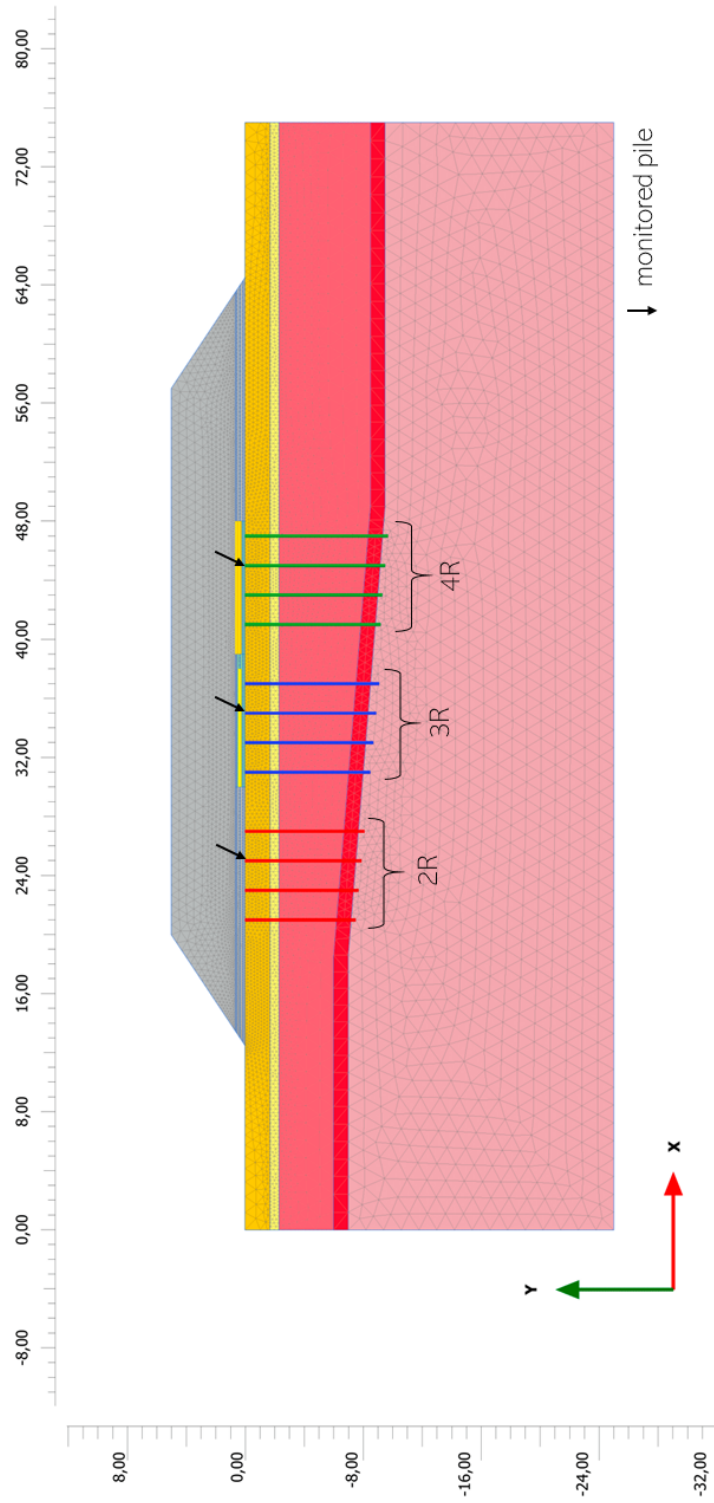


Figure 4.8 – ISF_b of monitored piles is adjusted for each pile group to match pile-displacement curve

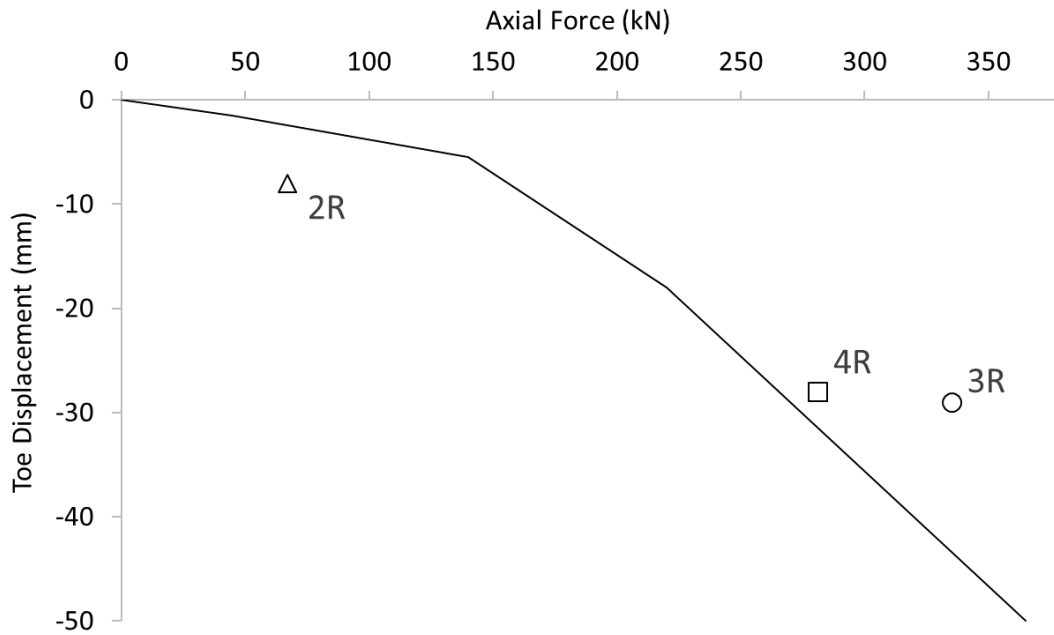


Figure 4.9 – Load-displacement state of monitored piles in test sections 2R, 3R, and 4R plotted along the load-displacement curve of the test pile

4.6.3 Calibration to Measured Differential Settlement (MSD)

Given the strong dependency of predicted geogrid strain on soil-pile differential settlement at the pile head, the model's ISF_b were calibrated as to match reported soil-pile differential settlement in each of test sections 2R, 3R, and 4R.

Reported values of differential settlement at the monitored piles are listed in Table 4.5 below from Briançon and Simon, 2012

Table 4.5 – Measured soil and pile settlement in sections 2R, 3R, and 4R as reported by Nunez et al., 2013 and Briançon and Simon, 2012

Test Section	vertical settlement (mm)		
	soil	pile	soil-pile differential
2R	105	8	97
3R	70	29	41
4R	65	28	37

Load-displacement curves do not give any information about the differential soil-pile settlement, so the main objective of this calibration is to assess the usefulness of collecting soil settlement data in the vicinity of test piles, particularly for the goal of predicting maximum strains overlaying geogrids.

It was also determined that reaching a certain differential settlement using ISF_b calibration or ISF_a and ISF_b results in the same geogrid strain distribution. Accordingly, this calibration section is carried out by varying ISF_b only.

Chapter 5

Results and Discussion

5.1 Effect of Interface Stiffness Factors

Pile, soil, and pile-soil differential settlement in Section 2R are tracked after varying ISF_a , ISF_b , and ISF_l separately (see Figures 5.1, 5.3, and 5.2).

As seen in Figure 5.1 above, increasing ISF_a from 0.07 to 70 results in a slight increase of pile settlement (20% increase from 28 mm to 33 mm and a more noticeable decrease in the surrounding soil settlement (144 mm to 109 mm). This results in a trend of decreasing differential soil-pile settlement as axial stiffness increases, with the latter approaching an asymptotic value as ISF_a increases.

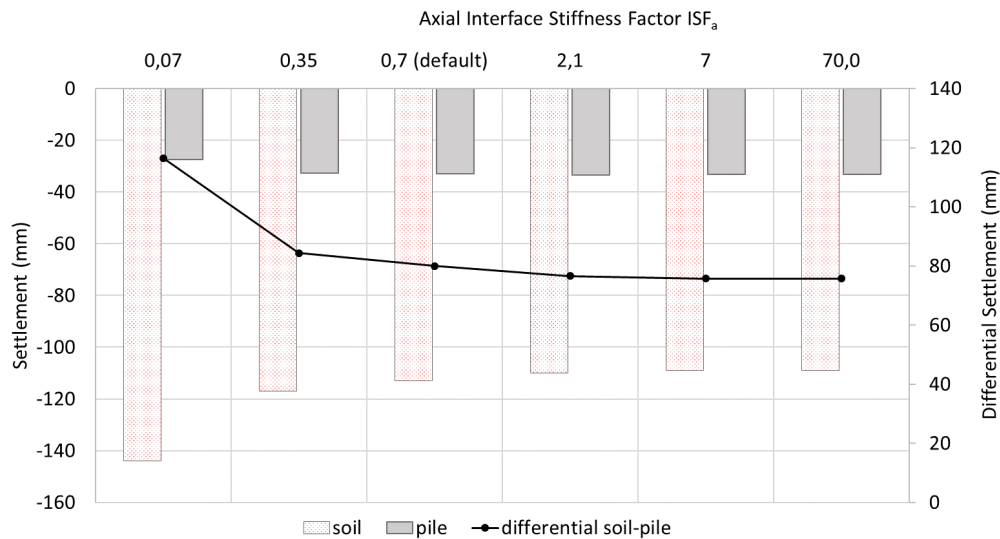


Figure 5.1 – Effect of varying ISF_a on soil and pile settlement

A similar trend is noted in changing ISF_b stiffness. As seen in Figure 5.3, increasing the

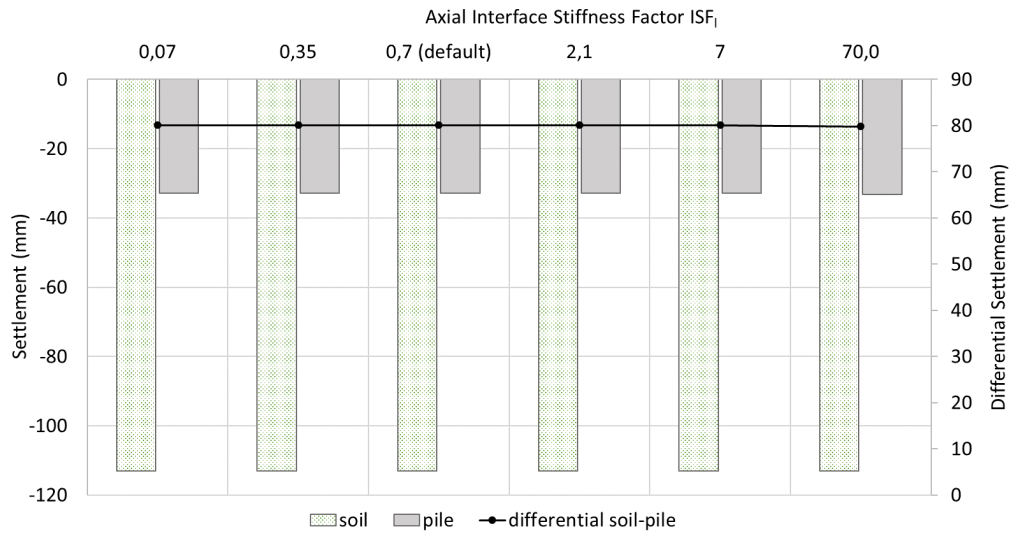


Figure 5.2 – Effect of varying ISF_l on soil and pile settlement

latter from 0.7 to 210 results in an increase of pile settlement (from 24 mm to 41 mm) and a decrease in the surrounding soil settlement (165 mm to 78 mm). This translates to a decrease in differential soil-pile settlement as ISF_b increases.

For lateral stiffness, however, changing ISF_l results in negligible change in soil, pile and accordingly soil-pile differential settlement. As seen in Figure 5.2 below, increasing ISF_l from 0.07 to 70 results in no noticeable change in pile or soil settlement.

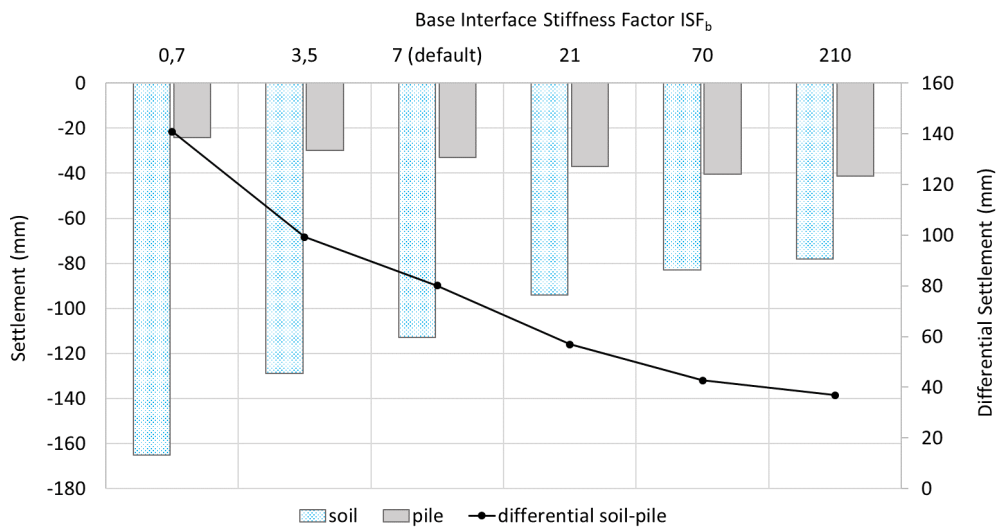


Figure 5.3 – Effect of varying ISF_b on soil and pile settlement

Figure 5.4 summarizes the effect of the various ISFs on percent change of differential settlement from their default values. It shows several main trends.

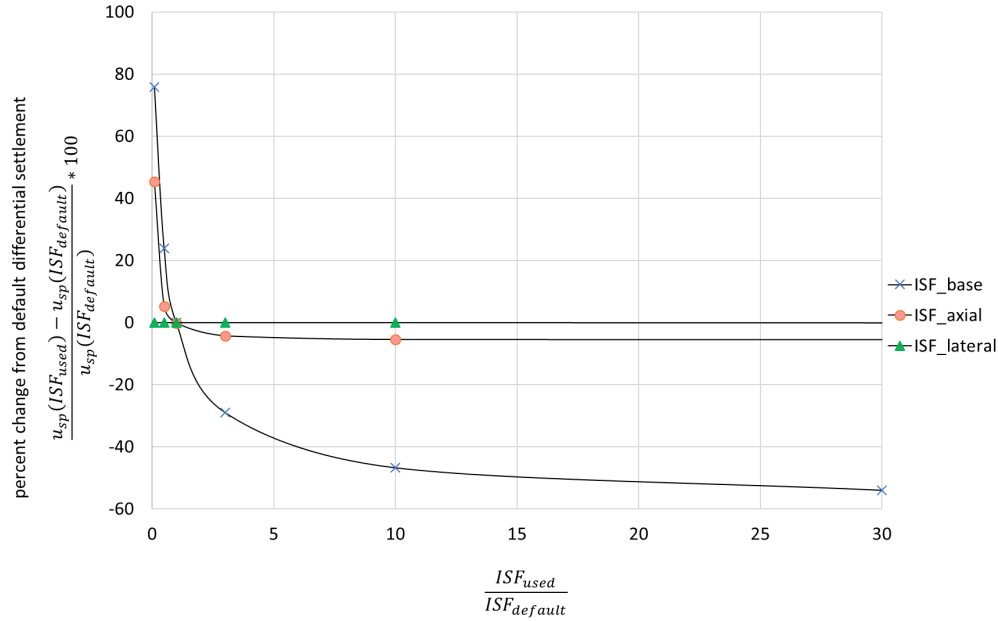


Figure 5.4 – Percent change in differential settlement as a function of ISF value used

First, both ISF_a and ISF_b allow the user to calibrate the settlement behavior at the pile-soil interface, yet the effect of ISF_b is more pronounced and thus allows for a wider range of calibration.

Second, in the ASIRI case, pile settlement is predominantly governed by toe movement, with base resistance constituting 61% of the pile's capacity. This might explain the stronger effect of ISF_b on pile-soil interface settlement behavior compared to ISF_a . The negligible effect of the lateral ISF_l is likely due to the axial nature of loading of the pile, so its lateral stiffness has negligible effect on the vertical settlement of the pile and surrounding soil.

This can be more clearly seen in the constitutive equation of pile skin (Equations 5.1): Below user-input capacities for base resistance (F_{max}) and axial resistance ($T_{skin,start,max}; T_{skin,start,max}$), the interface behaves elastically with ISF-dependent stiffnesses (Equations 5.1 below):

$$\begin{bmatrix} \sigma_a \\ \sigma_l \\ \sigma_b \end{bmatrix} = \begin{bmatrix} K_a & 0 & 0 \\ 0 & K_l & 0 \\ 0 & 0 & K_b \end{bmatrix} \begin{bmatrix} u_a^s - u_a^p \\ u_l^s - u_l^p \\ u_b^s - u_b^p \end{bmatrix} \quad (5.1)$$

where $K_a = ISF_a \frac{G_{soil}}{L_{spacing}}$; $K_l = ISF_l \frac{G_{soil}}{L_{spacing}}$; and $K_b = ISF_b \frac{Req G_{soil}}{L_{spacing}}$.

5.2 Calibration to Load-Displacement Curve (LDC)

ISF_b was calibrated for each test section pile group (2R, 3R, and 4R) as to match the load-displacement curve of test piles adjacent to the ASIRI embankment.

5.2.1 Results

Figure 5.5 shows the load displacement state using the default PLAXIS ISF_b (green) and those after ISF_b calibration to match the load displacement curve (black). It also shows the ratio of calibrated ISF_b to the default value, i.e. how much ISF_b had to be increased to match the load-displacement curve. ISF_b was increased from its default value of 7.0 to 57 for test section 2R, 12 for test section 3R, and 23 for test section 4R. (Table 5.1).

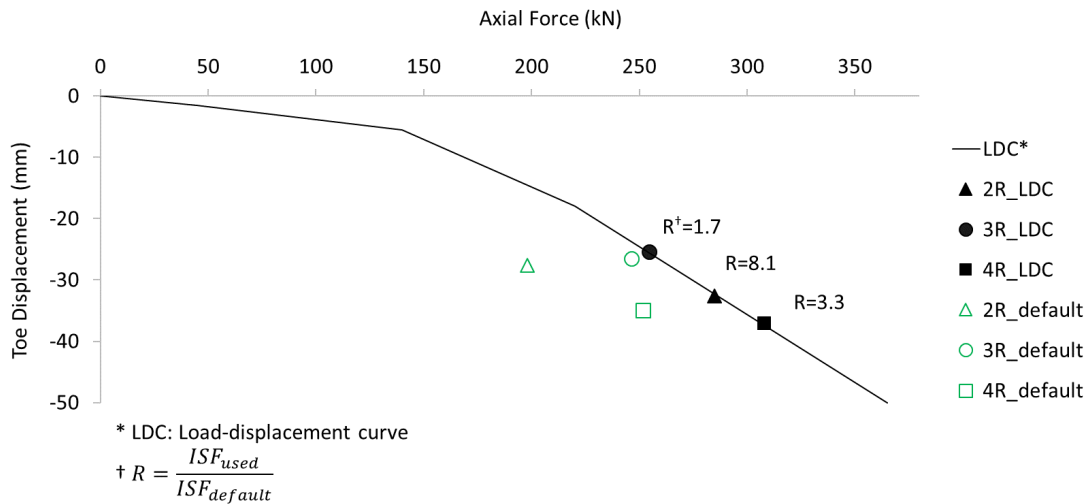


Figure 5.5 – calibration of ISF_b of pile groups 2R, 3R, and 4R from their default values to match the load-displacement curve (LDC)

Table 5.1 – ISF values at their default and LDC-calibrated values

	Default ISF_b	calibrated ISF_b
2R	7	57
3R	7	12
4R	7	23

Figure 5.6 shows the resulting settlement profile for both the default and LDC-calibrated models, compared to measured pile and soil settlement reported.

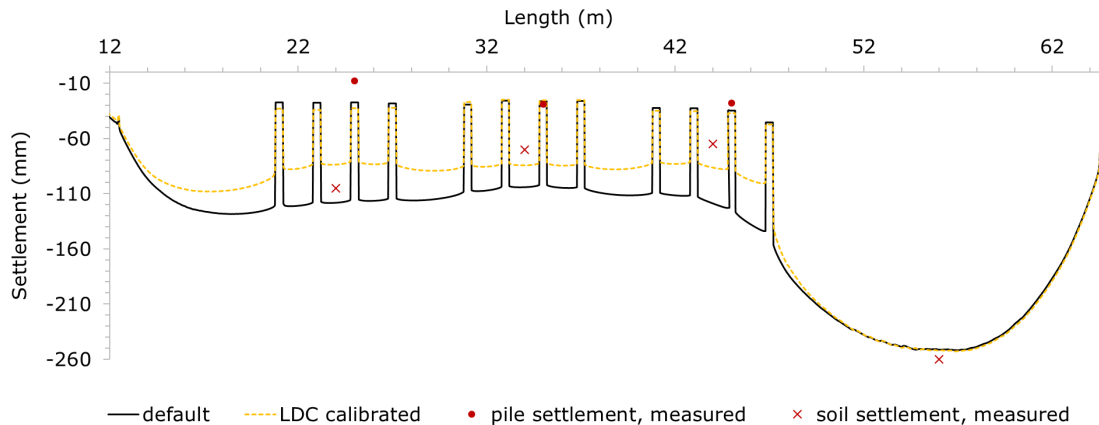


Figure 5.6 – Settlement profile under default and calibrated ISF_b , compared to measured values

5.2.2 Discussion

For pile settlement, the calibration minimally affects the predicted settlements. As previously shown in Figures 5.1 and 5.3, ISF_b has a minimal effect on pile settlement. These results are thus in agreement with expectations.

For soil settlement, the LDC- calibrated model gives better soil settlement predictions in test sections 3R and 4R compared to the default model, but not necessarily for 2R. Accordingly, the LDC-based calibration was insufficient to fully optimize ISF_b .

It is not clear yet why the calibration gave better settlement results for sections 3R and 4R but not 2R. This might be due to a natural variation between the settlement behavior of the test pile, used to produce the load-displacement curve, and that of the embankment piles. In other words, optimizing ISF_b for the test piles' load-displacement inherently assumes that the test piles behave identically to those used under the embankment.

In fact, data reported by Briançon and Simon, 2012 shows a spread in the load-settlement behavior of embankment piles around the load-displacement curve.

Figure 4.9 shows, the monitored piles in each of the sections 2R, 3R, and 4R do not fall on the load-displacement curve from the static load test. The discrepancy between the model predictions and reported data for these monitored piles might thus be the result of the assumption that the pile behavior matches that of the test piles. Accordingly, the model ISF_a and ISF_b were calibrated to match measured load-displacement (MLD) state of the monitored piles.

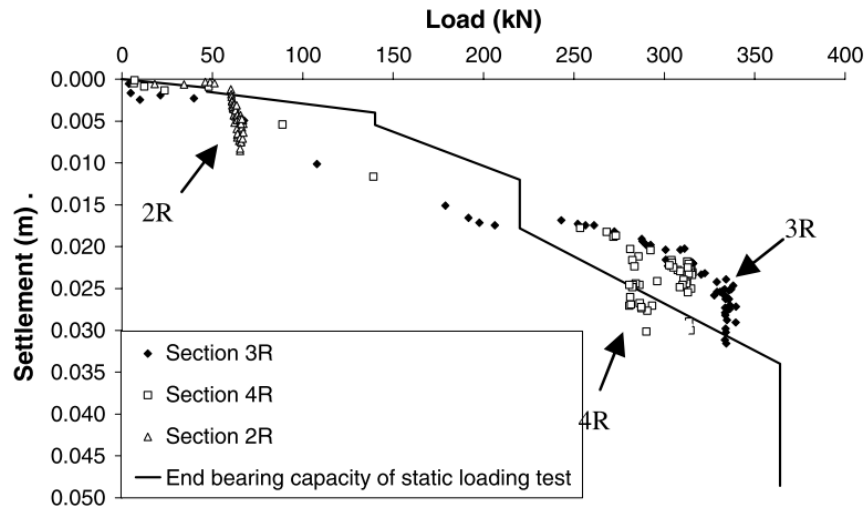


Figure 5.7 – load-displacement state of monitored piles plotted over the reported load-displacement curve (Briançon & Simon, 2012)

5.3 Calibration to Measured Load-Displacement (MLD)

ISF_a and ISF_b of monitored piles are calibrated to match the reported load-displacement data of the monitored piles, listed in Table 5.2.

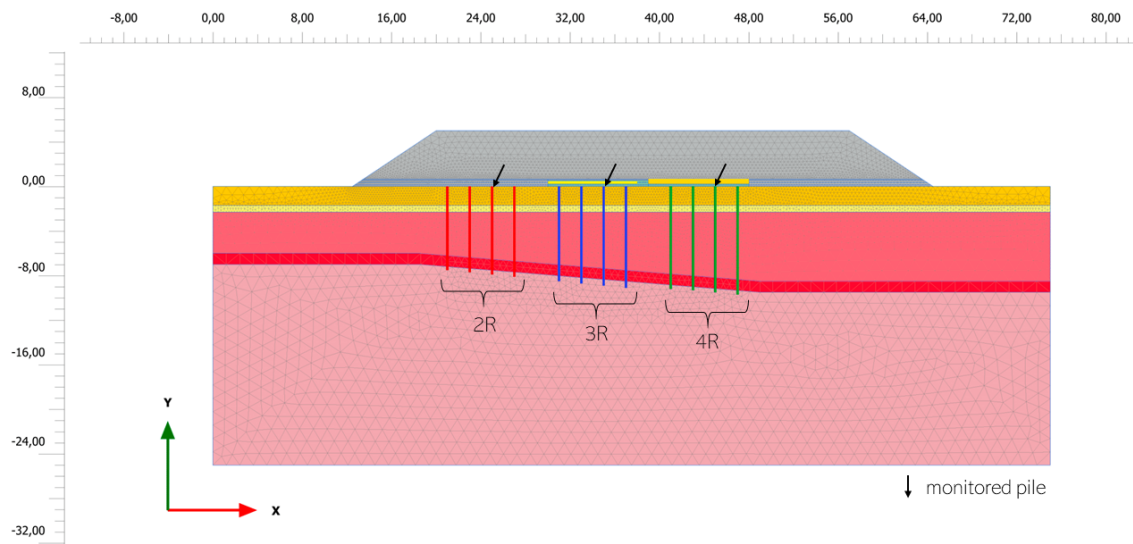


Figure 5.8 – Monitored piles in the ASIRI site pointed out on the PLAXIS 2D model

Table 5.2 – Measured load and displacement values at the monitored piles as reported by Briançon and Simon, 2012 and Nunez et al., 2013

	pressure* [kPa]	load [†] [kN]	displacement [‡] [mm]
2R	589	67	8
3R	2958	335	29
4R	2479	281	28

* as reported in Briançon and Simon, 2012 as the long term value of pressure at the monitored pile head

[†] load at pile head as calculated by multiplying the reported pile head pressure by the pile head area

[‡] reported in Briançon and Simon, 2012 as the long term subsoil settlement midway between the monitored pile and its diagonal pile

5.3.1 Results

Resulting calibrated ISF_a and ISF_b values are listed in Table 5.3 below.

Resulting vertical displacement profile is plotted in Figure 5.9.

As is expected from the calibration process, predicted pile settlement is matched with the measured one.

Soil settlement is however vastly overestimated in all sections: Section 2R features a soil settlement percent difference of 94%, 3R of 17%, and 4R of 126% compared to reported measurements.

Table 5.3 – ISF values under their default, LDC-, and MDC-calibrated models

	ISF_a			ISF_b		
	Default	LDC	MLD	Default	LDC	MLD
2R	0.7	0.7	0.001	7	57	1.0
3R	0.7	0.7	0.7	7	12	21.0
4R	0.7	0.7	0.01	7	23	17.5

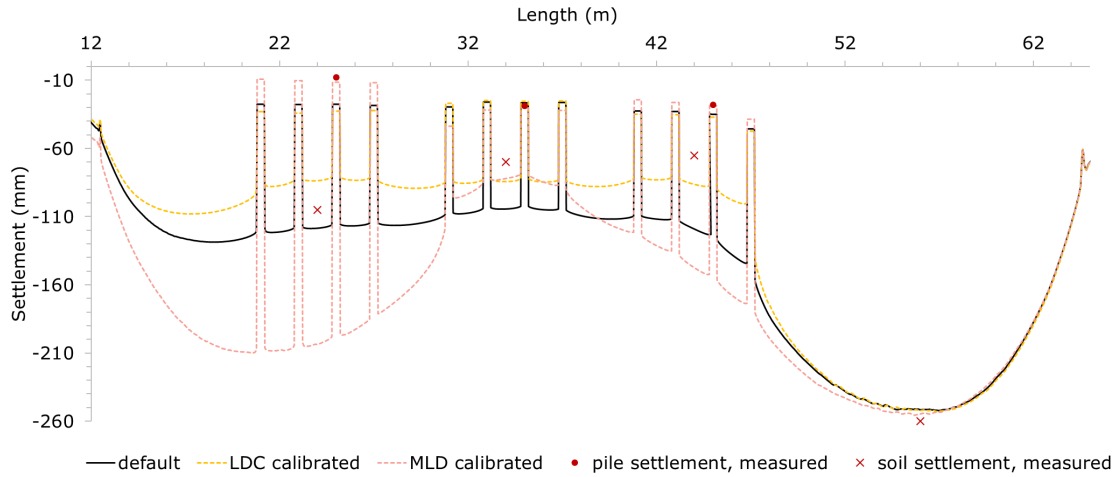


Figure 5.9 – Settlement profile under default, LDC-calibrated, and MLD-calibrated ISF values, compared to measured settlement

5.3.2 Discussion: Calibration to LDC vs. MLD

Results of Section 5.2 showed that the LDC-calibrated model gave more accurate results for soil settlement compared to the default model, but was still off by 20% - 30%.

To rule out the possibility that this discrepancy was due to deviation from test pile behavior, ISFs were calibrated to match measured load displacement of monitored piles. Results showed a vast overestimation of soil settlement, notably in sections 2R and 4R.

This is in accordance with the effect of ISF_a noted in Figure 5.1, where decreasing ISF_a results in an increase in soil-pile differential settlement, the increase being much sharper at lower values.

To match the low pile load of 67 kN in 2R, the pile's ISF_a had to be considerably lowered from its default 0.7 to 0.001 ($R=700$), thus resulting in excessive differential settlement between the pile and soil. The same effect took place in section 4R, where ISF_a had to be lowered to 0.01 ($R=70$). In section 3R, however, the pile's load could be matched without lowering ISF_a , which might explain why no excessive soil settlement is noted in section 3R.

5.4 Conclusions and Recommendations for ISF Calibration

Three set of values for ISF_a and ISF_b were used to model the ASIRI GRPE test site:

- **Default** values determined automatically by PLAXIS 2D using the EBR diameter and out-of-plane spacing.

- **Load-displacement curve - calibrated** values; this was achieved by varying the base stiffness factor ISF_b .
- **Measured load-displacement - calibrated** values; this was achieved by varying simultaneously the axial and base stiffness factors ISF_a and ISF_b .

PLAXIS 2D suggests calibrating EBR ISFs to the load-displacement characteristics of the piles. (Sluis et al., 2014), but this Chapter's analysis presents two main limitations of such an approach:

- The natural scatter of measured load-displacement of monitored piles shows a divergence from the expected (LDC) behavior. This can result in vast ranges of possible ISF_b and ISF_a between matching the actual and predicted behavior of piles. For example, ISF_a of test section 2R was decreased by a factor of 700 to match the load-displacement state of the monitored pile.
- ISF values have a more pronounced effect on soil settlement than on pile settlement, as shown in Section 5.1. However, information about differential soil settlement is not captured by load-displacement curves, and is thus not taken into account when calibrating ISF values. In other words, calibrating ISF values is a process of optimizing soil settlement, pile settlement, and pile load, and calibration to only two of those may result in a vast divergence of the third, as shown in results of Section 5.3 where soil settlement was vastly overestimated to match the pile load.
- The model behavior could be fit to the load-displacement curve by changing ISF_b solely while keeping ISF_a and ISF_l unchanged. This is limiting because it allows the user to LDC-optimize the model when two of the three ISFs remain uncalibrated.

It is worth noting that data on shear resistance distribution of the test pile (in Figure 4.5) aided in converging the calibration process.

Figure 5.10 below shows how the predicted settlement profile would have varied (at default ISF values) using a layer-dependent shaft resistance with varying Interface Reduction values $R_{inter} = 0.4, 0.7,$ and 1.0 instead of the linearly varying shaft resistance reported by (Nunez et al., 2013).

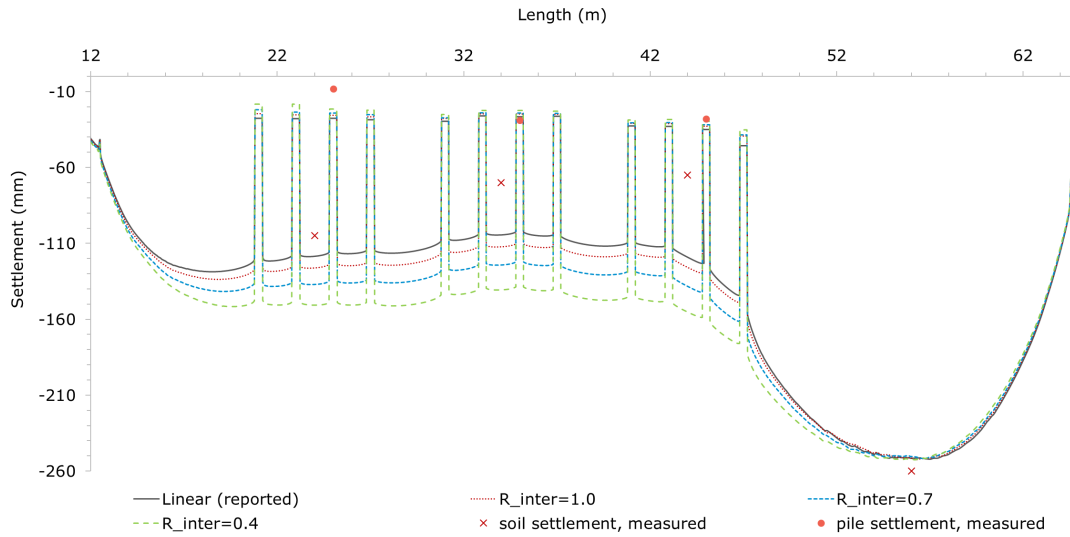


Figure 5.10 – Settlement profile (using default ISF values) under various shaft capacity distributions

EBR calibration could thus be enhanced value by collecting measurements on:

- Distribution of shaft resistance along the pile shaft
- Soil settlement in the vicinity of the pile instead of solely depending on pile settlement through the pile-displacement curve.

The next chapter will explore the effect of these different calibration methods on the accuracy of predicting geogrid strain.

Chapter 6

Geogrid Strain: Numerical and Analytical Validation

This chapter focuses on the accuracy of geogrid strain prediction in PLAXIS 2D and analytical design guidelines. In particular, it attempts at answering the following questions:

- Given the excessive soil settlement noted in Chapter 5 as a result of EBR calibration to measured load-displacement, to what extent will geogrid strain be overestimated?
- Can calibration to differential soil-pile settlement instead of pile load-displacement give a more accurate prediction of geogrid strain?
- How do the Dutch and German codes perform in predicting geogrid deformation and maximum strain?

6.1 Plaxis 2D Output

6.1.1 Methods

PLAXIS 2D output for geogrid strain in the single geotextile layer of 3R and the double geogrid layer of 4R is assessed under the following ISF values:

- PLAXIS 2D default
- Calibrated to load-displacement curve
- Calibrated to load-displacement of monitored piles
- Calibrated to differential soil-pile settlement.

Geogrid strain values reported by Briancon and Simon, 2012 and Nunez et al., 2013 were measured just outside the pile head and between piles as seen in Figure 6.1.

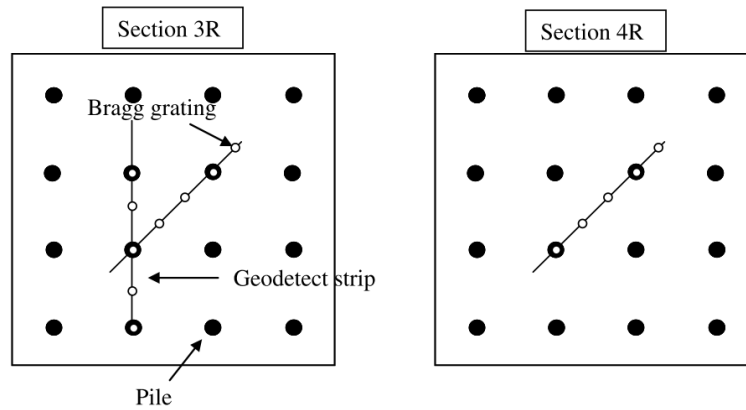


Figure 6.1 – Locations of geogrid strain gauges in test sections 3R and 4R, as reported in Briançon and Simon, 2012

6.1.2 Results

For section 3R, the PLAXIS 2D models seems to replicate the expected distribution of strain: Maximum strain is located at the outskirts of the pile. In regards to the magnitude of maximum strain, all models underestimate the maximum strain, with the MLD curve giving the best estimate.

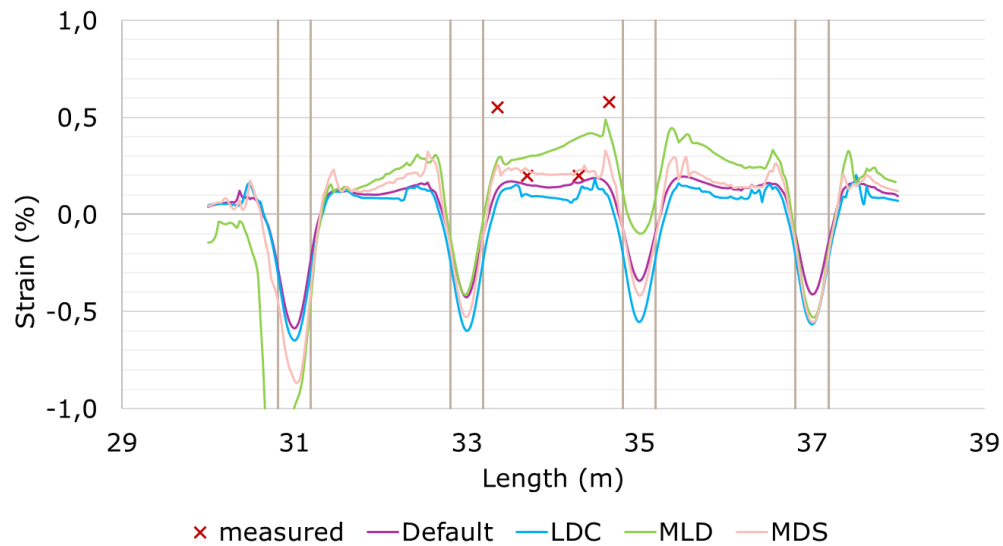


Figure 6.2 – PLAXIS 2D strain profile under various ISF-calibrated values, compared to measured strain for test section 3R

We notice that the order of models with respect to predicted maximum strain matches their order with respect to differential soil-pile settlement: highest differential pile-soil settlement results in the highest strain (lowest error compared to measurement), as can be seen in Figure 6.11 below, thus possibly explaining why the MLD model resulted in the most accurate prediction.

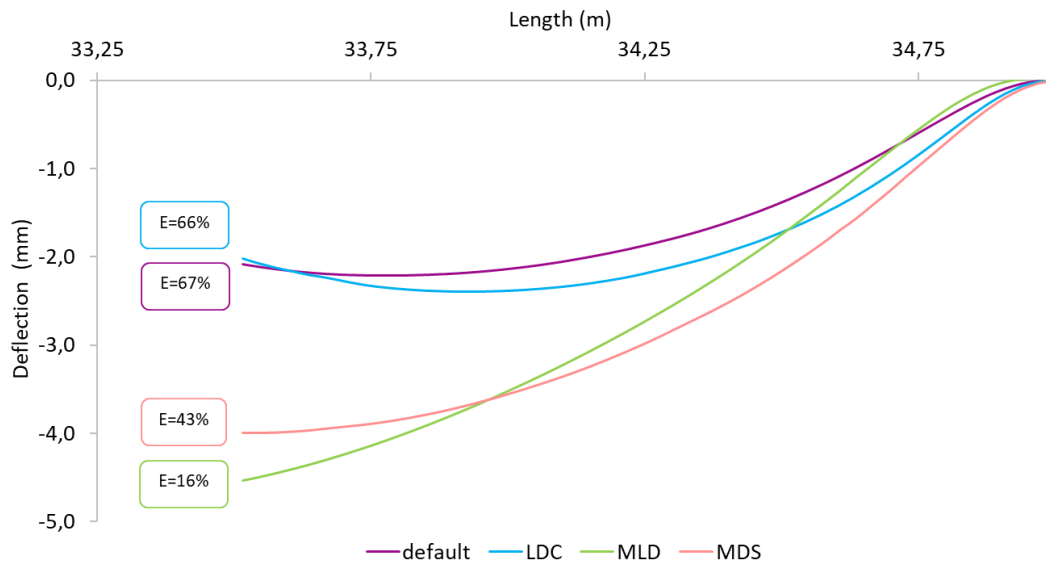


Figure 6.3 – Higher errors of predicted to measured maximum strain is in models with less GR deflection, and vice versa

For section 4R, the same trend of underestimating maximum strain is also noted in both the upper and lower geogrids.

6.1.3 Discussion

A major limitation of modelling geogrids over embedded beam rows is PLAXIS 2D is the nature of EBR elements: they are superimposed over the soil mesh and thus do not "break through" the soil mesh. Upon settlement, the mesh is allowed to settle *through* the pile element. This significantly decreases the deflection of the geogrid element and thus the strain developed.

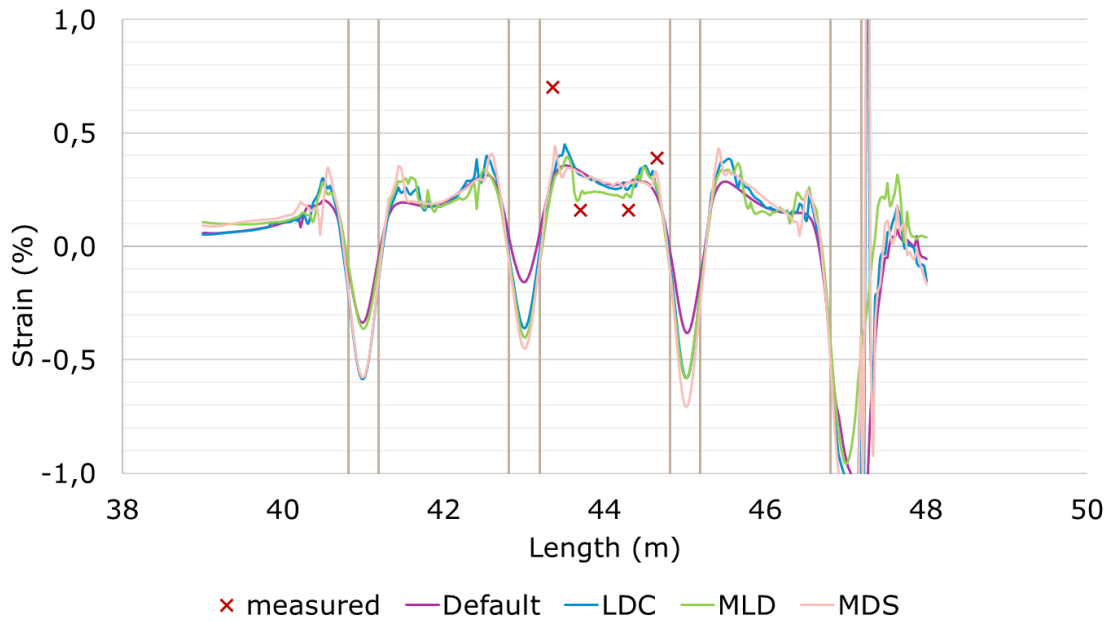


Figure 6.4 – PLAXIS 2D strain profile under various ISF-calibrated values, compared to measured strain for the bottom geogrid in test section 4R

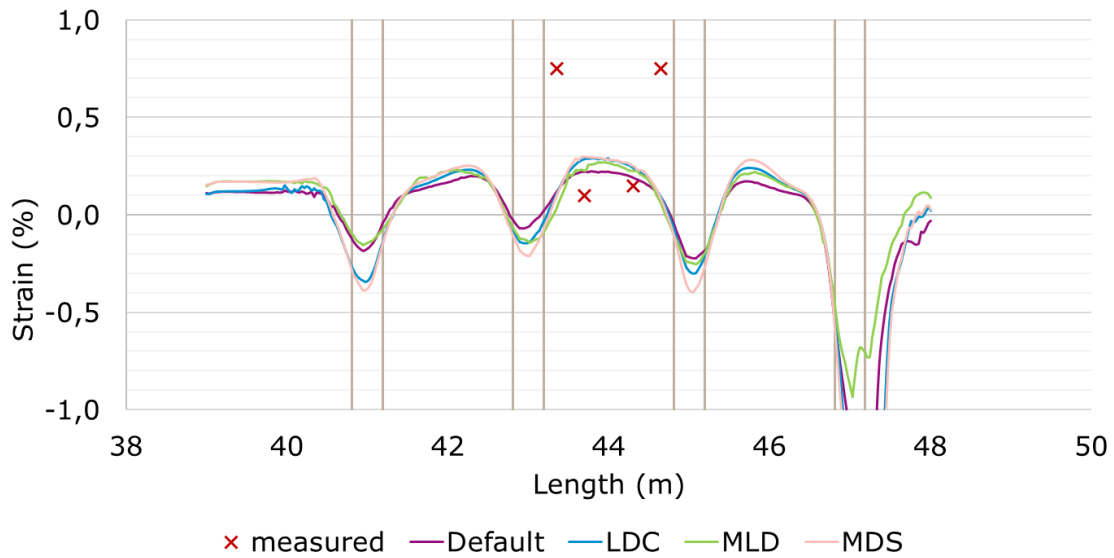


Figure 6.5 – PLAXIS 2D strain profile under various ISF-calibrated values, compared to measured strain for the top geogrid in test section 4R

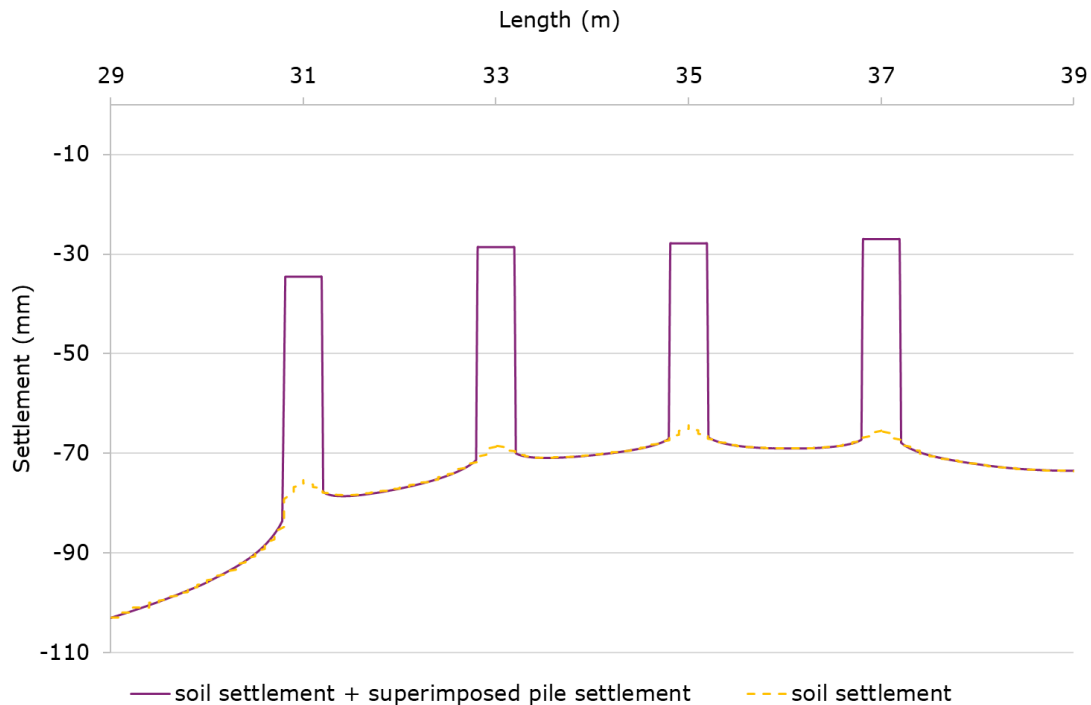


Figure 6.6 – settlement soil mesh profile before (yellow, dashed) and after (purple, full) pile superimposition

This can be seen more clearly in Figure 6.6. The dashed (yellow) line is the soil settlement profile before superimposing the pile settlement, and the full (purple) line is the settlement profile after the superimposition: the soil-pile differential settlement, the 'deflection', is not replicated in the soil mesh supporting the GR.

Attempting to circumvent this problem, several modelling alternatives were tested, each with its set of limitations.

- Moving the EBR's *fixed point* to the top instead of the bottom (Figure 6.7) prevents embankment settlement through the EBR element, but introduces a problem of its own: soil sliding along the pile shaft is restricted and pile-soil settlement is thus vastly underestimated.
- Placing a plate element on top of the EBR element (as shown in Figure 6.8) would also prevent embankment settlement through the EBR, as it would act as a physical barrier between the embankment and the EBR. In this case, the EBR's top node would be fixed to the plate's middle node, as seen in Figure 6.8 below. However, this is not realistic as it artificially increases the load transfer to the pile, thus unrealistically increasing the arching efficacy of the system.

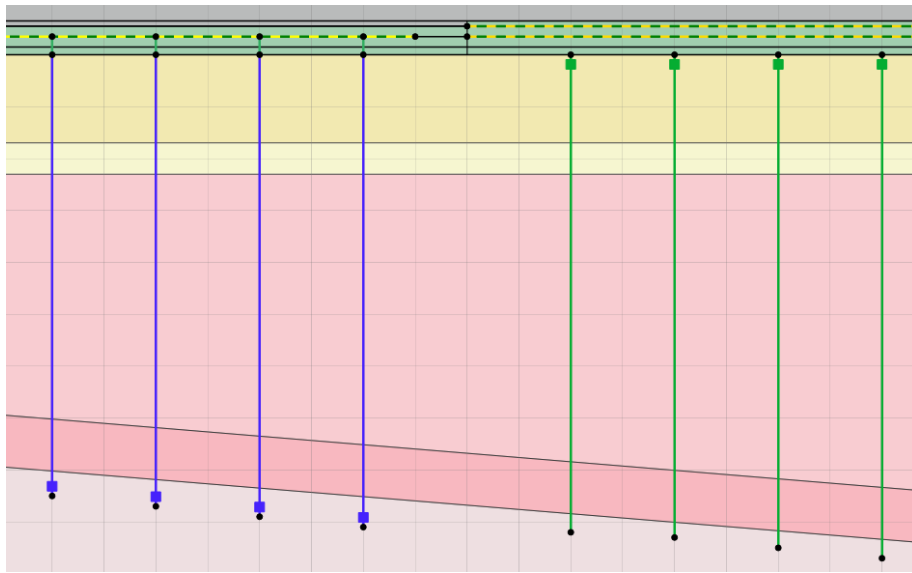


Figure 6.7 – EBR element fixed to the soil mesh at its bottom node (left) and top node (right)

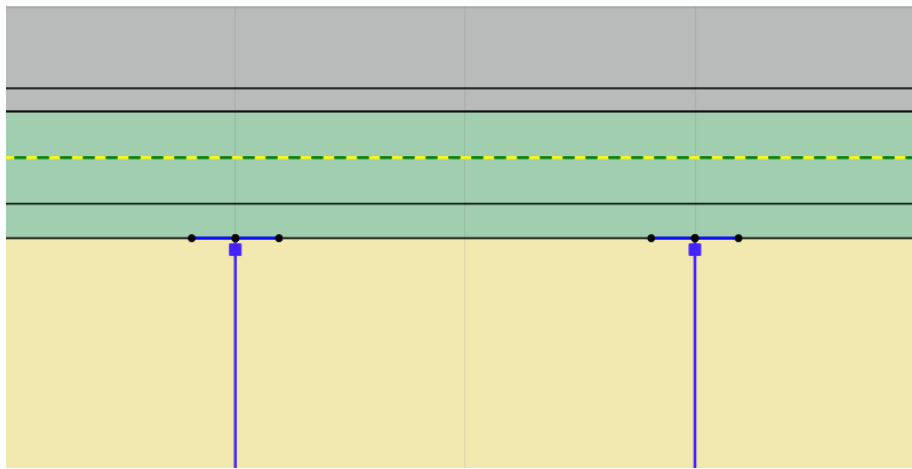


Figure 6.8 – EBR element fixed to a plate element at its top node

- One proto-fix is to attach an anchor between the pile top and the geogrid (Figure 6.9) and assign to it an elasticity modulus equal to that of the surrounding load transfer platform, as can be seen in Figure 6.9 below. This mimics the physical barrier (that is the pile) which would in reality cause this deflection to form. However, this inevitably results in an unrealistic concentration of the strain at the anchor-GR connection node, and thus overestimates the maximum strain which would otherwise spread over the pile head area.

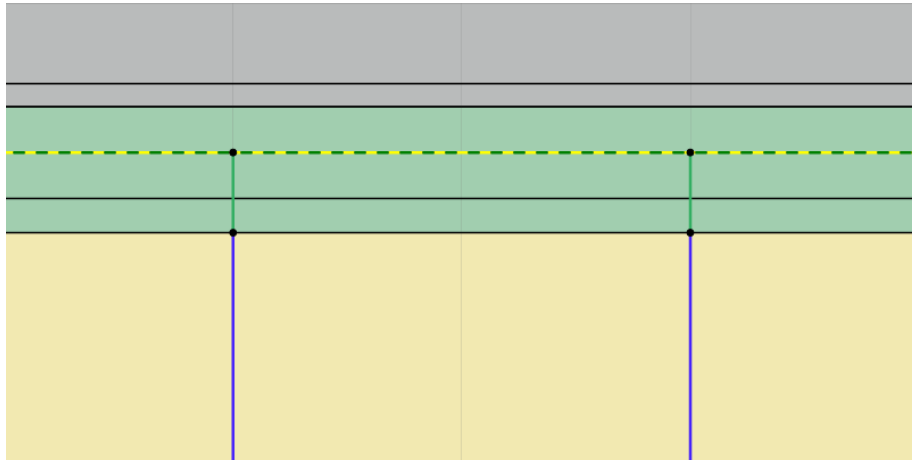


Figure 6.9 – Anchor element with LTP rigidity separating EBR element and geogrid

6.2 Analytical models: EBGeo and CUR 226

This section assesses the 1) GR displacement and 2) GR strain predictions of the German (EBGeo 2011) and Dutch (CUR 226 2016) guidelines.

The two guidelines were codified in two Excel sheets (Appendices B and C) and values in Table 6.1 were used as input.

Table 6.1 – Input parameters into the German EBGeo and Dutch CUR226 guidelines

s_x [m]	2
s_y [m]	2
d [m]	0.38
φ [°]	53*
γ [kN/m ³]	19.1
H [m]	4.65
k_s [kN/m ³]	317 [†]
J [kN/m]	750 (3R)

*This value was calculated as the equivalent friction angle at $c=0$ given the high cohesion of the fill ($c= 61$ kPa). It is calculated using the equation $\varphi = \text{atan} \frac{\sigma_v \tan \varphi + c}{\sigma_v}$ following van Eekelen et al., 2015

[†] This value is calculated using a thickness-weighted average of the subsoil layers MC,C, SC1, and SC2 as per EBGeo guideline. Full calculation found in Appendix B.1

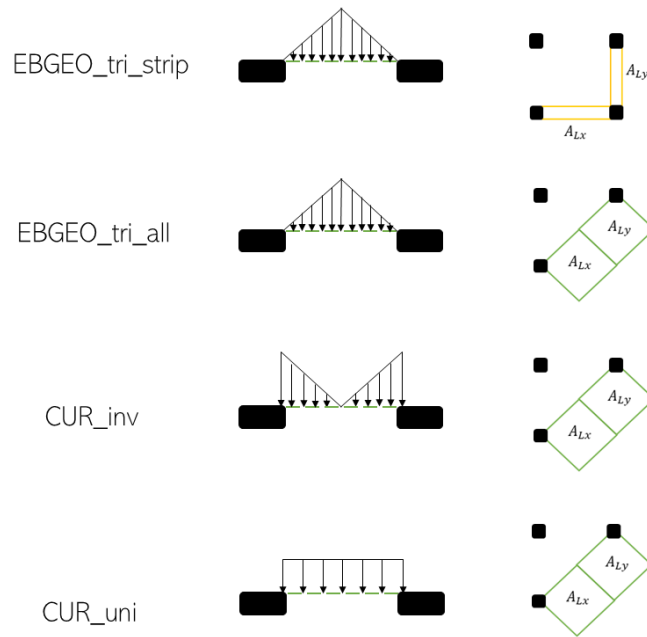


Figure 6.10 – The four analytical models used to predict maximum strain in test section 3R

For the EBGEO guideline, a triangular GR load is assumed (EBGEO_tri in graphs below). For subsoil support mobilization, the EBGEO guideline only mobilizes the support under the GR strip, yet van Eekelen, 2015 suggests mobilizing the whole area. Both variations are tested (EBGEO_tri_strip and EBGEO_tri_full below).

Using the CUR226 guidelines, both uniform and inverse triangular GR load distributions are tested. (CUR_inv and CUR_uni respectively)

GR displacement and maximum strain are computed. Given that no information about GR displacement is reported in Briançon and Simon, 2012 or Nunez et al., 2013, the computed GR displacement is compared to measured subsoil displacement and that output by PLAXIS 2D. This, of course, assumes an incompressible LTP which displaces with the underlying subsoil.

6.3 Results

GR Displacement

Figure 6.11 shows the GR displacement in section 3R predicted by the EBGEO guideline, both with strip and full subsoil mobilization, and the CUR226 guideline, both with uniform and inverse triangular GR load distributions. These are plotted along the PLAXIS output (calibrated against measured differential settlement), and reported measurements.

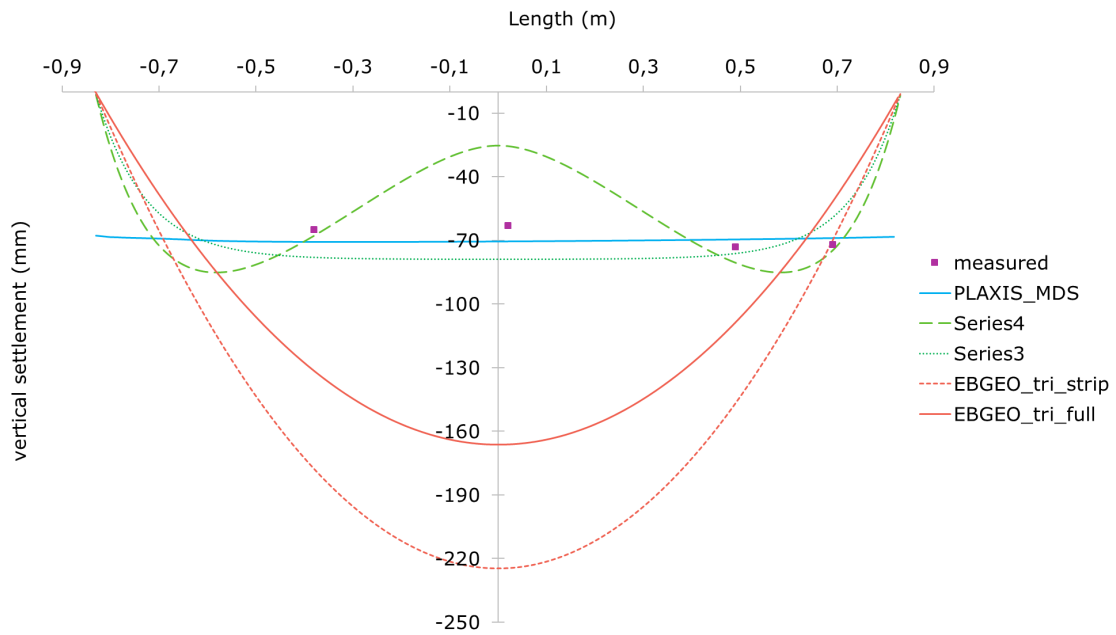


Figure 6.11 – GR deflection predicted by different models

GR Strain

Figure 6.12 shows the predicted maximum strain by the analytical models considered compared to the PLAXIS models and reported measurements in 3R.

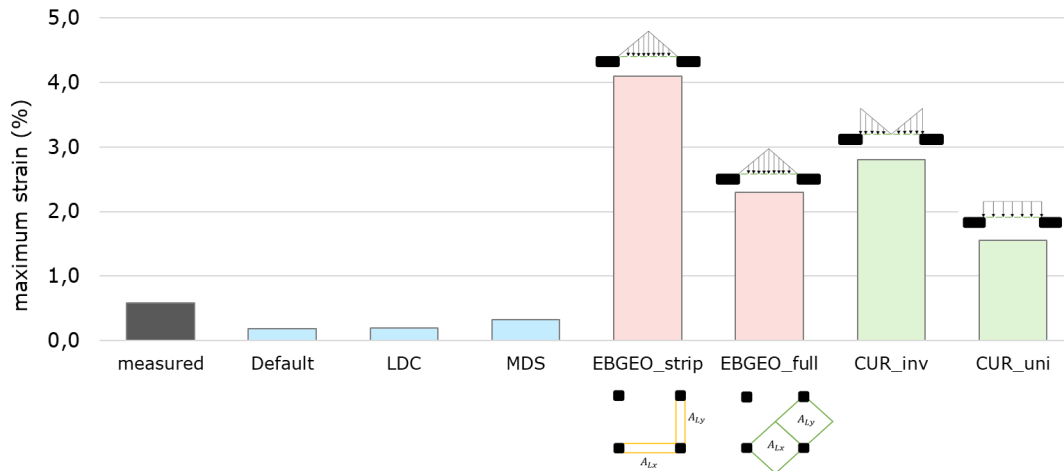


Figure 6.12 – Maximum GR strain predicted by different models

6.4 Discussion

As expected, the inclusion of subgrade support from the whole influence area as opposed to only the GR strip decreased GR displacement and thus better predicted maximum strain. This inclusion thus improved the predictions for the ASIRI case, particularly given the substantial subsoil support at the embankment site (calculated in Appendix B.1 at 317 kN/m^3).

Among the fully supported models, the inverse triangular one gave the highest overestimate of strain, likely due to its GR deformation shape which overestimated deflection near the piles compared to measurements. Both the uniform and triangular distributions resulted in lower overestimations of strain, and were most in-agreement with measurements for GR displacement. This is likely due to the high subgrade support at the ASIRI site which results in a more uniform settlement between piles and thus a more uniform GR load.

Based on the literature review conducted in Section 2.2, the triangular distribution was deemed as the least realistic of all GR load distributions regardless of the state of subsoil support. However, this was not the case with the ASIRI 3R test section. This may be due to the phenomenon of 'soil sliding' along the pile shafts noted in the ASIRI site, where soil settlement near the pile shaft was higher than that at midspan (see reported measured points in Figure 6.11 above and 6.13 below).

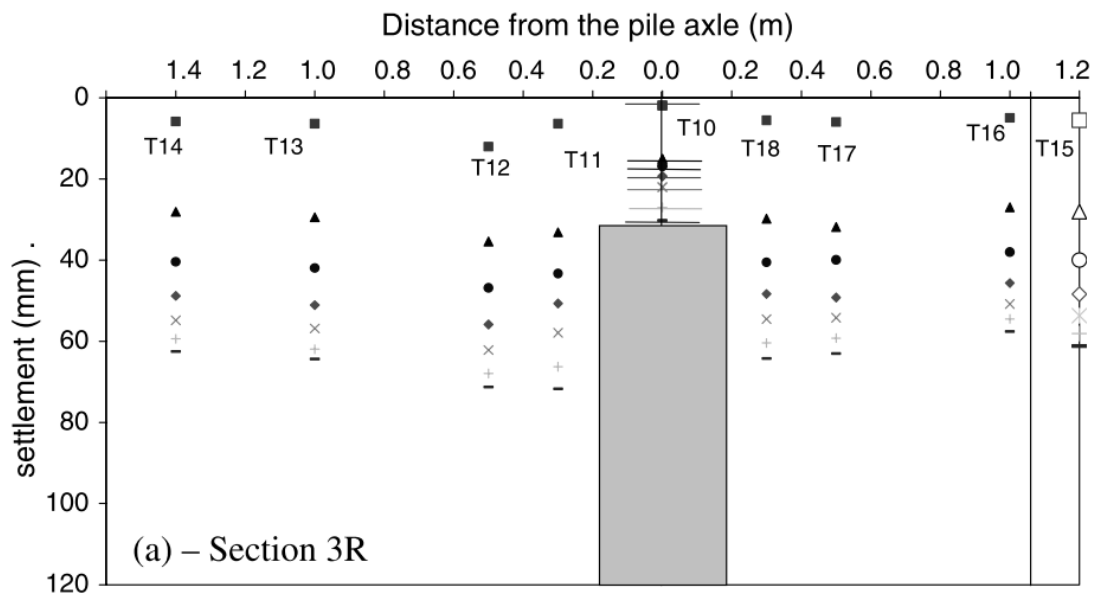


Figure 6.13 – Higher soil settlement reported near the pile compared to midspan between piles, as reported by Briançon and Simon, 2012

Chapter 7

Summary and Future Work

7.1 Summary

This thesis explored three main topics related to Geosynthetically Reinforced Piled Embankment (GRPE) systems:

- A literature review of GRPE design guidelines, particularly the British BS8006 2010, the German EBGEO 2011, and the Dutch CUR 226 2016. The review of reported validation studies comparing the accuracy of these guidelines shows a high sensitivity to embankment friction angle, with the German EBGEO tending to overestimate arching at lower friction angles, and the British BS8006 underestimating it at higher friction angles. The review also shows that the GR load distribution is highly dependent on the state of subsoil support, with a uniform distribution being more appropriate for high subsoil support, and an inverse triangular one more appropriate for less subsoil support.
- A validation of PLAXIS 2D for modelling GRPE systems was carried out. EBR elements were used to represent piles and their interface stiffness factors were calibrated using several methods: to the load displacement curve, to measured load displacement, and to soil-pile differential settlement. The analysis shows that the natural deviation of pile behavior from the load-displacement curve of a test pile results in a wide range of possible calibration values for the ISFs, rendering this method of calibration unpractical.

It is thus recommended to base the calibration process on the pile's load and displacement and the surrounding subsoil settlement to avoid an excessive divergence in predicted subsoil settlement. This is particularly relevant given the results of Chapter 5.1 which showed that ISF's have a much more pronounced effect on soil settlement than on pile settlement.

The analysis also shows that having information about the distribution of shear resistance along the pile shaft (from a static load test) is effective in narrowing down

the calibration process.

Results also show that PLAXIS 2D underestimates GR strain due to its inability to accurately model GR sags: EBR elements are *superimposed*, on top of a continuous soil mesh, thus allowing the embankment soil to settle through the EBR. This prevents the formation of a GR sag as would realistically happen, thus resulting in an underestimation of GR strain.

- The comparison of German EBGeo (2011) and Dutch CUR 226 (2016) predictions for GR displacement and strain to measured results shows several key points: First, including the subsoil support under the whole GR instead of only the GR strips gave better predictions, particularly given the high subsoil support at the ASIRI site. In regards to the GR load distribution, both the uniform and triangular distribution gave better results compared to the inverse triangular one - in a slight divergence from results of the literature review. This was likely due to the high subsoil support and the phenomenon of soil sliding along the pile shaft at the ASIRI site.

7.2 Future work

Rigid models such as the SINTEF model have not been widely explored since European codes adopted limit-equilibrium models like the Hewlett & Randolph, the Zaeske, and the Concentric Arches model. These are comparatively more computation-intensive compared to rigid arch models.

A well calibrated rigid arch model might thus offer a good preliminary approximation of arching efficacy and GR load for designers. It would thus be of great value to possibly calibrate the β value in the SINTEF model as a function of pile spacing and embankment friction angle using a calibrated numeric model.

It would additionally be of great use to further explore the use of anchors in PLAXIS 2D models to better simulate GR sags, particularly to circumvent the issue of strain localization at anchor-GR connection points.

Bibliography

- Bhasi, A., & Rajagopal, K. (2015). Geosynthetic-reinforced piled embankments : Comparison of numerical and analytical methods, *15*(5), 1–12.
- Briançon, L., & Simon, B. (2012). Performance of pile-supported embankment over soft soil: Full-scale experiment. *Journal of Geotechnical and Geoenvironmental Engineering*, *138*(52), 551–561.
- Brinkgreve, R. B. J., Kumarswamy, S., & Foria, F. (2017). *Modelling of a pile row in a 2d plane strain fe anlaysis*, Numerical Methods in Geotechnical Engineering.
- BSI. (2010). *Bs8006-2010 code of practice for strengthened/reinforced soils and other fill*. British Standards Institution.
- Collin, J. (2013). Geosynthetic-Reinforced Column-Support Embankment Design Guidelines Geosynthetic-Reinforced Column-Support Embankment Design Guidelines, (December).
- Edgers, L. (2016). *A Comparison of 2D and 3D Settlement Analyses of the Tower of Pisa*, Geo-Frontiers Congress 2011, Vol. 41165. *March 2011*.
- Eiksund, G., Svanø, G., & Watn, A. (2000). Alternative calculation principle for design of piled embankments with base reinforcement. *4th International Conference on Ground Improvement Geosystems*, *13*(52), 123–456.
- GSC. (2011). *Recommendations for design and analysis of earth structures using geosynthetic reinforcements (ebgeo)*. Ernst Sohn GmbH Co. KG.
- Gunnvard, P. (2016). *Evaluation of the Efficiency of the Standardized Norrland Method Analyses with the finite element program PLAXIS on the case of road 685*, Master Thesis. Luleå University of Technology.
- Khansari, A., & Vollmert, L. (2018). Technical Note Load transfer and deformation of geogrid-reinforced piled embankments : field measurement, (2010).
- King, A., L.and Bouazza, Dubsy, S., Rowe, R., Gniel, J., & Bui, H. (2019). Kinematics of soil arching in piled embankments. *Géotechnique*, *69*(52), 941–958.
- Nunez, M. A., Briançon, L., & Dias, D. (2013). Asiri case study: Analyses of a pile-supported embankment over soft clay: Full-scale experiment, analytical and numerical approaches. *Engineering Geology*, *153*, 53–67.
- Oh, Y. I., & Shin, E. C. (2007). Reinforcement and arching effect of geogrid-reinforced and pile-supported embankment on marine soft ground. *Marine Georesources & Geotechnology*, *25*(2), 97–118.

- Pedersen, B., & Bjorn, J. A. (2014). *Modelling of a piled raft foundation as a plane strain model in PLAXIS 2D*, Master Thesis. Chalmers University University of Technology.
- Plaxis2D. (2019a). Plaxis 2d reference manual connect edition v20.
- Plaxis2D. (2019b). Plaxis material models manual.
- Satibi, S. (2014). Numerical analysis and design criteria of embankments on floating piles.
- Sluis, J., Besseling, F., & Stuurwold, P. (2014). Modelling of a pile row in a 2d plane strain fe-analysis. *Numerical Methods in Geotechnical Engineering*, (6).
- Torggler, N. (2016). *Numerical Studies of Embedded Beam Row in Safety Analysis in PLAXIS 2D*, Master Thesis. Graz University of Technology.
- Trafikverket. (2016). Trafikverkets tekniska krav for geokonstruktioner tdok 2013:0667 (tk geo 13).
- van Eekelen, S. (2015). *Basal reinforced piled embankments experiments, field studies and the development and validation of a new analytical design model*. CPI – Koninklijke Wörmann, Zutphen, Netherlands.
- van Eekelen, S., Bezuijen, A., & Alexiew, D. (2008). *Piled embankments in the netherlands, a full-scale test, comparing 2 years of measurements with design calculations*, Fourth European Geosynthetics Conference.
- van Eekelen, S., Bezuijen, A., Lodder, H., & van Tol, A. (2012). Model experiments on piled embankments. part ii. *Geotextiles and Geomembranes*, 32, 82–94.
- van Eekelen, S., Bezuijen, A., Lodder, H., & van Tol, A. (2015). Validation of analytical models for the design of basal reinforced piled embankments. *Geotextiles and Geomembranes*, 43, 56–81.
- van Eekelen, S., & Brugman, M. (2016). *Cur 226 design guideline for basal reinforced piled embankment systems*. CRC Press.
- Zaeske, D., & Kempfert, H.-G. (2002). Berechnung und wirkungsweise von unbewehrten und bewehrten und mineralischen tragschichten auf punkt-linienförmigen traggliedern. *Bauingenieur*, Band 77, (February).

Appendix A

Reported Data from Case Studies

A.1 ASIRI

Soil parameters.

Parameter		Embankment fill	Load transfer platform	Silty clay (dry crust)	Clay	Sandy clays 1	Sandy clays 2	Sand and gravel alluvial deposits
Density, γ	[kN/m ³]	19.1	21	20	15	20	20	20
Thickness, Δz	[m]			1.7	0.6	4.2	1.5–2.5	
CC/(1 + e ₀)	[-]			0.1	0.2	0.06	0.08	
Compressibility indices,								
CC	[-]			0.2	0.54	0.1	0.13	
λ	[-]			0.087	0.235	0.044	0.056	
Swelling indices,								
CS	[-]			0.03	0.05	0.01	0.01	
κ	[-]			0.013	0.022	0.005	0.004	
Void ratio, e ₀	[-]			1	1.7	0.7	0.6	
Friction ratio, φ'	[°]	36.6	36	26	26	26	26	33
Cohesion, c'	[kPa]	17.3	61	0	0	0	0	0
Dilatancy, ψ'	[°]	6.6	3				3	
Overconsolidation pressure, σ'_p	[kPa]			30				
Pressuremeter modulus, EM	[MPa]							34.5
Pressuremeter limit pressure, PI	[MPa]							2.3
Elastic modulus, E	[MPa]		70					76.6
Poisson ratio, ν	[-]	0.3	0.3					0.3

Figure A.1 – Soil parameters reported by Nunez et al., 2013

Layer	Thickness (m)	γ (kN/m ³)	w (%)	Cc/1 + e ₀ (-)	I _p (%)	qc (MPa)	ϕ' (°)	c' (kPa)
CM	1.5	19.6	31	0.1	22	< 2	30	4
C	1	14.1	60	0.2	—	< 2	—	—
SC	6–8	20.8	31	0.07	12	< 2	26	13

Note: γ = unit weight; w = water content; e₀ = void ratio; Cc = compression index; I_p = plasticity index; qc = cone resistance; ϕ' = effective friction angle; c' = effective cohesion.

Figure A.2 – Soil parameters reported by Briançon and Simon, 2012

γ_d (kN/m ³)	0	D_{50} (mm)	D_{max} (mm)	C_c (-)	C_u (-)	ϕ' (°)	c' (kPa)
20.0	9.2	5	40	1.02	12.2	36	60

Note: γ_d = dry unit weight under 95% Modified Proctor Compaction; D_{50} = 50% finer than size; D_{max} = maximum diameter of particles; C_c = coefficient of curvature; C_u = coefficient of uniformity; ϕ' = effective friction angle; c' = effective cohesion.

Figure A.3 – LTP parameters reported by Briançon and Simon, 2012

Properties (EN ISO 10319)	Unit	GTX	GGR
Tensile strength	MD (min)	79 (75)	58 (55)
	CD (min)	79 (75)	58 (55)
Elongation at nominal strength (MD/CD)	%	10/10	10.5/10
Tensile strength at:	2%, MD and CD	16	10
	3%, MD and CD	22	13
	5%, MD and CD	37	17

Note: MD = machine direction; CD = cross direction.

Figure A.4 – Geogrid and Geotextile parameters as reported by Briançon and Simon, 2012

Equations used to deduce Hardening Soil model parameters E_{oed} , E_{50} , and E_{ur} from reported E and ν :

$$E_{oed} = \frac{E}{1 - \frac{2\nu^2}{1-\nu}} \quad (A.1)$$

$$E_{oed} = E_{50} = \frac{1}{3}E_{ur} \quad (A.2)$$

Appendix B

Excel sheet for German Design Code EBGEO

EBGEO (2010)

Recommendations for Design and Analysis of Earth Structures using Geosynthetic Reinforcements

Note: Equations used referenced by their number in the design code document

I. Input

1. Geometry

h (m)	5
a (m)	0,38
s _x (m)	2
s _y (m)	2
z (m)	0,35

2. Fill

γ (kN/m ³)	19,1
P _{G,k} (kN/m ²)	0
φ' _k (deg)	53
K _{crit}	8,9

(eqn 9.7)

II. Model Geometry

s(m)	2,83	
A _e (m ²)	4	(Fig 9.4)
A _s (m ²)	0,11	(Fig 9.4)
h _g (m)	1,00	(Fig 9.6)
b _{ers} (m)	0,34	(eqn 9.17)
A _{Lx} (m)	1,9	(eqn 9.18)
A _{ly} (m)	1,9	(eqn 9.19)
L _{w,x} (m)	1,66	(Fig 9.15)
L _{w,y} (m)	1,66	(Fig 9.15)

III. Subgrade Support

k _s (kN/m ³)	317	(Fig 9.26)
k _{s, full} (kN/m ³)	1100	(Eqn 5.7, van Eekelen 2015)*
J (kN/m)	750	

*Modified k_s to mobilize subgrade support under full influence area instead of just strip, from van Eekelen (2015)

Boundary Condition Checks

s	2	Valid
h/(s-a)	3	Valid
z	0,35	Fail

III. Calculation Constants

X	1,70	(eqn 9.8)
λ_1	0,75	(eqn 9.9)
λ_2	0,63	(eqn 9.10)

IV. Load Distribution

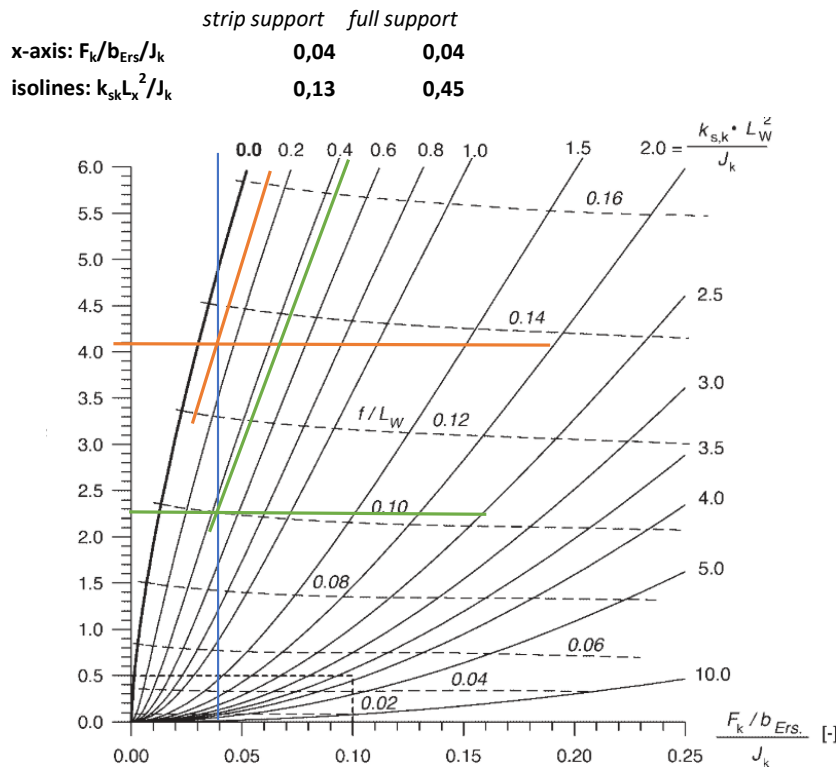
$\sigma_{z0,G,k}$ (kPa)	41,0	(eqn 9.6)
$\sigma_{zs,G,k}$ (kPa)	1963	(eqn 9.11)
$F_{s,G,k}$ (kN)	223	(eqn 9.13)
E_L (%)	58	(eqn 9.4)

V. GR Forces: triangular load distribution

$F_{x,G,k}$ (kN)	80	(eqn 9.20)
$F_{y,G,k}$ (kN)	80	(eqn 9.22)

VI. Graph Inputs

K_{sk} (kN/m ³)	317
$k_{s,full}$ (kN/m ³)	1100
$L_{w,x}$ (m)	1,66
J (kN/m)	6750
$F_k = F_{x,G,k}$ (kN)	80



VI. Read off graph

	strip support	full support
ϵ_{\max} (%)	4,1	2,3
f/L_w	0,135	0,1

	strip support	full support
T_{\max} (kN)	277	155
f	0,225	0,166

VI. GR Displacement graph

EBGEO assumes a parabolic sag with equation $y=ax^2 + f$

	strip support	full support
$D = L_{wx}$ (m)	1,66	1,66
$r = D/2$	0,83	0,83
f	0,22	0,17
$a = -f^2/r$	-0,32	-0,24

strip support			full support		
x	y(x)	y(x)(mm)	x	y(x)	y(x)(mm)
0,00	-0,2245	-224,5	0,00	-0,1663	-166,3
0,005	-0,2245	-224,5	0,005	-0,1663	-166,3
0,010	-0,2245	-224,5	0,010	-0,1663	-166,3
0,015	-0,2245	-224,5	0,015	-0,1663	-166,3
0,020	-0,2244	-224,4	0,020	-0,1662	-166,2
0,025	-0,2243	-224,3	0,025	-0,1662	-166,2
0,030	-0,2242	-224,2	0,030	-0,1661	-166,1
0,035	-0,2241	-224,1	0,035	-0,1660	-166,0
0,040	-0,2240	-224,0	0,040	-0,1659	-165,9
0,045	-0,2239	-223,9	0,045	-0,1658	-165,8
0,050	-0,2237	-223,7	0,050	-0,1657	-165,7
0,055	-0,2236	-223,6	0,055	-0,1656	-165,6
0,060	-0,2234	-223,4	0,060	-0,1655	-165,5
0,065	-0,2232	-223,2	0,065	-0,1653	-165,3
0,070	-0,2229	-222,9	0,070	-0,1651	-165,1
0,075	-0,2227	-222,7	0,075	-0,1650	-165,0
0,080	-0,2225	-222,5	0,080	-0,1648	-164,8
0,085	-0,2222	-222,2	0,085	-0,1646	-164,6
0,090	-0,2219	-221,9	0,090	-0,1644	-164,4
0,095	-0,2216	-221,6	0,095	-0,1642	-164,2
0,100	-0,2213	-221,3	0,100	-0,1639	-163,9
0,105	-0,2210	-221,0	0,105	-0,1637	-163,7
0,110	-0,2206	-220,6	0,110	-0,1634	-163,4
0,115	-0,2202	-220,2	0,115	-0,1631	-163,1
0,120	-0,2199	-219,9	0,120	-0,1629	-162,9
0,125	-0,2195	-219,5	0,125	-0,1626	-162,6
0,130	-0,2190	-219,0	0,130	-0,1623	-162,3
0,135	-0,2186	-218,6	0,135	-0,1619	-161,9

0,140	-0,2182	-218,2	0,140	-0,1616	-161,6
0,145	-0,2177	-217,7	0,145	-0,1613	-161,3
0,150	-0,2172	-217,2	0,150	-0,1609	-160,9
0,155	-0,2167	-216,7	0,155	-0,1605	-160,5
0,160	-0,2162	-216,2	0,160	-0,1602	-160,2
0,165	-0,2157	-215,7	0,165	-0,1598	-159,8
0,170	-0,2152	-215,2	0,170	-0,1594	-159,4
0,175	-0,2146	-214,6	0,175	-0,1590	-159,0
0,180	-0,2140	-214,0	0,180	-0,1585	-158,5
0,185	-0,2134	-213,4	0,185	-0,1581	-158,1
0,190	-0,2128	-212,8	0,190	-0,1576	-157,6
0,195	-0,2122	-212,2	0,195	-0,1572	-157,2
0,200	-0,2115	-211,5	0,200	-0,1567	-156,7
0,205	-0,2109	-210,9	0,205	-0,1562	-156,2
0,210	-0,2102	-210,2	0,210	-0,1557	-155,7
0,215	-0,2095	-209,5	0,215	-0,1552	-155,2
0,220	-0,2088	-208,8	0,220	-0,1547	-154,7
0,225	-0,2081	-208,1	0,225	-0,1541	-154,1
0,230	-0,2074	-207,4	0,230	-0,1536	-153,6
0,235	-0,2066	-206,6	0,235	-0,1530	-153,0
0,240	-0,2058	-205,8	0,240	-0,1525	-152,5
0,245	-0,2050	-205,0	0,245	-0,1519	-151,9
0,250	-0,2042	-204,2	0,250	-0,1513	-151,3
0,255	-0,2034	-203,4	0,255	-0,1507	-150,7
0,260	-0,2026	-202,6	0,260	-0,1501	-150,1
0,265	-0,2017	-201,7	0,265	-0,1494	-149,4
0,270	-0,2009	-200,9	0,270	-0,1488	-148,8
0,275	-0,2000	-200,0	0,275	-0,1481	-148,1
0,280	-0,1991	-199,1	0,280	-0,1475	-147,5
0,285	-0,1982	-198,2	0,285	-0,1468	-146,8
0,290	-0,1972	-197,2	0,290	-0,1461	-146,1
0,295	-0,1963	-196,3	0,295	-0,1454	-145,4
0,300	-0,1953	-195,3	0,300	-0,1447	-144,7
0,305	-0,1943	-194,3	0,305	-0,1440	-144,0
0,310	-0,1933	-193,3	0,310	-0,1432	-143,2
0,315	-0,1923	-192,3	0,315	-0,1425	-142,5
0,320	-0,1913	-191,3	0,320	-0,1417	-141,7
0,325	-0,1902	-190,2	0,325	-0,1409	-140,9
0,330	-0,1892	-189,2	0,330	-0,1401	-140,1
0,335	-0,1881	-188,1	0,335	-0,1393	-139,3
0,340	-0,1870	-187,0	0,340	-0,1385	-138,5
0,345	-0,1859	-185,9	0,345	-0,1377	-137,7
0,350	-0,1848	-184,8	0,350	-0,1369	-136,9
0,355	-0,1836	-183,6	0,355	-0,1360	-136,0
0,360	-0,1825	-182,5	0,360	-0,1352	-135,2
0,365	-0,1813	-181,3	0,365	-0,1343	-134,3
0,370	-0,1801	-180,1	0,370	-0,1334	-133,4
0,375	-0,1789	-178,9	0,375	-0,1325	-132,5
0,380	-0,1777	-177,7	0,380	-0,1316	-131,6
0,385	-0,1764	-176,4	0,385	-0,1307	-130,7

0,390	-0,1752	-175,2	0,390	-0,1297	-129,7
0,395	-0,1739	-173,9	0,395	-0,1288	-128,8
0,400	-0,1726	-172,6	0,400	-0,1278	-127,8
0,405	-0,1713	-171,3	0,405	-0,1269	-126,9
0,410	-0,1700	-170,0	0,410	-0,1259	-125,9
0,415	-0,1686	-168,6	0,415	-0,1249	-124,9
0,420	-0,1673	-167,3	0,420	-0,1239	-123,9
0,425	-0,1659	-165,9	0,425	-0,1229	-122,9
0,430	-0,1645	-164,5	0,430	-0,1219	-121,9
0,435	-0,1631	-163,1	0,435	-0,1208	-120,8
0,440	-0,1617	-161,7	0,440	-0,1198	-119,8
0,445	-0,1602	-160,2	0,445	-0,1187	-118,7
0,450	-0,1588	-158,8	0,450	-0,1176	-117,6
0,455	-0,1573	-157,3	0,455	-0,1165	-116,5
0,460	-0,1558	-155,8	0,460	-0,1154	-115,4
0,465	-0,1543	-154,3	0,465	-0,1143	-114,3
0,470	-0,1528	-152,8	0,470	-0,1132	-113,2
0,475	-0,1513	-151,3	0,475	-0,1121	-112,1
0,480	-0,1497	-149,7	0,480	-0,1109	-110,9
0,485	-0,1482	-148,2	0,485	-0,1098	-109,8
0,490	-0,1466	-146,6	0,490	-0,1086	-108,6
0,495	-0,1450	-145,0	0,495	-0,1074	-107,4
0,500	-0,1434	-143,4	0,500	-0,1062	-106,2
0,505	-0,1417	-141,7	0,505	-0,1050	-105,0
0,510	-0,1401	-140,1	0,510	-0,1038	-103,8
0,515	-0,1384	-138,4	0,515	-0,1025	-102,5
0,520	-0,1367	-136,7	0,520	-0,1013	-101,3
0,525	-0,1350	-135,0	0,525	-0,1000	-100,0
0,530	-0,1333	-133,3	0,530	-0,0988	-98,8
0,535	-0,1316	-131,6	0,535	-0,0975	-97,5
0,540	-0,1299	-129,9	0,540	-0,0962	-96,2
0,545	-0,1281	-128,1	0,545	-0,0949	-94,9
0,550	-0,1263	-126,3	0,550	-0,0936	-93,6
0,555	-0,1245	-124,5	0,555	-0,0922	-92,2
0,560	-0,1227	-122,7	0,560	-0,0909	-90,9
0,565	-0,1209	-120,9	0,565	-0,0896	-89,6
0,570	-0,1191	-119,1	0,570	-0,0882	-88,2
0,575	-0,1172	-117,2	0,575	-0,0868	-86,8
0,580	-0,1153	-115,3	0,580	-0,0854	-85,4
0,585	-0,1134	-113,4	0,585	-0,0840	-84,0
0,590	-0,1115	-111,5	0,590	-0,0826	-82,6
0,595	-0,1096	-109,6	0,595	-0,0812	-81,2
0,600	-0,1077	-107,7	0,600	-0,0797	-79,7
0,605	-0,1057	-105,7	0,605	-0,0783	-78,3
0,610	-0,1037	-103,7	0,610	-0,0768	-76,8
0,615	-0,1017	-101,7	0,615	-0,0754	-75,4
0,620	-0,0997	-99,7	0,620	-0,0739	-73,9
0,625	-0,0977	-97,7	0,625	-0,0724	-72,4
0,630	-0,0957	-95,7	0,630	-0,0709	-70,9
0,635	-0,0936	-93,6	0,635	-0,0693	-69,3

B.1 Subgrade Support

From EBGEO, Equation 9.27:

$$k_s = \frac{\prod_{n=1}^i E_{s,n}}{\sum_{n=1}^i t_{W,n} \prod_{n=1}^i E_{s,m}}; m \neq n \quad (\text{B.1})$$

This can be rewritten as:

$$k_s = \frac{1}{\sum_{n=1}^i \frac{t_n}{E_n}} \quad (\text{B.2})$$

For the ASIRI site, this equates to:

$$k_s = \frac{1}{\frac{t_{CM}}{E_{CM}} + \frac{t_C}{E_c} + \frac{E_{SC1}}{E_{SC1}} + \frac{E_{SC2}}{E_{SC2}}} = \frac{1}{\frac{1.7m}{1845kN/m^2} + \frac{0.6m}{923kN/m^2} + \frac{3.7m}{3137kN/m^2} + \frac{1m}{2516kN/m^2}} = 317kN/m^3 \quad (\text{B.3})$$

Appendix C

Excel sheet for Dutch Design Code CUR-226

CUR 226 (2016)
Dutch Design Guideline for Basal Reinforced Piled Embankments

1. Input	
1. Geometry	
s_x [m]	2
s_y [m]	2
d [m]	0,38
J [kN/m]	750
2. Fill	
φ [deg]	53
K_p	8,93
γ [kN/m ³]	19,1
H [m]	4,65
$\sigma_{v, tot}$ [kPa]	88,8

II. Model Geometries	
s_0 [m]	2,8
b_{eq} [m]	0,34
A_{ix} [m ²]	1,94
A_{iy} [m ²]	1,94
L_{wx} [m]	1,66
L_{wy} [m]	1,66
H_{xg2D} [m]	1,00
H_{yg2D} [m]	1,00
L_{x2D} [m]	1,66
L_{y2D} [m]	1,66
L_{3D} [m]	1,66
H_{g3D} [m]	1,41

III. Subgrade support (k_s)				317
Jordart	Djup		Δz [m]	E [kN/m ³]
	från [m]	till [m]		
LTP	0,00	0,35	0,4	70000
dry crust	0,35	2,05	1,7	1845
clay	2,05	2,65	0,6	923
sandy clay 1	2,65	6,35	3,7	3137
sandy clay 2	6,35	7,35	1,0	2516

!! Boundary Condition Checks !!	
$b/s_x >= 0,15$	Valid
$b/s_y >= 0,15$	Valid
$H/(s_0 + d_{eq}) >= 0,66$	Valid

IV. Subgrade Support	
ks (kN/m ³)	317
K _x	1100
K _y	1100
J [kN/m]	750

V. Load Distribution	
B+C F _{GR,strip} + F _{GR,square} for p=0 for p>0	97,2 97,2
A F _{pile}	258,1
1. F _{GR,strip} for p=0 for p>0	76,1 76,1
2. F _{transferred}	224,6
3. F _{GRsquare} for p=0 for p>0	21,1 21,1
F _{GR,Sq1} + F _{GR,Sq2} + F _{GR,Sq3}	13,9
3.a F _{GR,Sq1}	7,2
3.b F _{GR,Sq2}	13,96
1F _{GR,Sq2}	25,28
2F _{GR,Sq2}	-13,10
3F _{GR,Sq2}	-18,90
4F _{GR,Sq2}	0
3.c F _{GR,Sq3}	0

Q _{2d}	24,61
P _{x2D}	2224,3
P _{y2D}	2224,3
F _{xGRstr2,p=0}	0
F _{yGRstr2,p=0}	0
p _{transferred}	182,1
P _{3D}	2,19
Q _{3D}	11,48

!! Force balance check !!	Valid
A+B+C	355,3
(σ _{v,tot}) _{x,sy}	355,3

Inverse triangular GR load distribution

Compute Table

V. GR Forces
Assuming inverse triangular distribution

0. Input from sheet Indata

q_{av} [kPa]	86,7
L_{wx} [m]	1,66
K_x	1100
J_x [kN/m]	750

Optimize

$\epsilon_{geom, avg}$ [%]	2,84
$\epsilon_{const, avg}$ [%]	2,84
Difference	0,0000

1. Optimized values

T_H [kN/m]	20,7
α_x	7,3
M_x	2,84E-02

2. Output

T_{max}	28,55
ϵ_{max}	3,81

x	$z_{inv_tri}(x)$	$z'_{inv_tri}(x)$	T(x)	$\epsilon_{geom, avg}$	$\epsilon_{const, avg}$
[m]	[m]	[m/m]	[kN/m]	[/100 %]	[/100 %]
0,000	2,53E-02	0,00E+00	20,733	0,028	0,028
0,005	2,53E-02	6,59E-03	20,733	0,005	0,104
0,010	2,54E-02	1,29E-02	20,735	0,005	0,104
0,015	2,54E-02	1,90E-02	20,737	0,005	0,104
0,020	2,56E-02	2,49E-02	20,739	0,005	0,104
0,025	2,57E-02	3,06E-02	20,743	0,005	0,104
0,030	2,59E-02	3,60E-02	20,746	0,005	0,104
0,035	2,61E-02	4,13E-02	20,751	0,005	0,104
0,040	2,63E-02	4,63E-02	20,755	0,005	0,104
0,045	2,65E-02	5,12E-02	20,760	0,005	0,104
0,050	2,68E-02	5,59E-02	20,765	0,005	0,104
0,055	2,71E-02	6,04E-02	20,771	0,005	0,104
0,060	2,74E-02	6,47E-02	20,776	0,005	0,104
0,065	2,77E-02	6,89E-02	20,782	0,005	0,104
0,070	2,81E-02	7,29E-02	20,788	0,005	0,104
0,075	2,84E-02	7,67E-02	20,794	0,005	0,104
0,080	2,88E-02	8,04E-02	20,800	0,005	0,104

0,085	2,93E-02	8,40E-02	20,806	0,005	0,104
0,090	2,97E-02	8,74E-02	20,812	0,005	0,104
0,095	3,01E-02	9,07E-02	20,818	0,005	0,104
0,100	3,06E-02	9,38E-02	20,824	0,005	0,104
0,105	3,11E-02	9,69E-02	20,830	0,005	0,104
0,110	3,16E-02	9,98E-02	20,836	0,005	0,104
0,115	3,21E-02	1,03E-01	20,842	0,005	0,104
0,120	3,26E-02	1,05E-01	20,847	0,005	0,104
0,125	3,31E-02	1,08E-01	20,853	0,005	0,104
0,130	3,37E-02	1,10E-01	20,858	0,005	0,104
0,135	3,42E-02	1,13E-01	20,864	0,005	0,104
0,140	3,48E-02	1,15E-01	20,869	0,005	0,104
0,145	3,54E-02	1,17E-01	20,874	0,005	0,104
0,150	3,60E-02	1,19E-01	20,879	0,005	0,104
0,155	3,66E-02	1,21E-01	20,884	0,005	0,104
0,160	3,72E-02	1,23E-01	20,889	0,005	0,104
0,165	3,78E-02	1,24E-01	20,893	0,005	0,104
0,170	3,84E-02	1,26E-01	20,897	0,005	0,104
0,175	3,90E-02	1,28E-01	20,901	0,005	0,105
0,180	3,97E-02	1,29E-01	20,905	0,005	0,105
0,185	4,03E-02	1,31E-01	20,909	0,005	0,105
0,190	4,10E-02	1,32E-01	20,913	0,005	0,105
0,195	4,17E-02	1,33E-01	20,916	0,005	0,105
0,200	4,23E-02	1,35E-01	20,920	0,005	0,105
0,205	4,30E-02	1,36E-01	20,923	0,005	0,105
0,210	4,37E-02	1,37E-01	20,926	0,005	0,105
0,215	4,44E-02	1,38E-01	20,929	0,005	0,105
0,220	4,51E-02	1,39E-01	20,931	0,005	0,105
0,225	4,58E-02	1,39E-01	20,934	0,005	0,105
0,230	4,65E-02	1,40E-01	20,936	0,005	0,105
0,235	4,72E-02	1,41E-01	20,938	0,005	0,105
0,240	4,79E-02	1,42E-01	20,940	0,005	0,105
0,245	4,86E-02	1,42E-01	20,942	0,005	0,105
0,250	4,93E-02	1,43E-01	20,943	0,005	0,105
0,255	5,00E-02	1,43E-01	20,945	0,005	0,105
0,260	5,07E-02	1,44E-01	20,946	0,005	0,105
0,265	5,14E-02	1,44E-01	20,947	0,005	0,105
0,270	5,22E-02	1,44E-01	20,948	0,005	0,105
0,275	5,29E-02	1,44E-01	20,948	0,005	0,105
0,280	5,36E-02	1,45E-01	20,949	0,005	0,105
0,285	5,43E-02	1,45E-01	20,949	0,005	0,105
0,290	5,50E-02	1,45E-01	20,949	0,005	0,105
0,295	5,58E-02	1,45E-01	20,949	0,005	0,105
0,300	5,65E-02	1,45E-01	20,949	0,005	0,105
0,305	5,72E-02	1,45E-01	20,948	0,005	0,105
0,310	5,79E-02	1,44E-01	20,948	0,005	0,105
0,315	5,87E-02	1,44E-01	20,947	0,005	0,105
0,320	5,94E-02	1,44E-01	20,946	0,005	0,105
0,325	6,01E-02	1,43E-01	20,945	0,005	0,105
0,330	6,08E-02	1,43E-01	20,944	0,005	0,105

0,335	6,15E-02	1,42E-01	20,942	0,005	0,105
0,340	6,22E-02	1,42E-01	20,941	0,005	0,105
0,345	6,29E-02	1,41E-01	20,939	0,005	0,105
0,350	6,37E-02	1,41E-01	20,937	0,005	0,105
0,355	6,44E-02	1,40E-01	20,935	0,005	0,105
0,360	6,51E-02	1,39E-01	20,932	0,005	0,105
0,365	6,57E-02	1,38E-01	20,930	0,005	0,105
0,370	6,64E-02	1,37E-01	20,927	0,005	0,105
0,375	6,71E-02	1,36E-01	20,924	0,005	0,105
0,380	6,78E-02	1,35E-01	20,921	0,005	0,105
0,385	6,85E-02	1,34E-01	20,918	0,005	0,105
0,390	6,91E-02	1,33E-01	20,915	0,005	0,105
0,395	6,98E-02	1,31E-01	20,911	0,005	0,105
0,400	7,04E-02	1,30E-01	20,907	0,005	0,105
0,405	7,11E-02	1,28E-01	20,903	0,005	0,105
0,410	7,17E-02	1,27E-01	20,899	0,005	0,104
0,415	7,24E-02	1,25E-01	20,895	0,005	0,104
0,420	7,30E-02	1,24E-01	20,891	0,005	0,104
0,425	7,36E-02	1,22E-01	20,886	0,005	0,104
0,430	7,42E-02	1,20E-01	20,881	0,005	0,104
0,435	7,48E-02	1,18E-01	20,876	0,005	0,104
0,440	7,54E-02	1,16E-01	20,871	0,005	0,104
0,445	7,60E-02	1,14E-01	20,866	0,005	0,104
0,450	7,65E-02	1,11E-01	20,861	0,005	0,104
0,455	7,71E-02	1,09E-01	20,856	0,005	0,104
0,460	7,76E-02	1,06E-01	20,850	0,005	0,104
0,465	7,81E-02	1,04E-01	20,844	0,005	0,104
0,470	7,86E-02	1,01E-01	20,839	0,005	0,104
0,475	7,91E-02	9,82E-02	20,833	0,005	0,104
0,480	7,96E-02	9,52E-02	20,827	0,005	0,104
0,485	8,01E-02	9,22E-02	20,821	0,005	0,104
0,490	8,05E-02	8,89E-02	20,815	0,005	0,104
0,495	8,10E-02	8,56E-02	20,809	0,005	0,104
0,500	8,14E-02	8,21E-02	20,803	0,005	0,104
0,505	8,18E-02	7,85E-02	20,797	0,005	0,104
0,510	8,22E-02	7,47E-02	20,791	0,005	0,104
0,515	8,25E-02	7,08E-02	20,785	0,005	0,104
0,520	8,29E-02	6,67E-02	20,779	0,005	0,104
0,525	8,32E-02	6,24E-02	20,773	0,005	0,104
0,530	8,35E-02	5,80E-02	20,768	0,005	0,104
0,535	8,38E-02	5,34E-02	20,762	0,005	0,104
0,540	8,41E-02	4,86E-02	20,757	0,005	0,104
0,545	8,43E-02	4,37E-02	20,753	0,005	0,104
0,550	8,45E-02	3,85E-02	20,748	0,005	0,104
0,555	8,47E-02	3,31E-02	20,744	0,005	0,104
0,560	8,48E-02	2,76E-02	20,741	0,005	0,104
0,565	8,49E-02	2,18E-02	20,738	0,005	0,104
0,570	8,50E-02	1,58E-02	20,736	0,005	0,104
0,575	8,51E-02	9,55E-03	20,734	0,005	0,104
0,580	8,51E-02	3,08E-03	20,733	0,005	0,104

0,585	8,51E-02	-3,65E-03	20,733	0,005	0,104
0,590	8,51E-02	-1,06E-02	20,734	0,005	0,104
0,595	8,50E-02	-1,79E-02	20,736	0,005	0,104
0,600	8,49E-02	-2,54E-02	20,740	0,005	0,104
0,605	8,48E-02	-3,32E-02	20,744	0,005	0,104
0,610	8,46E-02	-4,13E-02	20,751	0,005	0,104
0,615	8,44E-02	-4,97E-02	20,759	0,005	0,104
0,620	8,41E-02	-5,84E-02	20,768	0,005	0,104
0,625	8,38E-02	-6,75E-02	20,780	0,005	0,104
0,630	8,34E-02	-7,69E-02	20,794	0,005	0,104
0,635	8,30E-02	-8,66E-02	20,811	0,005	0,104
0,640	8,25E-02	-9,67E-02	20,830	0,005	0,104
0,645	8,20E-02	-1,07E-01	20,852	0,005	0,104
0,650	8,15E-02	-1,18E-01	20,877	0,005	0,104
0,655	8,09E-02	-1,29E-01	20,906	0,005	0,105
0,660	8,02E-02	-1,41E-01	20,938	0,005	0,105
0,665	7,94E-02	-1,53E-01	20,975	0,005	0,105
0,670	7,86E-02	-1,66E-01	21,016	0,005	0,105
0,675	7,78E-02	-1,79E-01	21,062	0,005	0,105
0,680	7,69E-02	-1,93E-01	21,114	0,005	0,106
0,685	7,59E-02	-2,07E-01	21,171	0,005	0,106
0,690	7,48E-02	-2,21E-01	21,234	0,005	0,106
0,695	7,36E-02	-2,36E-01	21,304	0,005	0,107
0,700	7,24E-02	-2,52E-01	21,382	0,005	0,107
0,705	7,11E-02	-2,68E-01	21,467	0,005	0,107
0,710	6,97E-02	-2,85E-01	21,560	0,005	0,108
0,715	6,83E-02	-3,03E-01	21,663	0,005	0,108
0,720	6,67E-02	-3,21E-01	21,775	0,005	0,109
0,725	6,51E-02	-3,40E-01	21,898	0,005	0,109
0,730	6,33E-02	-3,59E-01	22,032	0,005	0,110
0,735	6,15E-02	-3,80E-01	22,178	0,005	0,111
0,740	5,95E-02	-4,01E-01	22,336	0,005	0,112
0,745	5,74E-02	-4,23E-01	22,509	0,005	0,113
0,750	5,53E-02	-4,45E-01	22,696	0,005	0,113
0,755	5,30E-02	-4,69E-01	22,898	0,006	0,114
0,760	5,06E-02	-4,93E-01	23,117	0,006	0,116
0,765	4,81E-02	-5,18E-01	23,354	0,006	0,117
0,770	4,54E-02	-5,45E-01	23,609	0,006	0,118
0,775	4,26E-02	-5,72E-01	23,884	0,006	0,119
0,780	3,97E-02	-6,00E-01	24,179	0,006	0,121
0,785	3,66E-02	-6,29E-01	24,497	0,006	0,122
0,790	3,34E-02	-6,60E-01	24,837	0,006	0,124
0,795	3,00E-02	-6,91E-01	25,202	0,006	0,126
0,800	2,65E-02	-7,24E-01	25,593	0,006	0,128
0,805	2,28E-02	-7,58E-01	26,011	0,006	0,130
0,810	1,89E-02	-7,93E-01	26,456	0,006	0,132
0,815	1,48E-02	-8,29E-01	26,931	0,006	0,135
0,820	1,06E-02	-8,67E-01	27,438	0,007	0,137
0,825	6,17E-03	-9,06E-01	27,976	0,007	0,140
0,830	1,54E-03	-9,47E-01	28,548	0,007	0,143

Uniform GR load distribution

Compute Table

V. GR Forces
Assuming inverse triangular distribution

0. Input from sheet Indata

q_{av} [kPa]	86,7
L_{wx} [m]	1,66
K_x	1100
J_x [kN/m]	750

Optimize

$\epsilon_{geom, avg}$ [%]	1,55
$\epsilon_{const, avg}$ [%]	1,55
Difference	0,0000

1. Optimized values

TH [kN/m]	11,4
α_x	9,8

2. Output

T_{max}	14,39
ϵ_{max}	1,92

x	$z_{inv_tri}(x)$	$z'_{inv_tri}(x)$	T(x)	$\epsilon_{geom, avg}$	$\epsilon_{const, avg}$
[m]	[m]	[m/m]	[kN/m]	[/100 %]	[/100 %]
0,000	7,88E-02	0,00E+00	11,45	0,016	0,016
0,005	7,88E-02	-2,18E-05	11,45	0,005	0,057
0,010	7,88E-02	-4,37E-05	11,45	0,005	0,057
0,015	7,88E-02	-6,57E-05	11,45	0,005	0,057
0,020	7,88E-02	-8,79E-05	11,45	0,005	0,057
0,025	7,88E-02	-1,10E-04	11,45	0,005	0,057
0,030	7,88E-02	-1,33E-04	11,45	0,005	0,057
0,035	7,88E-02	-1,56E-04	11,45	0,005	0,057
0,040	7,88E-02	-1,79E-04	11,45	0,005	0,057
0,045	7,88E-02	-2,03E-04	11,45	0,005	0,057
0,050	7,88E-02	-2,27E-04	11,45	0,005	0,057
0,055	7,88E-02	-2,52E-04	11,45	0,005	0,057
0,060	7,88E-02	-2,77E-04	11,45	0,005	0,057
0,065	7,88E-02	-3,03E-04	11,45	0,005	0,057
0,070	7,88E-02	-3,30E-04	11,45	0,005	0,057
0,075	7,88E-02	-3,58E-04	11,45	0,005	0,057
0,080	7,88E-02	-3,86E-04	11,45	0,005	0,057

0,085	7,88E-02	-4,16E-04	11,45	0,005	0,057
0,090	7,88E-02	-4,46E-04	11,45	0,005	0,057
0,095	7,88E-02	-4,78E-04	11,45	0,005	0,057
0,100	7,88E-02	-5,10E-04	11,45	0,005	0,057
0,105	7,88E-02	-5,44E-04	11,45	0,005	0,057
0,110	7,88E-02	-5,79E-04	11,45	0,005	0,057
0,115	7,88E-02	-6,16E-04	11,45	0,005	0,057
0,120	7,88E-02	-6,54E-04	11,45	0,005	0,057
0,125	7,88E-02	-6,93E-04	11,45	0,005	0,057
0,130	7,88E-02	-7,34E-04	11,45	0,005	0,057
0,135	7,88E-02	-7,77E-04	11,45	0,005	0,057
0,140	7,88E-02	-8,22E-04	11,45	0,005	0,057
0,145	7,88E-02	-8,69E-04	11,45	0,005	0,057
0,150	7,87E-02	-9,18E-04	11,45	0,005	0,057
0,155	7,87E-02	-9,69E-04	11,45	0,005	0,057
0,160	7,87E-02	-1,02E-03	11,45	0,005	0,057
0,165	7,87E-02	-1,08E-03	11,45	0,005	0,057
0,170	7,87E-02	-1,14E-03	11,45	0,005	0,057
0,175	7,87E-02	-1,20E-03	11,45	0,005	0,057
0,180	7,87E-02	-1,26E-03	11,45	0,005	0,057
0,185	7,87E-02	-1,33E-03	11,45	0,005	0,057
0,190	7,87E-02	-1,40E-03	11,45	0,005	0,057
0,195	7,87E-02	-1,47E-03	11,45	0,005	0,057
0,200	7,87E-02	-1,55E-03	11,45	0,005	0,057
0,205	7,87E-02	-1,63E-03	11,45	0,005	0,057
0,210	7,87E-02	-1,72E-03	11,45	0,005	0,057
0,215	7,87E-02	-1,81E-03	11,45	0,005	0,057
0,220	7,87E-02	-1,90E-03	11,45	0,005	0,057
0,225	7,86E-02	-2,00E-03	11,45	0,005	0,057
0,230	7,86E-02	-2,10E-03	11,45	0,005	0,057
0,235	7,86E-02	-2,21E-03	11,45	0,005	0,057
0,240	7,86E-02	-2,32E-03	11,45	0,005	0,057
0,245	7,86E-02	-2,44E-03	11,45	0,005	0,057
0,250	7,86E-02	-2,56E-03	11,45	0,005	0,057
0,255	7,86E-02	-2,69E-03	11,45	0,005	0,057
0,260	7,86E-02	-2,83E-03	11,45	0,005	0,057
0,265	7,85E-02	-2,98E-03	11,45	0,005	0,057
0,270	7,85E-02	-3,13E-03	11,45	0,005	0,057
0,275	7,85E-02	-3,29E-03	11,45	0,005	0,057
0,280	7,85E-02	-3,45E-03	11,45	0,005	0,057
0,285	7,85E-02	-3,63E-03	11,45	0,005	0,057
0,290	7,85E-02	-3,81E-03	11,45	0,005	0,057
0,295	7,84E-02	-4,00E-03	11,45	0,005	0,057
0,300	7,84E-02	-4,21E-03	11,45	0,005	0,057
0,305	7,84E-02	-4,42E-03	11,45	0,005	0,057
0,310	7,84E-02	-4,64E-03	11,45	0,005	0,057
0,315	7,84E-02	-4,87E-03	11,45	0,005	0,057
0,320	7,83E-02	-5,12E-03	11,45	0,005	0,057
0,325	7,83E-02	-5,38E-03	11,45	0,005	0,057
0,330	7,83E-02	-5,65E-03	11,45	0,005	0,057

0,335	7,82E-02	-5,93E-03	11,45	0,005	0,057
0,340	7,82E-02	-6,23E-03	11,45	0,005	0,057
0,345	7,82E-02	-6,55E-03	11,45	0,005	0,057
0,350	7,82E-02	-6,88E-03	11,45	0,005	0,057
0,355	7,81E-02	-7,22E-03	11,45	0,005	0,057
0,360	7,81E-02	-7,59E-03	11,45	0,005	0,057
0,365	7,80E-02	-7,97E-03	11,45	0,005	0,057
0,370	7,80E-02	-8,37E-03	11,45	0,005	0,057
0,375	7,80E-02	-8,79E-03	11,45	0,005	0,057
0,380	7,79E-02	-9,23E-03	11,45	0,005	0,057
0,385	7,79E-02	-9,70E-03	11,45	0,005	0,057
0,390	7,78E-02	-1,02E-02	11,45	0,005	0,057
0,395	7,78E-02	-1,07E-02	11,45	0,005	0,057
0,400	7,77E-02	-1,12E-02	11,45	0,005	0,057
0,405	7,76E-02	-1,18E-02	11,45	0,005	0,057
0,410	7,76E-02	-1,24E-02	11,45	0,005	0,057
0,415	7,75E-02	-1,30E-02	11,45	0,005	0,057
0,420	7,75E-02	-1,37E-02	11,45	0,005	0,057
0,425	7,74E-02	-1,44E-02	11,45	0,005	0,057
0,430	7,73E-02	-1,51E-02	11,45	0,005	0,057
0,435	7,72E-02	-1,58E-02	11,45	0,005	0,057
0,440	7,72E-02	-1,66E-02	11,45	0,005	0,057
0,445	7,71E-02	-1,75E-02	11,45	0,005	0,057
0,450	7,70E-02	-1,83E-02	11,45	0,005	0,057
0,455	7,69E-02	-1,93E-02	11,45	0,005	0,057
0,460	7,68E-02	-2,02E-02	11,45	0,005	0,057
0,465	7,67E-02	-2,13E-02	11,45	0,005	0,057
0,470	7,66E-02	-2,23E-02	11,45	0,005	0,057
0,475	7,65E-02	-2,34E-02	11,45	0,005	0,057
0,480	7,63E-02	-2,46E-02	11,45	0,005	0,057
0,485	7,62E-02	-2,59E-02	11,45	0,005	0,057
0,490	7,61E-02	-2,72E-02	11,45	0,005	0,057
0,495	7,59E-02	-2,85E-02	11,45	0,005	0,057
0,500	7,58E-02	-3,00E-02	11,45	0,005	0,057
0,505	7,56E-02	-3,15E-02	11,45	0,005	0,057
0,510	7,55E-02	-3,30E-02	11,46	0,005	0,057
0,515	7,53E-02	-3,47E-02	11,46	0,005	0,057
0,520	7,51E-02	-3,64E-02	11,46	0,005	0,057
0,525	7,49E-02	-3,83E-02	11,46	0,005	0,057
0,530	7,48E-02	-4,02E-02	11,46	0,005	0,057
0,535	7,45E-02	-4,22E-02	11,46	0,005	0,057
0,540	7,43E-02	-4,43E-02	11,46	0,005	0,057
0,545	7,41E-02	-4,66E-02	11,46	0,005	0,057
0,550	7,39E-02	-4,89E-02	11,46	0,005	0,057
0,555	7,36E-02	-5,14E-02	11,46	0,005	0,057
0,560	7,34E-02	-5,39E-02	11,47	0,005	0,057
0,565	7,31E-02	-5,66E-02	11,47	0,005	0,057
0,570	7,28E-02	-5,95E-02	11,47	0,005	0,057
0,575	7,25E-02	-6,25E-02	11,47	0,005	0,057
0,580	7,22E-02	-6,56E-02	11,47	0,005	0,057

0,585	7,18E-02	-6,89E-02	11,48	0,005	0,057
0,590	7,15E-02	-7,24E-02	11,48	0,005	0,057
0,595	7,11E-02	-7,60E-02	11,48	0,005	0,057
0,600	7,07E-02	-7,98E-02	11,49	0,005	0,057
0,605	7,03E-02	-8,38E-02	11,49	0,005	0,057
0,610	6,99E-02	-8,80E-02	11,49	0,005	0,057
0,615	6,94E-02	-9,25E-02	11,50	0,005	0,057
0,620	6,89E-02	-9,71E-02	11,50	0,005	0,058
0,625	6,84E-02	-1,02E-01	11,51	0,005	0,058
0,630	6,79E-02	-1,07E-01	11,51	0,005	0,058
0,635	6,74E-02	-1,12E-01	11,52	0,005	0,058
0,640	6,68E-02	-1,18E-01	11,53	0,005	0,058
0,645	6,62E-02	-1,24E-01	11,54	0,005	0,058
0,650	6,56E-02	-1,30E-01	11,55	0,005	0,058
0,655	6,49E-02	-1,37E-01	11,56	0,005	0,058
0,660	6,42E-02	-1,44E-01	11,57	0,005	0,058
0,665	6,35E-02	-1,51E-01	11,58	0,005	0,058
0,670	6,27E-02	-1,59E-01	11,59	0,005	0,058
0,675	6,19E-02	-1,67E-01	11,61	0,005	0,058
0,680	6,10E-02	-1,75E-01	11,62	0,005	0,058
0,685	6,01E-02	-1,84E-01	11,64	0,005	0,058
0,690	5,92E-02	-1,93E-01	11,66	0,005	0,058
0,695	5,82E-02	-2,03E-01	11,68	0,005	0,058
0,700	5,72E-02	-2,13E-01	11,70	0,005	0,059
0,705	5,61E-02	-2,23E-01	11,73	0,005	0,059
0,710	5,49E-02	-2,35E-01	11,76	0,005	0,059
0,715	5,37E-02	-2,46E-01	11,79	0,005	0,059
0,720	5,25E-02	-2,59E-01	11,83	0,005	0,059
0,725	5,11E-02	-2,72E-01	11,86	0,005	0,059
0,730	4,97E-02	-2,85E-01	11,91	0,005	0,060
0,735	4,83E-02	-3,00E-01	11,95	0,005	0,060
0,740	4,67E-02	-3,15E-01	12,00	0,005	0,060
0,745	4,51E-02	-3,31E-01	12,06	0,005	0,060
0,750	4,34E-02	-3,47E-01	12,12	0,005	0,061
0,755	4,16E-02	-3,65E-01	12,19	0,005	0,061
0,760	3,98E-02	-3,83E-01	12,26	0,005	0,061
0,765	3,78E-02	-4,02E-01	12,34	0,005	0,062
0,770	3,58E-02	-4,23E-01	12,43	0,005	0,062
0,775	3,36E-02	-4,44E-01	12,53	0,005	0,063
0,780	3,13E-02	-4,66E-01	12,63	0,006	0,063
0,785	2,89E-02	-4,89E-01	12,75	0,006	0,064
0,790	2,64E-02	-5,14E-01	12,87	0,006	0,064
0,795	2,38E-02	-5,40E-01	13,01	0,006	0,065
0,800	2,10E-02	-5,67E-01	13,16	0,006	0,066
0,805	1,81E-02	-5,95E-01	13,32	0,006	0,067
0,810	1,51E-02	-6,25E-01	13,50	0,006	0,068
0,815	1,19E-02	-6,57E-01	13,70	0,006	0,068
0,820	8,49E-03	-6,90E-01	13,91	0,006	0,070
0,825	4,95E-03	-7,24E-01	14,14	0,006	0,071
0,830	1,24E-03	-7,61E-01	14,39	0,006	0,072

TRITA-ABE-MBT-2120